

Combined Hydrodynamic and Reaction Analysis of a Bubbling to Turbulent Fluidized Bed Reactor

Jean Saayman

University of Pretoria

Combined Hydrodynamic and Reaction Analysis of a Bubbling to Turbulent Fluidized Bed Reactor

by

Jean Saayman

A thesis submitted in partial fulfilment of
the requirements for the degree

Philosophiae Doctor (Chemical Engineering)

in the

Department of Chemical Engineering

Faculty of Engineering, the Built Environment and Information
Technology

University of Pretoria

06 June 2013

Combined Hydrodynamic and Reaction Analysis of a Bubbling to Turbulent Fluidized Bed Reactor

Author : Jean Saayman
Supervisor : Prof. Willie Nicol
Department : Department of Chemical Engineering
University of Pretoria
Degree : Philosophiae Doctor (Chemical Engineering)

Extended Abstract

There are many large-scale contacting methods for gas reactions requiring a solid catalyst. The catalytic gas-solid Fluidized Bed Reactor (FBR) is one of the popular methods in industry. In FBRs the bulk of the gas throughput is present as lean bubbles, mostly deprived of solids, bubbling through a solids-rich emulsion phase. The movement of gas into and out of the emulsion often dictates the performance of an FBR. During the past five decades major contributions have been made towards the understanding of FBRs, although numerous gaps still exist, especially at higher bubbling regime velocities.

This work follows an integrated approach for the simultaneous measurement of hydrodynamics and reactor performance. Hydrodynamics are measured using fast X-Ray Tomography (XRT), pressure analysis techniques and an optical fibre probe. Reactor performance is measured by utilizing the ozone decomposition reaction. Performance is quantified using a basic two-phase reactor model with an apparent overall interphase mass transfer (K_0) parameter. Two 14 cm (ID) fluidized bed columns are used, one setup supporting the ozone decomposition reaction and the other installed within a fast XRT facility. Special emphasis is placed on superficial velocities (U_0) spanning the entire bubbling regime up to the onset of the turbulent regime (U_c). The particle types employed are Geldart B sand particles and highly dense ferro-silicon (FeSi) particles. Fines are added to both particle types, resulting in a total of four particle systems (sand baseline; sand with fines; FeSi baseline; FeSi with fines). Time constraints on the XRT equipment limited the tomography measurements to the sand baseline particle system. The hydrodynamics of the

other particle systems were limited to the pressure signal and optical probe measurements of the ozone decomposition setup.

The results of the sand baseline system suggest that a distinction should be made between the low-interaction bubbling regime and the high-interaction bubbling regime. A change in mass transfer behaviour occurs around a U_0/U_c value of 0.25. Reactor performance increases up to $U_0/U_c = 0.7$, after which a decreasing trend is observed. An empirical correlation is proposed for the specific interphase mass transfer (k_{be}) of the higher velocity bubbling regime. This correlation is based on the integration of the hydrodynamics determined by means of XRT and reactor performance:

$$k_{be} \propto \frac{\psi_B}{\phi_0 U_0} = \beta \quad 4-12$$

The hydrodynamic parameter β gives the best fit for the entire velocity range with an average error of 8%, although it is not recommended for $U_0/U_c < 0.17$. It is observed that the classical approach of penetration theory for interphase mass transfer, performs exceptionally well at low velocities ($U_0/U_c < 0.34$).

The addition of fines to the FeSi particle type decreases the overall reactor performance, despite decreased bubble sizes. The solids fraction, however, unexpectedly increases with the addition of fines and a collapse of the emulsion phase is measured. It is therefore postulated that though flow in the emulsion phase is much higher for the FeSi baseline system and decreases with the addition of fines. For the sand particle type, the behaviour expected from literature is observed: reactor performance increases, bubble sizes decrease and the solids fraction decreases.

Very distinct hydrodynamic behaviour is observed for all the fluidization regimes with XRT. Probability density distributions show there are still two phases present in the turbulent regime and that the emulsion-phase solids fraction remains independent of velocity until fast fluidization sets in. The turbulent regime has unique hydrodynamic behaviour, although voids appear to be a transient structure between the structures of the bubbling and fast fluidization regimes.

KEYWORDS: Fast X-ray tomography; Reactor performance; Void behaviour; Cross-sectional solids fraction; High-density particles; Ozone decomposition reaction

Acknowledgements

“A PhD will be the only time you get to pour all your focus and energy into one subject for a few years – enjoy every second of it!” – Prof. W. Nicol. With all its ups and downs I truly enjoyed doing this work. Many people have contributed to making it such a successful time and project. Thank you all.

I would like to express my immense gratitude to my Supervisor, Professor Willie Nicol, for all his advice and guidance, as well as affording me the opportunity for international research exposure. I want to acknowledge and thank Professor Naoko Ellis for her input regarding the reaction studies, as well as the University of British Columbia for the use of their optical voidage probe. Also, I would like to thank Professor Ruud van Ommen from the Delft University of Technology for the use of the University’s fast X-ray tomography setup. I received much advice and guidance during my visit to the institution. Professor Rob Mudde and Evert Wagner need to be mentioned as well.

Lastly, thank you to my family, friends and fellow office coffee drinkers for all the non-work-related support, specifically to both my parents. I am also grateful to Sasol Research and Development for their financial support.

Contents

Extended Abstract	ii
Acknowledgements	iv
List of Figures	viii
List of Tables.....	xi
Nomenclature	xii
Chapter 1 : Introduction	1
1.1 Outline of the thesis	3
Chapter 2 : Literature Review	5
2.1 Fluidized bed fundamentals	5
2.2 Measuring methods.....	9
2.2.1 Pressure signals	9
2.2.2 Optical probes	10
2.2.3 Tomography	12
2.2.4 Ozone decomposition reaction	12
2.3 Solids and voids behaviour.....	13
2.3.1 Fines	16
2.4 Fluidized bed reactor models.....	16
2.4.1 Basic two-phase model.....	17
2.4.2 Three-phase model	17
2.4.3 Bubbling-turbulent model	18
2.5 Mass transfer.....	19
2.5.1 Mass transfer correlations	20
2.5.2 Performance of correlations	24
Chapter 3 : Tomography	25
3.1 Experimental.....	26

3.2	Results and discussion	30
3.2.1	Regime quantification	30
3.2.2	Cross-sectional solids concentration	31
3.2.3	Tomographic reconstruction	35
3.3	Conclusions	44
Chapter 4	: Linking Reactor Performance and Hydrodynamics	46
4.1	Experimental.....	46
4.1.1	Setup.....	46
4.1.2	Ozone decomposition catalyst.....	49
4.1.3	Method	49
4.2	Results and discussion	52
4.2.1	Reactor performance quantification	52
4.2.2	Overall reactor performance (K_0).....	54
4.2.3	Hydrodynamic measurements	55
4.2.4	Linking reactor performance and XRT measurements	57
4.3	Mass transfer correlations.....	59
4.3.1	Penetration theory	59
4.3.2	Boundary layer theory	60
4.3.3	Empirical correlation.....	61
4.4	Conclusions	64
Chapter 5	: Reactor Performance	65
5.1	Experimental.....	65
5.2	Estimation of bubble size	67
5.3	Results and discussion	68
5.3.1	Regime quantification	68
5.3.2	Reactor performance	70
5.3.3	Hydrodynamics	72

5.3.4	Specific mass transfer.....	76
5.3.5	Emulsion phase flow	79
5.4	Conclusions	80
Chapter 6	: Concluding Remarks	82
References	84
Appendix A	: XRT Calibration	91
Appendix B	: Determination of Hydrodynamic Parameters	101
Appendix C	: Reactor Performance Data.....	106

List of Figures

Figure 2.1: Geldart particle classification (taken from [45]).....	5
Figure 2.2: Standard deviation of pressure fluctuations used to define U_c and U_k [5].....	7
Figure 2.3: Definition of U_{tr} [5].....	8
Figure 2.4: Definition of U_{se} [5].....	8
Figure 2.5: Graphical explanation of the non-intrusive void measurement technique using pressure signals. Signals are measured in the plenum chamber, in the bubbling fluidized bed and processed to obtain a measure of bubble size.....	10
Figure 2.6: Illustration of the optical voidage probe.....	11
Figure 2.7: Explanation of how two probes are used to determine void bubble length.....	11
Figure 2.8: Average cross-sectional solids concentrations as the velocity increases for the top (+) and bottom (*) measurement planes [74].....	15
Figure 2.9: Bubble size (top) and bubble velocity (bottom) results of Brouwer et al. [76]. The XRT technique shows very good agreement with bubble size. Circles (o) represent bubble means and asterisks (*) one standard deviation. The dashed lines are the predicted values.....	15
Figure 2.10: Schematic representation of possible resistance to mass transfer.....	21
Figure 3.1: Top view of the fast XRT setup showing the three detector arrays and sources. Side view showing a single upper and lower detector array (taken from Brouwer et al. [76]).....	27
Figure 3.2: Photographs from the top and side of the setup.....	27
Figure 3.3: Position of 16 measuring lines (half of a single detector array). Horizontal lines indicate the positions of the partitions used for calibration.....	28
Figure 3.4: (a) is an example of the calculated cross-sectional solids concentration signal obtained for both the top and bottom measuring planes; the example is taken from the measurement done at 200 mm above the distributor and at a velocity of 0.11 m/s. (b) and (c) show the same signal, except that the top plane's signal is shifted in time. (d) is the calculated SSD between the top and bottom plane signals at different top plane time shifts.....	29
Figure 3.5: Standard deviation of pressure fluctuations, showing the bubbling to turbulent regime transition (U_c) at 0.65 m/s. Also shown is the standard deviation of incoherence, which is a measure of the void size. The end of turbulent fluidization (U_k) is determined to be 1.19 m/s.....	30
Figure 3.6: Average cross-sectional solids concentration with superficial velocity at $H=200$ mm, $H=300$ mm, $H=400$ mm and $H=500$ mm from the distributor.....	32
Figure 3.7: Mean line solids fraction indicating radial distribution of solids. Bold markers indicate U_c and U_k . Regime indication is given in the velocity legend.....	33
Figure 3.8: Density distributions of the cross-sectional solids concentration (ϕ) at different heights.....	34
Figure 3.9: Average voids movement.....	35

Figure 3.10: Reconstructed cross-sectional image for the bottom and top planes. Both images are taken at the same point in time. This example is taken from the measurement at a height of 300 mm and a superficial velocity of 0.11 m/s.....36

Figure 3.11: Pseudo-3D reconstruction of the void shapes over 2 s. $H = 300$ mm and $U_0 = 0.11$ m/s. The y-axis and x-axis give length dimensions, while the z-axis represents time. $t=0$ s at top and $t=2$ s at bottom36

Figure 3.12: Samples of 2 s reconstructions at two superficial velocities (bubbling – $u_0 = 0.43$ m/s and turbulent – $u_0 = 0.87$ m/s) and heights ($H = 200$ mm and $H = 400$ mm)37

Figure 3.13: Fraction of void objects that could be matched in both bottom and top planes39

Figure 3.14: Comparison of bubble size correlations with the measured bubble diameters (d_b) for the regime from bubbling up to turbulent41

Figure 3.15: Quantification of void structures.....42

Figure 3.16: Illustration of the core annulus at different heights in the column. $U_0 = 1.84$ m/s.....43

Figure 3.17: Comparison of different methods for determining the average rise velocity of voids44

Figure 4.1: Reactor experimental setup and schematic drawing48

Figure 4.2: Confirmation of first-order behaviour. The linear line is a first-order PFR model with $k_r = 15$ s⁻¹49

Figure 4.3: First-order rate constant as experiments were conducted52

Figure 4.4: Reactor performance and fitted polynomial for interpolation55

Figure 4.5: Agreement between measured standard deviation of incoherence and the bubble size, determined via XRT56

Figure 4.6: Comparison of measured solids concentration at $H = 200$ mm between the optical probe and XRT57

Figure 4.7: Combination of hydrodynamic parameters having the same trend as the reactor performance parameter K_059

Figure 4.8: Predicted specific mass transfer compared with the measured specific mass transfer based on several theories and correlations. The error made in the modified correlation prediction is shown63

Figure 5.1: First-order behaviour confirmed for FeSi catalyst.....66

Figure 5.2: Regime transition confirmed to be at 0.65 m/s for sand69

Figure 5.3: From visual inspection the standard deviations of differential pressure fluctuations show a U_c of 0.36 m/s for the baseline case and 0.33 m/s for the case of added fines. The different method of random velocity selection resulted in a smooth band of data being created.....70

Figure 5.4: Reactor performance results for sand. Behaviour in the bubbling regime is as expected.....71

Figure 5.5: Reactor performance for FeSi showing an increasing trend. Statistical analysis was applied to every five consecutive data points for the “Baseline” case and to every four consecutive data points for the “With Fines” case. Bar plots indicate the relevant mean and standard deviations in the x- and y-directions of this analysis.....72

Figure 5.6: Incoherent standard deviation at 20 cm. Sand results are at the top and FeSi results at the bottom.....73

Figure 5.7: Bubble sizes from the voidage probe, showing equivalent void diameter at 0.20 m above the distributor. Sand results are in the top graph and FeSi results in the bottom graph. Good agreement between the incoherence and the probe measurement is obtained for FeSi; sand does not have acceptable agreement with the incoherence or XRT results74

Figure 5.8: Average solids concentration showing that FeSi has an opposite trend from sand, with the addition of fines. These readings are from the voidage probe at $r/R=0$ and $h=0.20$ m. Sand results are at the top and FeSi results at the bottom75

Figure 5.9: Calculating void lengths for the case of sand with added fines using incoherence data77

Figure 5.10: Specific mass transfer with superficial velocity. A statistical analysis was applied to every five consecutive data points for the FeSi “Baseline” case and every four consecutive data points for the FeSi “With Fines” case. Bar plots indicate the relevant mean and standard deviations in the x- and y-directions of this analysis.....78

Figure 5.11: Solids concentration distribution at $r/R = 0$ and 0.2 m from the distributor. The distributions at low and high superficial velocities for the baseline case and the case with added fines are shown80

Figure A.1: Calibration curves at 25 mA, source 191

Figure A.2: Calibration curves at 25 mA, source 292

Figure A.3: Calibration curves at 25 mA, source 392

Figure A.4: Calibration curves at 50 mA, source 193

Figure A.5: Calibration curves at 50 mA, source 293

Figure A.6: Calibration curves at 50 mA, source 394

Figure B.1: U_{mf} for Sand baseline determined to be 9.1 mm/s..... 101

Figure B.2: U_{mf} for Sand with fines determined to be 4.0 mm/s..... 102

Figure B.3: U_{mf} for FeSi baseline determined to be 6.5 mm/s 102

Figure B.4: U_{mf} for FeSi with fines determined to be 5.0 mm/s 103

Figure B.5: Entrainment measurements for Sand baseline..... 104

Figure B.6: Entrainment measurements for FeSi baseline and with fines..... 105

List of Tables

<i>Table 2-1: U_c correlations (as quoted by Arnaldos and Casal[46])</i>	7
<i>Table 3-1: U_c correlations and predictions of the system under investigation [46]</i>	31
<i>Table 3-2: Signal lengths analysed to determine mean bubble diameter</i>	39
<i>Table 4-1: Catalyst and fluidizing medium properties</i>	51
<i>Table 5-1: Catalyst and fluidizing medium properties</i>	67
<i>Table 5-2: U_c correlations and predictions of the FeSi baseline system (as quoted by Arnaldos and Casal [46])</i>	69
<i>Table A-1: Calibration coefficients for source 1 and 25 mA</i>	95
<i>Table A-2: Calibration coefficients for source 2 and 25 mA</i>	96
<i>Table A-3: Calibration coefficients for source 3 and 25 mA</i>	97
<i>Table A-4: Calibration coefficients for source 1 and 50 mA</i>	98
<i>Table A-5: Calibration coefficients for source 2 and 50 mA</i>	99
<i>Table A-6: Calibration coefficients for source 3 and 50 mA</i>	100
<i>Table C-1: Data of baseline sand experiments</i>	106
<i>Table C-2: Data of sand with added fines experiments</i>	107
<i>Table C-3: Data of baseline FeSi experiments</i>	108
<i>Table C-4: Data of FeSi with added fines experiments</i>	109

Nomenclature

A_{cal}	Calibration coefficient 1	[-]
a_I	Inter-phase transfer surface	[m ⁻¹]
Ar	Archimedes number ($= d_p^3 \cdot \rho_g \cdot (\rho_s - \rho_g) \cdot g / \mu^2$)	[-]
B_{cal}	Calibration coefficient 2	[-]
C_B	Concentration in bubble	[mol/m ³]
C_C	Concentration in cloud	[mol/m ³]
C_{cal}	Calibration coefficient 3	[-]
C_e	Concentration in emulsion	[mol/m ³]
C_i	Gas concentration of species I	[kmol/m ³]
$C_{i,IN}$	Inlet concentration	[kmol/m ³]
D	Reactor diameter	[m]
D_e	Effective diffusivity of gas in the emulsion phase	[m ² /s]
D_{gl}	Diffusion coefficient of gas into liquid	[m ² /s]
D_m	Gas diffusion coefficient	[m ² /s]
D_b	Bubble diameter	[m]
d_p	Particle diameter	[m]
d_p^*	Modified particle diameter ($= Ar^{1/3}$)	[m]
D_z	Axial dispersion coefficient	[m ² /s]
f_{kq}	Coefficient in the Sit and Grace k_q correlation	[-]
F_P	Degree of pressure fluctuations	[-]
f_{Pe}	Coefficient in the Bi and Grace Pe correlation	[-]
g	Gravitational acceleration (9.81)	[m/s ²]
G_s	Solids circulation rate/ Entrainment rate	[kg/s.m ²]
H	XRT measuring height above distributor	[mm]
H_b	Bed height	[m]
i	X-ray beam number	[-]
I_{Xray}	X-ray beam intensity	[au]
K_{bc}	Bubble-cloud mass transfer (bubble area based)	[s ⁻¹]
K_{be}	Bubble-emulsion mass transfer (bubble area based)	[s ⁻¹]
K_{ce}	Cloud-emulsion mass transfer (bubble area based)	[s ⁻¹]

K_O	Overall bubble-emulsion mass transfer (catalyst volume based)	$[s^{-1}]$
L_b	Length/height of voids	$[m]$
l_i	Length of a single X-ray beam inside the column	$[m]$
l_T	Total length of X-ray beams in the column from a single source	$[m]$
k_{be}	Specific bubble-emulsion mass transfer	$[m/s]$
k_{db}	Correction coefficient for bubble size correlation	$[-]$
k_{gl}	Gas-liquid mass transfer	$[m/s]$
k_R	Reaction rate constant (catalyst volume based)	$[s^{-1}]$
P	Pressure at a single point	$[Pa]$
ΔP	Pressure drop	$[Pa]$
Pe	Peclet number ($U \cdot H_b / D_z$)	$[-]$
q	Volumetric flow rate ratio (q_i / Q_{TOTAL})	$[-]$
Q	Volumetric flow rate	$[m^3/s]$
q_{bc}	Exchange rate between bubble and cloud phase	$[m^3/s]$
Re	Reynolds number ($d_p \cdot u_o \cdot \rho_g / \mu$)	$[-]$
R_i	Reaction rate as a function of concentration	$[s^{-1}]$
R_p	Radius of penetration	$[m]$
S_b	Surface area of bubble	$[m^2]$
Sc	Schmidt number ($\mu / (\rho_g \cdot D_m)$)	$[-]$
SSD	Sum of squared differences used for \bar{u}_v determination	$[-]$
t_e	Element of solids exposure time to bubble for gas exchange	$[s]$
U_b	Average bubble velocity, relative to distributor	$[m/s]$
u_B	Bubble phase reactor model gas velocity	$[m/s]$
U_{b-Tomo}	Tomography determined bubble velocity, relative to distributor	$[m/s]$
U_{b-Theo}	Calculated theoretical bubble velocity, relative to distributor	$[m/s]$
U_{br}	Terminal rise velocity of a single bubble	$[m/s]$
U_c	Onset of turbulent regime velocity	$[m/s]$
u_C	Cloud phase reactor model gas velocity	$[m/s]$
u_E	Emulsion phase reactor model gas velocity	$[m/s]$
U_k	End of turbulent regime velocity	$[m/s]$
U_{mb}	Minimum bubble velocity	$[m/s]$
U_{mf}	Minimum fluidization velocity	$[m/s]$
U_{mf}^*	Modified minimum fluidization velocity ($Re/Ar^{1/3}$)	$[m/s]$
U_0	Operating velocity	$[m/s]$

U_{se}	Significant entrainment velocity	[m/s]
U_t	Terminal particle velocity	[m/s]
U_{tr}	Transport velocity	[m/s]
\bar{u}_v	Average void rise velocity	[m/s]
V_b	Volume of bubble/void	[m ³]
z	Height in reactor (from distributor)	[m]

Subscripts

B	Bubble phase (low-density phase)
b	Bubble
C	Cloud phase
E	Emulsion phase (high-density phase)
H	High-density phase
L	Low-density phase
mf	Minimum fluidization
\bar{P}	Average value

Greek letters

β	Empirical mass transfer parameter ($\psi_B / (\Phi_0 U_0)$)	[s/m]
ε	Gas volume fraction	[-]
ε_{mf}	Gas volume fraction at minimum fluidization	[-]
ε_0	Porosity of fluidized bed at specific	[-]
ρ_b	Bulk density	[kg/m ³]
ρ_s ($/\rho_p$)	Particle density	[kg/m ³]
ρ_g	Gas density	[kg/m ³]
μ_G	Gas viscosity	[Pa.s]
Φ	Solids volume fraction (1- ε)	[-]
$\Phi_{L,0}$	Solids volume fraction in the L-phase in a bubble bed	[-]
ϕ	Instantaneous cross-sectional solids fraction	[-]
$\bar{\phi}$	Mean cross-sectional solids fraction	[-]
ϕ_i	Instantaneous line solids fraction	[-]
$\bar{\phi}_i$	Mean line solids fraction	[-]
ϕ_{packed}	Solids fraction of packed bed	[-]

ψ	Phase volume fraction	[-]
ψ_B	Bubble phase volume fraction	[-]
ψ_f	Fluid flow streamline function	[-]

Chapter 1 : Introduction

Catalytic Gas-Solid Fluidized Bed Reactors (FBRs) have been studied and used for over six decades. From novel laboratory demonstrations [1] to performing nanoparticle coatings [2], to being at the heart of large petrochemical companies [3,4], these reactors have many uses. From an engineering point of view, advantages include: efficient solids mixing, good gas-solid contacting and low pressure drop. A wealth of understanding of the hydrodynamics of FBRs and their effects on reactor performance has been gained, although there are numerous areas where fundamental understanding is lacking. Many studies focus on either a specific hydrodynamic parameter or purely on the reactor performance. By using the one, deductions are made with regard to the other. For instance; hydrodynamic insight is used to infer the effect on the reactor performance or the reactor performance is used to infer the hydrodynamic cause. Few studies have followed an integrated approach, which creates difficulties in modelling an FBR. Depending on the operating velocity (U_0) several regimes exist in FBRs, most commonly used being the bubbling, turbulent or fast fluidization regimes. Each regime is characterized by its own hydrodynamic behaviours. The bubbling and fast fluidization regimes have enjoyed much academic attention due to the distinctness of the bubbles and the core annulus, respectively. The turbulent regime has better gas-solids contacting than the bubbling regime without the high solids circulation of the fast fluidization regime. These reasons make the turbulent regime a popular choice for industry. Commercial examples of turbulent reactors include FCC regenerators, zinc sulphide roasters and Mobil MTG, acrylonitrile, maleic anhydride, phthalic anhydride and ethylene dichloride reactors. Despite the turbulent regime being popular in industry, it has not received as much attention as the bubbling or fast fluidization regimes [5].

Based on observations of incipiently fluidized bubbling beds, the need for hydrodynamic descriptions of two-phase behaviour arose. The earliest well-known published works on the matter were those of Rowe and Partridge [6,7] and Davidson and Harrison [8–10]. The concept was developed further and gas exchange between the phases was explored [11–16]. Ultimately, leaders in the field such as Kunii, Levenspiel and Grace proposed reactor models based on the theory [17–22]. Generally, these reactor models and the two-phase theory best describe the hydrodynamic behaviour of bubbling fluidized beds [23–26]. The theory entails that most of the gas reagents are contained in a lean, solids/catalyst-deprived phase that

bubbles though a dense, solids-rich (emulsion) phase. This closely resembles the physical phenomena in the FBR. Since most of the gas throughput is present in the lean phase, the movement of gas into and out of the emulsion phase often dictates the performance of an FBR. Therefore the description of the interphase mass transfer becomes one of the crucial modelling variables. Most correlations for this transfer are derived on the basis of low-velocity/interaction bubbling regime behaviour (small U_0/U_c values of 0.02). U_c is the onset velocity of the turbulent regime. In this low U_0/U_c regime the bubbles have near-ideal geometries and low interactions with each other. Despite the success of these models at lower velocities, the transfer correlations are not suited for higher velocity operations [25,27–29]. Few attempts have been made to adapt interphase mass transfer correlations for the higher velocity bubbling regime or turbulent regime [30].

A integrated approach combining hydrodynamics and reactor performance is followed in this study with the focus on the upper end of the bubbling regime and the start of the turbulent regime. The aim was to investigate which theories in the literature are applicable and which do not hold in a more “violently” bubbling bed. This was achieved by performing in-depth hydrodynamic investigations into reactive fluidized beds. The ozone decomposition reaction was used and all experiments were executed at atmospheric conditions. Two particle types, sand and ferrosilicon (FeSi), were used. FeSi is a particle with a density of $6\,800\text{ kg/m}^3$. Little is available in the open literature about the fluidizing properties of extremely dense particles. FBRs utilizing high-density particles already exist in industry; an example, relevant to South Africa, is the High-Temperature Fisher-Tropsch (HTFT) reactor. These reactors operate with dense iron- or cobalt-based catalysts [3,4]. The literature also indicates that fines introduce desirable hydrodynamics into fluidized beds [28,31–41]. Fines were therefore used as a means to validate the reactor performance quantification technique and were added to each particle type, creating four particle systems:

- A sand baseline system
- A sand with fines system
- A FeSi baseline system.
- A FeSi with fines system.

Two setups were used, namely a reaction setup and a tomography setup. The reaction setup was equipped with pressure sensors and an optical probe. The initial idea was to perform reaction and hydrodynamic measurements simultaneously in our local laboratories. However, this plan was modified and subsequently advanced X-Ray Tomography (XRT)

measurements were done at the Delft University of Technology in the Netherlands. The Delft facility did not allow the simultaneous implementation of a catalytic gas phase reaction, so in order to unify the two investigations the same column diameter was employed. Due to time constraints only one particle system was used in the tomography setup – the sand baseline system. Special emphasis was placed on consolidating the reaction work with the advanced hydrodynamic measurements (see [Chapter 4](#)).

The XRT setup is a 1.5 m high, 14 cm diameter column with a two-cyclone return system. The bubbling, turbulent and fast fluidization flow regimes were investigated. All reaction experiments were conducted in a 14 cm column; 5.5 m in height, with a two-cyclone return system. The reaction used was the ozone decomposition reaction and only the bubbling and turbulent onset regimes were investigated ($0.09 < U_0/U_c < 1.11$). This velocity constraint was due to flow and pressure limitations caused by the ozone outlet system. Reactor performance was quantified using a basic two-phase model to obtain the apparent overall mass transfer. The reactor performance and hydrodynamics of high-density FeSi particles were investigated and experimentally compared with the well-studied particle system of sand. For FeSi the velocity range was, similarly, the bubbling regime to the onset of the turbulent regime ($0.16 < U_0/U_c < 1.08$).

1.1 Outline of the thesis

- [Chapter 2](#) is a review of all the general literature on the subject and that relevant to this thesis.
- [Chapter 3](#) covers the advanced hydrodynamic measurements of the XRT setup: the experimental work conducted in a 14 cm (ID) column using Geldart B sand particles covering the bubbling, turbulent and fast fluidization regimes. The cross-sectional solids concentration, solids distributions and three-dimensional void reconstructions are observed and quantified.
- [Chapter 4](#) continues with the same particle system in which reaction work was conducted in a similar 14 cm (ID) column. The ozone decomposition reaction is used to quantify reactor performance. Only the bubbling regime up to the onset of the turbulent regime is investigated. The link between hydrodynamics and reactor performance is made via an interphase mass transfer model, in which the bubble interface area is derived from XRT reconstructions. The applicability of existing

interphase mass transfer correlations over the entire velocity range is explored and a new correlation between the hydrodynamic parameters and the interphase mass transfer is proposed.

- Lastly, the reaction investigation is expanded to include additional aspects like high-density particle fluidization and the effect of fines ([Chapter 5](#)). Fines are introduced into the sand particle system as well as into the high-density particle system.

Chapter 2 : Literature Review

2.1 Fluidized bed fundamentals

The basic concept of fluidization is the levitation of multiple particles using the terminal drag velocity (U_t) and an upwards-moving medium. For gas-solid fluidization this is achieved by introducing gas from the bottom of a packed bed of particles. At a certain superficial velocity (U_0) the local particle velocity reaches U_t , causing the particles to levitate. The bed adopts the characteristics of a liquid, hence the bed of particles “fluidizes”. In theory, this phenomenon of fluidization is simple and straightforward. Nevertheless, the velocity of fluidization (U_{mf}) is extremely low and for any practical applications an increase in throughput is unavoidable. It is these higher operating velocities that have preoccupied researchers for more than six decades. For a comprehensive background on fluidization, the following references can be consulted [42–44]. A short overview of relevant theory is given here.

One of the first ground-breaking classifications done in fluidization was that of Geldart [43]. [Figure 2.1](#) shows the four particle classifications.

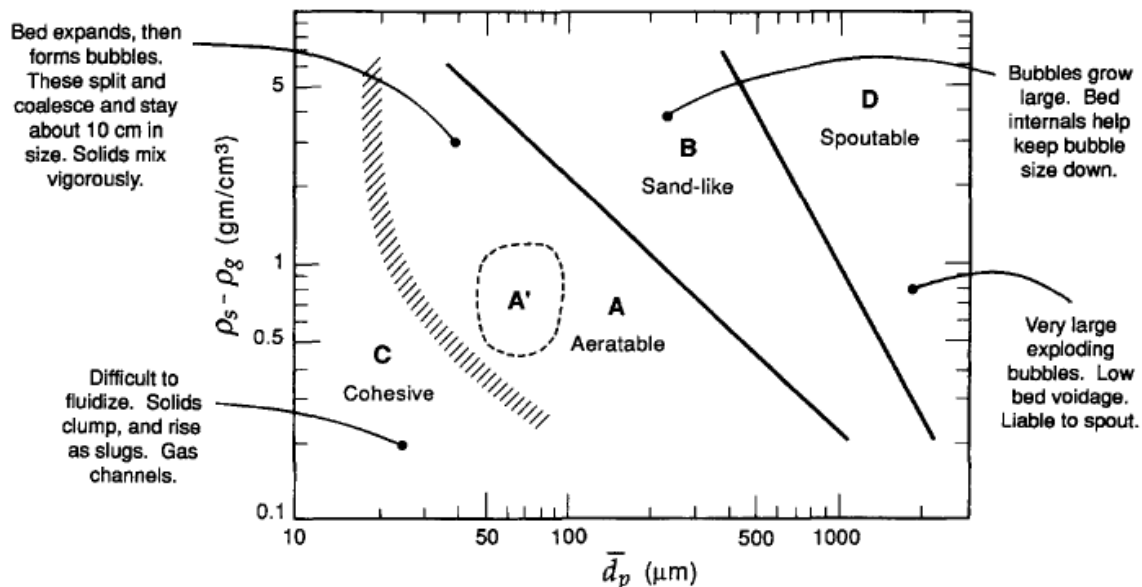


Figure 2.1: Geldart particle classification (taken from [45])

Several flow regimes can exist, depending on the Geldart particle classification and superficial velocity. The following flow regimes can occur in order of increasing superficial velocity (also indicated are the transition velocities where each regime starts):

- Particulate fluidization regime (U_{mf} – Minimum fluidization velocity)
- Bubbling regime (U_{mb} – Minimum bubbling velocity)
- Slugging
- Turbulent regime (U_c – Onset of turbulent regime)
- Fast fluidization regime (Several velocities defined – $U_k/U_{se}/U_{tr}$)
- Pneumatic transport regime

Particulate fluidization exists for Geldart A particles; for other particle systems U_{mf} and U_{mb} are the same velocity. Slugging occurs in the bubbling regime if the column diameter is insufficiently large [42]. To determine U_{mf} the Ergun equation can be used [44]:

$$150(1 - \varepsilon_{mf})U_{mf}^* + 1.75(U_{mf}^*)^2 d_p^* = \varepsilon_{mf}^3 (d_p^*)^2 \quad 2-1$$

or the Grace (1982) correlation [25]:

$$U_{mf} = \frac{\mu}{\rho_g d_p} (\sqrt{27.2^2 + 0.0408 Ar} - 27.2) \quad 2-2$$

Generally, fluidization is characterized by a lean phase and dense/emulsion phase. The lean phase is solids deprived and most of gas is located in this phase. The emulsion phase contains the majority of solids. In the bubbling regime the lean phase manifests as distinct bubbles which bubble through the emulsion phase. The terminal rise velocity of a single bubble is dependent on the bubble size:

$$U_{br} = 0.711 \sqrt{g D_b} \quad 2-3$$

In a freely bubbling bed the specific velocity of the lean phase/bubbles, U_b , is given by a velocity balance as done by Davidson and Harrison [9]:

$$U_b = U_o - U_{mf} + U_{br} \quad 2-4$$

The bubble fraction (ψ_B) in a fluidized bed can be determined using a solids phase balance:

$$\psi_B = \frac{\Phi_{mf} - \Phi_o}{\Phi_{mf}} \quad 2-5$$

A second method for calculating ψ_B (for fast bubbles) is to use a gas phase balance:

$$\psi_B = \frac{U_o - U_{mf}}{U_b - U_{mf}} \quad \text{for } U_o \gg U_{mf} \rightarrow \psi_B \approx \frac{U_o}{U_b} \quad 2-6$$

The onset of turbulent fluidization occurs at U_c . This is the superficial velocity at which the standard deviation of in-bed pressure fluctuations reaches a maximum. U_k is defined at

the point where the standard deviation reaches a plateau. [Figure 2.2](#) illustrates the expected trends in the standard deviation of pressure fluctuations. Arnaldos and Casal (1996) conducted a comprehensive study of available U_c and U_k correlations. They tested the accuracy of the correlations for different systems [46]. [Table 2-1](#) gives the top 7 U_c correlations. A state-of-the-art review of the turbulent regime was undertaken by Bi et al. [5] and can be referred to for a more detailed discussion on the matter.

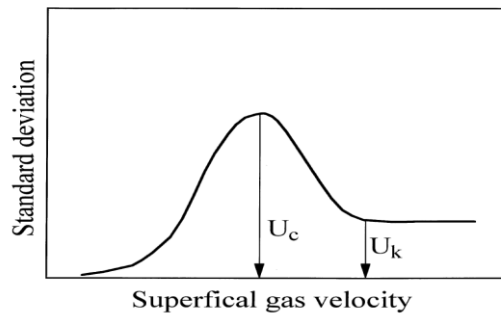


Figure 2.2: Standard deviation of pressure fluctuations used to define U_c and U_k [5]

Table 2-1: U_c correlations (as quoted by Arnaldos and Casal[46])

Authors	Correlation	Applicable range
Yang	$U_c = u_i(\epsilon_c)^m$ $u_i/u_t = 25.49(Re_t)^{-0.485}$ $m = 2.31(Re_t)^{-0.0457}$ $\epsilon_c = m - 1/m$	$33 < d_p < 49 \mu\text{m}$ $1070 < \rho_p < 1450 \text{ kg/m}^3$
Cai et al.	$U_c = (gd_p)^{0.5} \left[\frac{0.211}{D_t^{0.27}} + \frac{2.42 \times 10^{-3}}{D_t^{1.27}} \right] \left[\frac{D_t(\rho_s - \rho_g)}{d_p \rho_g} \right]^{0.27}$	-
Nakajima et al.	$Re_c = 0.633Ar^{0.467}$	-
Jin et al.	$U_c = (gd_p)^{0.5} \left[\frac{(KD_f)(\rho_s - \rho_g)}{d_p \rho_g} \right]^{0.27}$ $KD_f = 0.00367 \text{ (for free bed)}$	$50 < d_p < 1050 \mu\text{m}$ $700 < \rho_p < 2600 \text{ kg/m}^3$
Han et al.	$U_c = 60(\rho_p)^{0.56}(d_p)^{0.29}(D_t)^{0.53}$	$24 < d_p < 2600 \mu\text{m}$
Lee and Kim	$Re_c = 0.7Ar^{0.485}$	$0.44 < Ar < 4.4 \times 10^7$ $1.22 < Ar < 5.7 \times 10^7$
Horio	$Re_c = 0.936Ar^{0.472}$	$54 < d_p < 2600 \mu\text{m}$

Fast fluidization and pneumatic transport is also referred to as a Circulating Fluidized Bed (CFB). Fast fluidization is associated with a lean core annulus structure, dense outer annulus structure and high solids carryover. CFB reactors are generally designed with solids return systems. A few velocities have been used to define the start of fast fluidization. However, controversy exists due to the added possibility of controlling the solids circulation rate. The transport velocity (U_{tr}) is determined by keeping the linear velocity in the riser section constant, varying the solids circulation rate and measuring the pressure drop across the riser. This procedure is done for several velocities until a graph such as [Figure 2.3](#) is obtained.

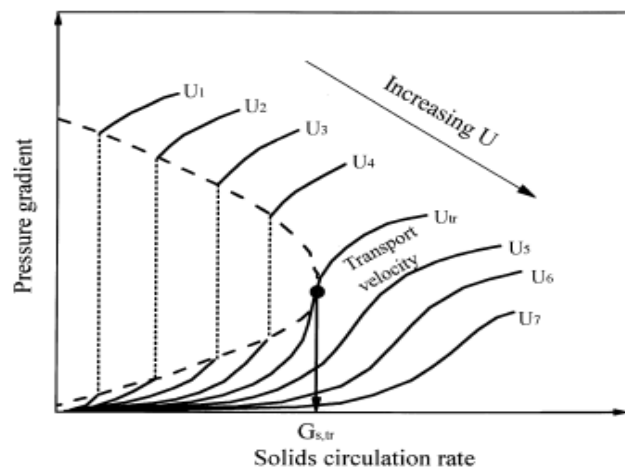


Figure 2.3: Definition of U_{tr} [5]

The significant entrainment velocity (U_{se}) is less involved and usually independent of the solids circulation rate. The operating velocity is increased until the solids carryover/entrainment rate (G_s) starts to increase significantly. [Figure 2.4](#) illustrates this:

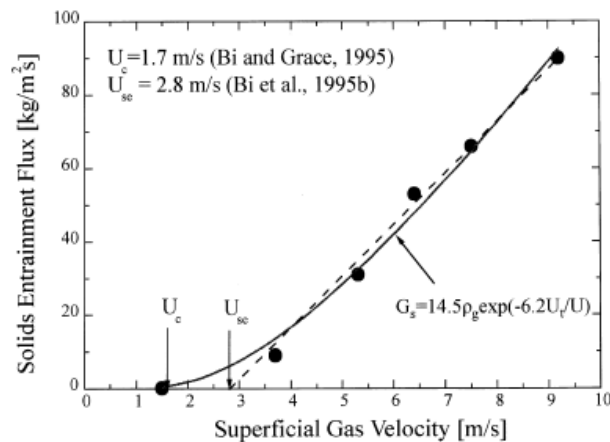


Figure 2.4: Definition of U_{se} [5]

2.2 Measuring methods

There are numerous measuring methods for fluidized beds, from pressure probes to nuclear particle tracking. Mudde [47] gives a review of the more advanced gas-liquid-solids measurement techniques. This review covers optical probes, Laser Doppler Anemometry (LDA), cross-sectional wire mesh sensors, Electrical Capacitance Tomography (ECT), X-Ray Densitometry, Gamma-Ray Densitometry and Nuclear Particle Tracking (CARPT and PEPT). The following section, however, will be limited to the techniques used in this study and their underlying concepts.

2.2.1 Pressure signals

The possible analyses of pressure signals in a fluidized bed stretch over the time domain, frequency domain and state-space, all giving valuable information [48]. The method described in this section is a frequency domain analysis technique. An example of a time domain analysis is the quantification method of U_c .

By using two pressure probes, one in the plenum chamber and the other in the bed, a measure of the bubble size can be determined [40,49]. The Power Spectral Density (PSD) function of each signal is used to decompose pressure fluctuations into global bed phenomena and phenomena in the vicinity of the pressure probe. These local phenomena are caused by the passing bubbles/voids. The PSDs of both pressure probe signals are compared and the coherence and incoherence of the two signals relative to each other are calculated. The standard deviation of the incoherent part of the signal (σ_i) is a measure of the average bubble/void size. [Figure 2.5](#) illustrates the analysis procedure. σ_i is directly proportional to the bubble size in the following manner:

$$D_b \propto \frac{\sigma_i}{\rho_b g} \quad 2-7$$

$$\therefore D_b \propto \frac{\sigma_i}{\rho_p(1-\epsilon_0)g} \quad 2-8$$

Using this technique Van der Schaaf et al. [49] showed that relative bubble sizes and slug lengths could be determined. The magnitude of the effects that fines have on bubble sizes was observed by Beetstra et al. [40] using this technique.

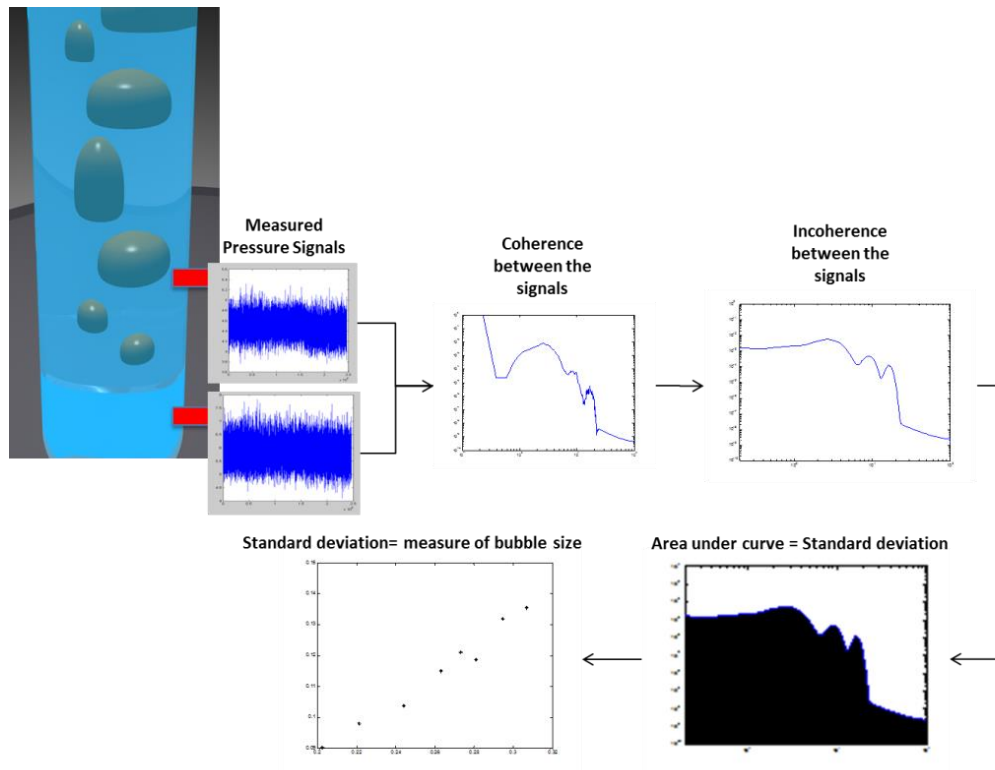


Figure 2.5: Graphical explanation of the non-intrusive void measurement technique using pressure signals. Signals are measured in the plenum chamber, in the bubbling fluidized bed and processed to obtain a measure of bubble size

2.2.2 Optical probes

Optical probes are very useful measuring devices as they have the capability of detecting solids concentrations [50–53]. They are, however, intrusive by nature. Generally, they consist of a thin tube containing two sets of optical fibres. The one set of fibres is connected to a light source and the second is connected to a light detector. The fibres run through the tube to the tip, which has a window. [Figure 2.6](#) illustrates the concept and shows the path that light would travel. Depending on the concentration of solids around the tip of the probe, a different amount of light would scatter back. This fact enables the possibility to measure the solids concentration.

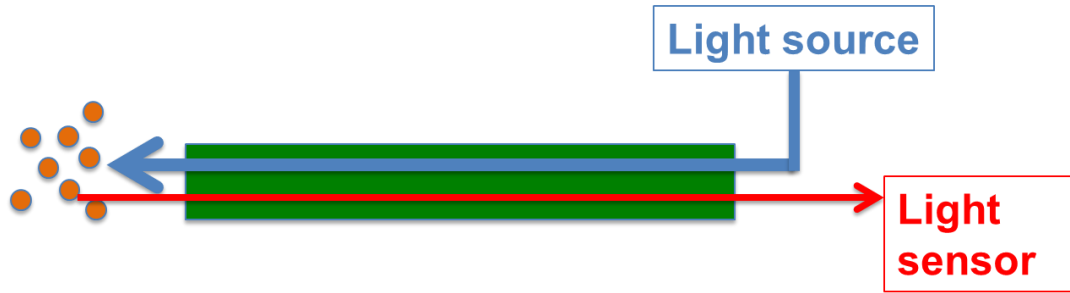


Figure 2.6: Illustration of the optical voidage probe

Rüdisüli et al. [50] and Zhang and Bi [52] used two optical probes separated by a small distance to measure void lengths in fluidized beds. Since bubbles have low solids concentrations, an optical probe can detect whether it is in contact with a bubble or not. [Figure 2.7](#) shows how these researchers determined the void length. As the void rises through the bed, it makes contact with the bottom (green) probe. And as the void continues to rise, contact is made with the top (red) probe. The signal response is shown. Using the lag between the two contact times and the distance between the probes, the rise velocity is determined. With the total bubble-probe contact time and the rise velocity known, the bubble length can be determined. Rüdisüli et al. [50] developed a bubble-linking algorithm for this measurement technique.

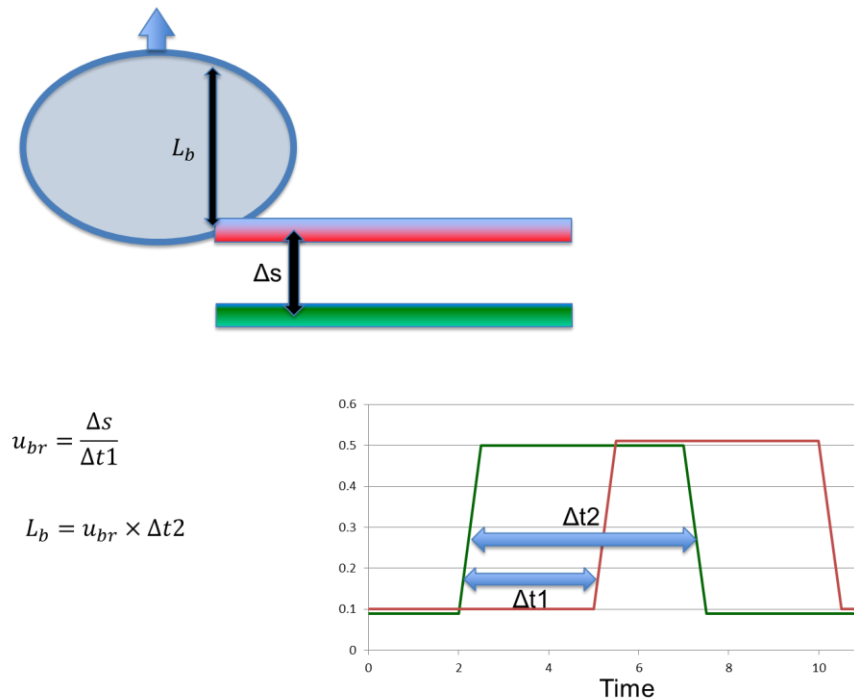


Figure 2.7: Explanation of how two probes are used to determine void bubble length

2.2.3 Tomography

One of the many non-intrusive measuring techniques is tomography devices. Tomography measures the cross-sectional solids concentration and with the aid of reconstruction algorithms cross-sectional “pictures” can be obtained. Electrical Capacitance Tomography (ECT) is a fast and relatively inexpensive method of tomography which is why it has been widely applied in recent years. ECT is, however, a soft-field technique, meaning that the gas-solids distribution influences the position of the field lines, resulting in relatively poor resolution at the centre of the bed. X-Ray Tomography (XRT) is a hard-field technique: the direction of a field line is not changed by the medium. Recent advances in faster responding X-ray detectors have made it possible to implement time-resolved cross-sectional measuring in fluidized beds [47].

These advances in XRT create the opportunity to reconstruct three-dimensional bubble shapes, leading to new insight into bubble behaviour. Bieberle [54] and Mudde [55,56] have proved the usefulness of the XRT technique for the bubbling regime. The setup developed by Bierberle [54] uses an electron beam which sweeps rapidly across a circular target around a column to produce a single moving X-ray beam which is then detected by stationary detectors around the fluidized bed. For a more detailed explanation, refer to the article. The setup developed by Mudde, used in this investigation, has three stationary X-ray tubes and detector arrays. The arrays contain top and bottom rows of detectors, creating two measurement planes and the means to determine bubble rise velocities. Rautenbach et al. [57] experimentally compared tomography techniques using this XRT setup in conjunction with an ECT-type setup. The advantages and disadvantages of each were listed and it was concluded that the choice between ECT and XRT lies in the type of information a researcher requires.

2.2.4 Ozone decomposition reaction

A popular tracer reaction used in fluidized bed research is the ozone decomposition reaction. Ozone decomposes to oxygen with a heat of reaction (ΔH_{298}) of -138 kJ/mol and a free energy of reaction (ΔG_{298}) of -163 kJ/mol, although ozone is thermally stable up to 523 K [58]. At ambient temperatures it has a very long half-life and the reaction needs to be catalysed. Both metals and metal oxides serve as good catalysts. Although metal oxides are preferred as they are easily impregnated onto many catalyst supports [59]. Most of these catalysts have varying deactivation trends which are influenced by factors such as the

presence of NO_x , humidity and oxygen, but all researchers have found that first-order kinetics apply [59–62]. Ozone is ideally suited for investigative reaction work in a fluidized bed since:

- Catalyst support options are unlimited.
- The reaction is first order.
- The reaction occurs at ambient temperatures.
- Ozone is detectable at low concentrations, resulting in negligible volume change.

The ozone decomposition reaction was used by Sun to investigate the effects of particle size distribution on reactor performance for the bubbling to fast fluidization regime [28,37,63–65]. Paglioloco et al. [66] used the ozone reaction to derive a design correlation for a CFB reactor. Schoenfelder et al. [67] tested a CFB reactor model using the ozone decomposition reaction. Therdthianwong et al. [68] continued the CFB work of Schoenfelder et al. Zimmermann and Taghipour [69] used computational flow dynamics (CFD) to predict ozone-based reactor performance, which was compared with the experimental data of Sun [64]. A more recent study using ozone was that of Fan et al. [70,71] on a new type of reactor called a Downer reactor.

As advantageous as the ozone decomposition reaction is, many researchers find it difficult to implement. The catalyst seems to be unpredictable and the activity is not constant from day to day. Dhandapani and Oyama [59] reported possible reaction mechanisms and described the reaction rate as a multi-parameter power law equation dependent on O_3 , H_2O and O_2 , although H_2O and O_2 do not react and will therefore merely influence the first-order reaction rate constant. From work on ozone-operated FBRs varying first-order reaction rate constants are reported. Most researchers ascribe them to catalyst deactivation, but Schoenfelder et al. [67] mentioned that both moisture content and temperature may have an effect on the kinetics.

2.3 Solids and voids behaviour

Although much is known about the void structure of bubbling and fast fluidization regimes, interest in the turbulent regime has only increased in the last two decades [5,53]. In this thesis emphasis is placed on studies which include the turbulent regime.

Zhang and Bi [52] used the two optical probe technique to measure void lengths in a turbulent fluidized bed. A Geldart A Fluid Catalytic Cracking (FCC) catalyst was used. They found radially uniform void lengths in the turbulent regime and proposed a new bubble

coalescence-splitting balance model. It was also noted that void lengths decrease with superficial velocity in the turbulent regime and increase with measurement height.

Ellis et al. [72] used single optical probes with different column diameters and FCC catalyst to investigate solids concentration in the bubbling and turbulent regimes. The voidage profile was asymmetrical close to the solids return inlet and bed surface; radial symmetry was observed for the rest of the bed. However, they reported some uncertainty due to the intrusive nature of the probes. Zhu et al. [53] installed three optical probes around the periphery of a fluidized bed at the same radial position. The bubbling and turbulent regimes were investigated for FCC powder. No radial symmetry for the voidage profile was observed in the bubbling regime whereas symmetry did exist in the turbulent regime. Du et al. [73] used optical probes in conjunction with ETC to investigate bed non-homogeneity using an FCC catalyst. They similarly found asymmetry for the bubbling regime and symmetry for the turbulent regime. Also, the observation was made that ECT and the optical probes yield considerably different results for the void phase fraction, depending on the signal's threshold level to distinguish between the emulsion and void phases.

A very comprehensive ECT study is that of Makkawi and Wright [74], which spanned several regimes. Glass ballotini particles (Geldart B) were used for the bubbling, turbulent and fast fluidization regimes and the aim was to define fluidization regimes based on these measurements. The investigation was limited to a shallow bed and axial measurements where not possible. The packed bed height and column diameter (13.8 cm) were equal [75]. There were two measuring planes 38 mm apart, with the bottom plane 76 mm from the distributor. Qualitative observations were made using the tomography images. The characteristic bubbles of the bubbling regime could be observed, as well as the core annulus structure of the fast fluidization regime. They found that bubbles break up into smaller voids at the turbulent regime transition. This is in agreement with the optical probe observations of Zhang and Bi [52]. Quantitative solids concentration measurements were also reported. [Figure 2.8](#) shows the average cross-sectional solids concentrations as the velocity increases for the top and bottom planes of measurement.

Brouwer et al. [76] used the fast XRT setup to investigate the effects of elevated pressure on bubble behaviour. Exceptional agreement was found between the bubble size results and correlations, as shown in [Figure 2.9](#), although the bubble velocity (U_b) was lower than predicted by the correlation.

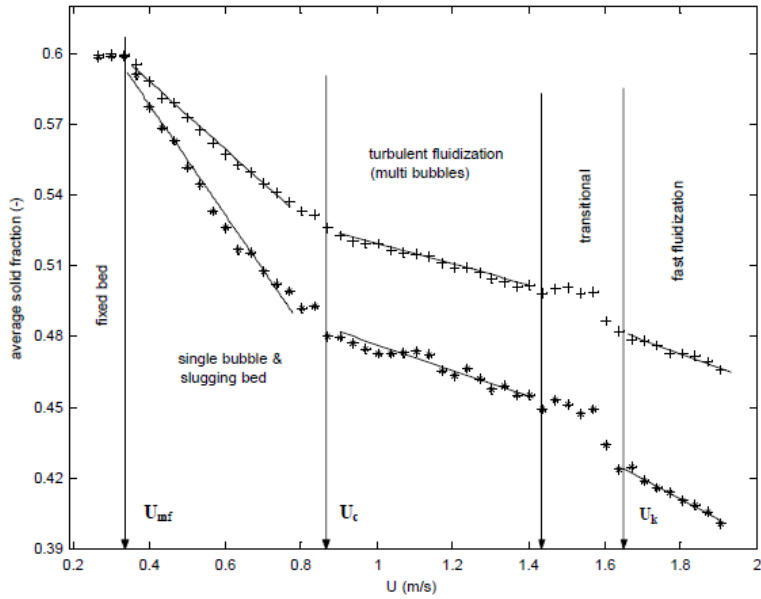


Figure 2.8: Average cross-sectional solids concentrations as the velocity increases for the top (+) and bottom (*) measurement planes [74]

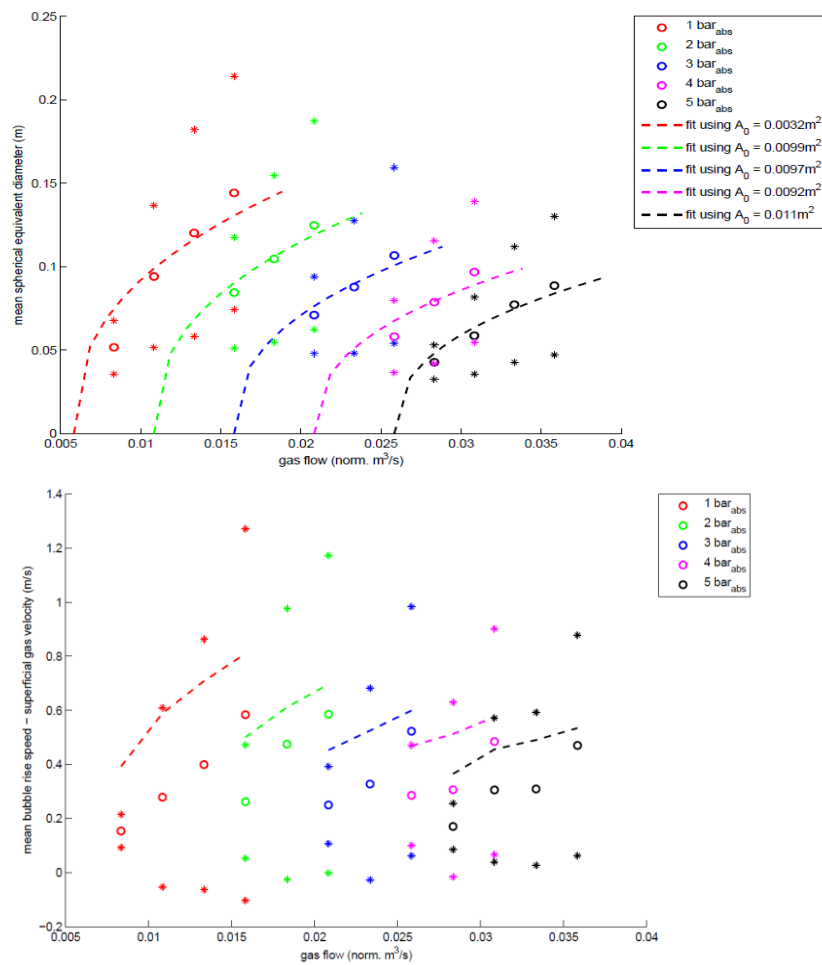


Figure 2.9: Bubble size (top) and bubble velocity (bottom) results of Brouwer et al. [76]. The XRT technique shows very good agreement with bubble size. Circles (o) represent bubble means and asterisks (*) one standard deviation. The dashed lines are the predicted values

2.3.1 Fines

The addition of fines in gas-solid fluidized beds has long been known to introduce desirable features into reactors. In industry, fines are mostly generated via attrition during normal reactor operation. For bubbling fluidized beds, a decrease in bubble size and an increase in emulsion-phase voidage have been reported. This is in agreement with a longer collapse time for fluidized beds containing higher fines [31–34]. The mechanisms by which the addition of fines influences the hydrodynamics are still unclear. Some research suggests that in gas-solid fluidized beds the particles tend to form stable agglomerates when they are smaller than 20–40 μm [35]. From Scanning Electron Micrograph (SEM) images it was found that fine particles adhered to coarse particles or formed agglomerates [36]. Other effects of fines include the decrease of the velocity at which the turbulent fluidization regime starts [37–39]. Furthermore, the effect of fines on elutriation from fluidized beds was found to depend on the size and proportion of fines, as well as the gas velocity [35]. A more recent and systematic study has shown the influence of particle size distribution and the addition of fines on the hydrodynamic behaviour of Geldart A particles [40].

The change in hydrodynamics with addition of fines has also been proved to increase conversion in a catalytic reaction system. Yates and Newton [41] added 16% and 27% fines to a bed of Geldart A commercial oxidation catalyst, where fines were defined as particles $<45 \mu\text{m}$. The investigation found that reactor performance increased due to an increase in emulsion-phase voidage. The voidage increase caused a shift in the gas flow pattern: more gas was flowing through the emulsion phase and less in the lean phase. Further experimental evidence was reported by Sun and Grace [28] on the disproportionate increase of fines contained in bubbles, contributing to better chemical conversion with a wider particle size distribution [37]. The study was conducted with a narrow, bimodal and wide particle size distribution of Fluid Catalytic Cracking (FCC) catalyst. Fines were defined as particles smaller than 20% of the Sauter mean particle size.

2.4 Fluidized bed reactor models

As mentioned, at its simplest, a fluidized bed reactor can be described as a dense (solids-containing) emulsion phase with a lean (solids-free) phase bubbling through it. Reactant, mostly in the lean phase, is transported to the emulsion phase via mass transfer where reaction can occur. Even though single-phase reactor models with axial dispersion have also

been used before, these are not phenomenologically correct. Generally, these models are used for the turbulent regime as the single-phase assumption works well for a turbulent reactor, although Foka et al. [30] showed that two-phase models can also work. A comprehensive review of reactor models is given by Mahecha-Botero et al. [77].

2.4.1 Basic two-phase model

By assuming negligible gas flow through the emulsion phase and no solids content in the bubbling phase, the following mass balance can be done based on the solids volume of the catalyst:

$$C_i = u_B C_{i,B} + u_E C_{i,E} \quad 2-9$$

$$A_{bed} u_B \frac{dC_{i,B}}{dW_v} = -K_O (C_{i,B} - C_{i,E}) \quad 2-10$$

$$A_{bed} u_E \frac{dC_{i,E}}{dW_v} = -R_i(C_E) + K_O (C_{i,B} - C_{i,E}) \quad 2-11$$

Where R_i is the reaction rate, for first-order reactions it would be:

$$R_i(C) = k_r C \quad 2-12$$

For this model the mass transfer coefficient is an overall coefficient and has the same units as k_r , which is based on the rate of total volumetric gas transfer per solids volume.

2.4.2 Three-phase model

There is a cloud phase around the bubble that Kunii and Levenspiel postulate has a significant effect on modelling and mass transfer [44]. A mass balance based on this model would look as follows:

$$C_i = u_B C_{i,B} + u_C C_{i,C} + u_E C_{i,E} \quad 2-13$$

$$u_B \frac{dC_{i,B}}{dz} = \phi_B R_i(C_B) - K_{BC} \psi_B (C_{i,B} - C_{i,C}) \quad 2-14$$

$$u_C \frac{dC_{i,C}}{dz} = \phi_C R_i(C_C) + K_{BC} \psi_B (C_{i,B} - C_{i,C}) - K_{CE} \psi_B (C_{i,C} - C_{i,E}) \quad 2-15$$

$$u_E \frac{dC_{i,E}}{dz} = \phi_E R_i(C_E) + K_{CE} \psi_B (C_{i,C} - C_{i,E}) \quad 2-16$$

Here K_{BC} and K_{CE} are based on total gas transfer rate per bubble volume.

2.4.3 Bubbling-turbulent model

The turbulent regime is more easily modelled by means of axially dispersed plug flow. For the bubbling-turbulent regime one would have to change the approach and a single model which would work well for both regimes was found not to be possible. However, Thompson et al. published a transitional model whereby probabilistic averaging is used to create a two-phase model for low velocities and an axially dispersed plug flow model for velocities beyond U_c [25].

Using the two-phase model of Grace [20], which has axial dispersion in both phases, several parameters were varied as the probability of being in the turbulent regime changed. The mass balances and equations are as follows:

Mass balances:

$$C_i = q_L C_{i,L} + q_H C_{i,H} \quad 2-17$$

$$u_L \frac{dC_{i,L}}{dz} = D_{z,L} \frac{d^2 C_{i,L}}{dz^2} + \phi_L R_{i,L}(C_L) - k_q a_I \varepsilon_L (C_{i,L} - C_{i,H}) \quad 2-18$$

$$u_H \frac{dC_{i,H}}{dz} = D_{z,H} \frac{d^2 C_{i,H}}{dz^2} + \phi_H R_{i,H}(C_H) + \left(\frac{\psi_L}{\psi_H}\right) k_q a_I \varepsilon_L (C_{i,L} - C_{i,H}) \quad 2-19$$

The boundary conditions at the inlet ($z=0$):

$$u_L (C_{i,L,z=0^+} - C_{i,IN}) = D_{z,L} \frac{dC_{i,L}}{dz} \Big|_{z=0} \quad 2-20$$

$$u_H (C_{i,H,z=0^+} - C_{i,IN}) = D_{z,H} \frac{dC_{i,H}}{dz} \Big|_{z=0} \quad 2-21$$

The boundary conditions at the outlet ($z=H_b$):

$$\frac{dC_{i,L}}{dz} \Big|_{z=H_b} = 0 \quad 2-22$$

$$\frac{dC_{i,H}}{dz} \Big|_{z=H_b} = 0 \quad 2-23$$

The parameters that need to be calculated depending on the probability of being in the turbulent regime are:

$$u_L = (1 - [P_T(U)])u_b(U) + [P_T(U)] \cdot U_0 \quad 2-24$$

$$D_{z,L} = (1 - [P_T(U)])D_m + [P_T(U)] \cdot \frac{U_0 H_b}{Pe(U)} \quad 2-25$$

$$\phi_L = (1 - [P_T(U)])\phi_{L,0} + [P_T(U)] \cdot \phi(U) \quad 2-26$$

2.5 Mass transfer

As with most multiphase reactors, modelling a fluidized bed is difficult due to the complex hydrodynamic behaviour. Since the concept of two-phase theory was introduced, interphase mass transfer has been investigated. Two-phase theory is now generally accepted as the best modelling approach [23,25,26]. Before attempting to understand the mechanisms of interphase mass transfer and correlation approaches, background in fluid flow around a void is needed. Davidson and Harrison [9] developed equations that explained many aspects of bubble behaviour. Using a continuity equation of particles, relative velocities and pressure gradients, they derived fluid stream functions around a spherical void:

$$\psi_f = \left(U_{br} - \frac{u_{mf}}{\epsilon_{mf}} \right) \left(1 - \left(\frac{R_p}{r} \right)^3 \right) \frac{r^2 \sin^2 \theta}{2} \quad 2-27$$

Where R_p is given by:

$$R_p = \left(\frac{U_{br} + 2 \left(\frac{u_{mf}}{\epsilon_{mf}} \right)}{U_{br} - \left(\frac{u_{mf}}{\epsilon_{mf}} \right)} \right)^{\frac{1}{3}} \cdot \left(\frac{D_b}{2} \right) \quad 2-28$$

R_p has a physical significance in that it represents the radius of penetrations or rather the cloud radius. Gas penetrates the roof of the bubble, circulates downwards in the cloud phase and re-enters at the base of the bubble. It is assumed that this cloud of solids moves with the bubble. Using the streamline equations, Davidson and Harrison found that the gas exchange rate between bubble and cloud due to this convection (through flow) process should be:

$$q_{bc} = 3\pi \left(\frac{D_b}{2} \right)^2 u_{mf} \quad 2-29$$

Based on the surface area of a bubble, this becomes:

$$\frac{q_{bc}}{S_b} = \frac{3}{4} u_{mf} \quad 2-30$$

Murray also did the same type of analysis but found the through flow to be [16]:

$$\frac{q_{bc}}{S_b} = \frac{1}{4} u_{mf} \quad 2-31$$

Penetration theory is mathematical derivations that consider the diffusive components of gas into and out of a bubble. Generally, two equations are used: the Davidson and Harrison [9] equation, derived for a fluidized bed, and the Higbie penetration theory [78], derived for a gas-liquid system. Continuing their work with streamlines, Davidson and Harrison

theoretically calculated the diffusion from the curved surface of a spherical-cap bubble. The equation they arrived at for bubble-to-cloud diffusion was:

$$k_{bc} = 0.975 \left(\frac{D_m^{\frac{1}{2}} g^{\frac{1}{4}}}{D_b^{\frac{1}{4}}} \right) \quad 2-32$$

Since gas-solid fluidized beds are analogous with gas-liquid systems, the Higbie penetration theory can also be used with some modification. This is done in an attempt to explain transfer from the cloud into the emulsion phase. Higbie [78] derived the following equation:

$$k_{gl} = \left(\frac{4D_{gl}}{\pi t_e} \right)^{\frac{1}{2}} \quad 2-33$$

where k_{gl} is the mass transfer of gas into the liquid, D_{gl} is the diffusion coefficient of gas in liquid and t_e is the time since exposure. The above equation was adapted for a gas-solid fluidized system:

$$k_{ce} = \left(\frac{4D_e \varepsilon_{mf}}{\pi t_e} \right)^{\frac{1}{2}} \quad 2-34$$

Then, given that the exposure time of a bubble surface element to the emulsion phase is [43]:

$$t_e = \frac{2R_p}{U_{br}} \approx \frac{D_b}{U_{br}} \quad 2-35$$

The effective diffusivity (D_e) can be approximated with the molecular diffusivity (D_m), hence the Higbie penetration theory equation for a fluidized system is arrived at:

$$k_{ce} = \left(\frac{4D_m \varepsilon_{mf} U_{br}}{\pi D_b} \right)^{\frac{1}{2}} \quad 2-36$$

2.5.1 Mass transfer correlations

One of the first proper review articles on mass transfer was written in by Drinkenburg and Rietema [13]. In the review the authors represent all the possible resistances to mass transfer in a scheme similar to that of [Figure 2.10](#). Mass transfer can occur by diffusion between the three phases, convection between bubble and cloud as suggested by Davidson and Harrison and convection from cloud to emulsion via gas absorption onto the particles and then “cloud shedding”. However, Chavarie and Grace found that this last phenomenon does not occur for a single rising bubble [14]. There are two types of mass transfer correlation: the first is based

on boundary layer equations and the second on penetration theory. In an ideal model all the resistances would be considered and the concentration of each phase would be calculated individually. But different researchers have made specific assumptions to correlate mass transfer.

2.5.1.1 Boundary layer theory correlations

Partridge and Rowe assumed that $R_0=R_1=R_2=0$ with $C_b=C_c$, which resulted in a boundary layer-type correlation [13]:

$$Sh_c = 2 + 0.69Sc^{1/3}Re_c^{1/2} \quad 2-37$$

$$\frac{k_{be}a_I\psi_B D_b}{\varepsilon_0 D_m} = 2 + 0.69 \left(\frac{\mu_g}{D_m \rho_g} \right)^{1/3} \left(\frac{\rho_g U_{br} D_b}{\mu_g} \right)^{1/2} \quad 2-38$$

For large bubbles and high Re numbers the equation would simplify as follows, very similar to the Davidson and Harrison penetration model [13]:

$$k_{be} = 0.58\varepsilon_0 \left(\frac{D_m^{1/2} g^{1/4}}{D_b^{1/4}} \right) \quad 2-39$$

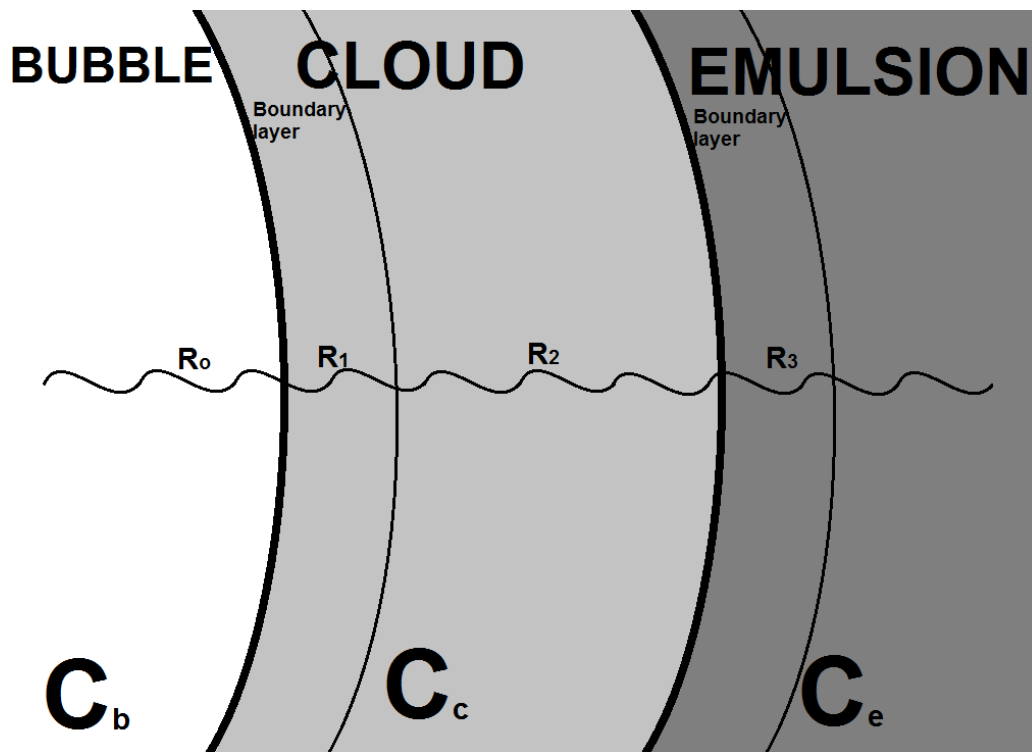


Figure 2.10: Schematic representation of possible resistance to mass transfer

The mass transfer correlation of Foka et al. [30] is also based on boundary layer theory. The researchers applied the two-phase model of Van Deemter (1961) to their data and the following correlation, spanning both bubbling and turbulent regimes, was derived:

$$k_{be}a_l = 1.631Sc^{0.37}U_0 \quad 2-40$$

2.5.1.2 Penetration theory correlations

Drinkenburg and Rietema showed that the assumption $C_b=C_c$ made for boundary layer theory does not hold and even more so when there is a chemical reaction taking place. By assuming $R_1=R_2=R_3=0$ with $C_c=C_e$, Davidson and Harrison combined their through flow and penetration model:

$$k_{be} = 0.75U_{mf} + 0.975 \left(\frac{D_m^{\frac{1}{2}}g^{\frac{1}{4}}}{D_b^{\frac{1}{4}}} \right) \quad 2-41$$

Kunii and Levenspiel merely assumed $R_1=R_2=0$ and used individual values for C_b , C_c and C_e . In essence, this results in two mass transfer steps in series. For the bubble-to-cloud step they used the same correlation as Davidson and Harrison. For the cloud-to-emulsion step they used the Higbie (1935) approximation for fluidized beds:

$$k_{bc} = 0.75U_{mf} + 0.975 \left(\frac{D_m^{\frac{1}{2}}g^{\frac{1}{4}}}{D_b^{\frac{1}{4}}} \right) \quad 2-42$$

$$k_{ce} = \left(\frac{4D_m\varepsilon_{mf}U_{br}}{\pi D_b} \right)^{\frac{1}{2}} \quad 2-43$$

Basing mass transfer on the bubble volume instead of the bubble surface area (multiplying the coefficients by $6/D_b$) gives the well-known Kunii and Levenspiel correlations:

$$K_{bc} = 4.5 \frac{U_{mf}}{D_b} + 5.85 \left(\frac{D_m^{\frac{1}{2}}g^{\frac{1}{4}}}{D_b^{\frac{1}{4}}} \right) \quad 2-44$$

$$K_{ce} = 6.77 \left(\frac{D_m\varepsilon_{mf}U_{br}}{D_b^3} \right)^{\frac{1}{2}} \quad 2-45$$

By knowing that these transfer steps are in series, the overall mass transfer can be calculated using:

$$\frac{1}{K_{be}} = \frac{1}{K_{bc}} + \frac{1}{K_{ce}} \quad 2-46$$

This correlation was verified using tracer experiments on non-reacting systems. Kunii and Levenspiel emphasized that K_{bc} and K_{ce} need to be kept separate for adsorbing or reacting systems. The changing concentration gradient in the cloud phase due to reaction prevents the simplification to K_{be} using the above equation. Hence, the three-phase reactor model was introduced.

Most mass transfer correlations take the form discussed thus far: the “Davidson and Harrison”– or “Murray”– through flow combined with either the “Davidson and Harrison” – or “Higbie” – penetration equations. Most of these mass transfer correlations are only verified using non-reacting tracer experiments with single rising bubbles. A very reliable experimental technique was established in the late 1970s early 1980s at the University of British Columbia, Canada under the guidance J.R Grace, even though it had the limitation of being conducted in a pseudo-2D column. Chavarie and Grace [14] were the first to use this setup and it was later perfected by Sit and Grace [15,16]. The bed, packed with non-reactive particles, is incipiently fluidized with ozone-free air. Ozone-rich air is then continuously pulse-injected at the bottom of the column, creating bubbles containing ozone. Using a movable ultraviolet (UV) source and a photometer, the ozone concentration in the bubbles can be determined at different heights as the bubbles rise through the bed. Sit and Grace found that bubble shape plays an important role [15], as does bubble coalescence [16]. The correlation they used to fit their data was based on Murray through flow and Higbie penetration:

$$3D\text{-column:} \quad k_{be} = \frac{1}{4}U_{mf} + \left(\frac{4D_m\varepsilon_{mf}U_{br}}{\pi D_b}\right)^{\frac{1}{2}} \quad 2-47$$

$$2D\text{-column:} \quad k_{be} = \frac{1}{\pi}U_{mf} + \left(\frac{4D_m\varepsilon_{mf}U_{br}}{\pi D_b}\right)^{\frac{1}{2}} \quad 2-48$$

Notice the difference in the convection terms; this is not due to geometric differences. When doing streamline theory, the final equation looks slightly different for a two-dimensional flat bubble vs. a three-dimensional spherical bubble. To account for bubble shape, Sit and Grace suggested multiplying k_{be} by the square root of the width-to-length ratio of the bubble [15]:

$$3D\text{-column:} \quad k_{be} = \frac{\sqrt{\tau}}{4}U_{mf} + \left(\frac{\sqrt{\tau}4D_m\varepsilon_{mf}U_{br}}{\pi D_b}\right)^{\frac{1}{2}} \quad 2-49$$

In the follow-up article, bubble interaction was more closely investigated [16]. Using the results for different sized particles (90 μm –390 μm , meaning different U_{mf}), they postulated

that bubble interaction causes an increase in the through flow and they adapted the correlations as follows:

$$3D\text{-column:} \quad k_{be} = \frac{1}{3} U_{mf} + \left(\frac{4D_m \varepsilon_{mf} U_{br}}{\pi D_b} \right)^{\frac{1}{2}} \quad 2-50$$

$$2D\text{-column:} \quad k_{be} = 0.4 U_{mf} + \left(\frac{4D_m \varepsilon_{mf} U_{br}}{\pi D_b} \right)^{\frac{1}{2}} \quad 2-51$$

Systems with big particles (large U_{mf}) will have a dominating convection term, and systems with small particles will be more diffusion dominated. This may explain why some correlations do not contain a convection term.

2.5.2 Performance of correlations

Wu and Agarwal looked at the effects of temperature in a fluidized bed using particles from 264 μm to 463 μm . [27] This was very similar to the Sit and Grace [16] experiment, except that it was done in a 127 mm ID column and argon was used as a tracer. Single argon bubbles were created near the distributor using a tube inserted from the top of the bed. A sample tube near the top of the bed would then extract a sample of the bubble gas as the bubble passes the sample tube. Experiments were conducted at 298 K, 423 K, 573 K and 773 K, and the Sit and Grace [16] and Davidson and Harrison [9] correlations were tested. Wu and Agarwal [27] found that the Sit and Grace correlation performed better, but in some cases was not ideal. They incorporated a correction factor for the convection term.

When it comes to reactions in a freely bubbling bed, concentration gradients steepen due to reaction in the cloud phase and bubble interaction starts playing a big role. Therefore it might be expected that these correlations do not perform ideally. Yet little work in this regard has been done. Thompson et al. used the data of Sun in a new transitional two-phase model [25,28]. They had to incorporate a correction factor to the Sit and Grace [16] correlation to fit the data. This might be due to the effect of the probabilistic transition factor. Campos et al. performed reactor performance experiments in a coke combustor at 1 223 K and inferred mass transfer using two-phase theory [29]. They combined the overall mass transfer correlations for K_{be} of Kunii and Levenspiel and found that the correlations far overpredicted mass transfer, although, as mentioned, Kunii and Levenspiel do warn that their three-phase model cannot be reduced to a two-phase model for reacting systems.

Chapter 3 : Tomography

Gas-solid fluidized beds have complex hydrodynamics and solid distributions. Understanding these parameters' fundamental behaviour is important to gain insight into gas-solid contacting and, in turn, reactor performance. Before exploring the reactor performance, this work started with an advanced tomography investigation into the hydrodynamics of multiple regimes. The aim was to gain insight into the structure of the bed, with the focus on the bubbling regime up to the turbulent regime. Geldart B sand particles were used. In the Introduction ([Chapter 1](#)) this particle system was referred to as the “sand baseline system”.

Different methods have been used to measure solids distributions and void structures, among which tomography is a useful and non-intrusive technique. The hydrodynamics of the bubbling and fast fluidization regimes are quite well understood, but interest in the turbulent regime has only increased strongly in the last two decades. Proper understanding of the flow structures in turbulent beds is still in its infancy, with the initial investigations employing optical probes and Electrical Capacitance Tomography (ECT) techniques [53,72,74,79]. ECT is a fairly inexpensive method of tomography, although resolution to the centre of the bed is relatively poor [80]. This disadvantage is due to the fact that ECT is a soft-field technique, which means that the gas-solids distribution influences the position of the field lines. Fast X-Ray Tomography (XRT) does not suffer this disadvantage. XRT is a hard-field technique. Recent advances in fast XRT make it possible to implement time-resolved cross-sectional measuring in fluidized beds [47]. The fast XRT technique has proved useful for visualizing bubbles at low operating velocities and in previous work it was shown that reliable cross-sectional solids concentration measurements can be obtained using fast XRT [55,56,80,81]. These advances create the opportunity for new insights into bubble behaviour and cross-sectional solids distribution.

In this chapter the cross-sectional solids concentration profiles are determined and are compared with the literature. Faster dynamics in cross-sectional solids distributions are expected for the turbulent and fast fluidization regimes and the abilities of XRT in these regimes is explored. The quality of tomographic reconstruction and void visualisations in these regimes also require examination. The flow structures of the bubbling, turbulent and fast fluidization regimes are observed and the validity of two-phase theory is considered.

3.1 Experimental

This investigation was conducted in an acrylic column 0.14 m in diameter and 1.4 m high with two cyclones in series at the outlet. Captured solids were returned to the column via a dipleg, which had a T-valve. The valve was operated at a constant gas flow rate of 100 l/min. Two absolute-pressure sensors were installed; each logged data at 1 000 Hz. One pressure sensor was in the plenum chamber and the other 0.07 m above the distributor. This entire setup was on a hydraulic-jack platform. This enables the column-cyclone setup to be moved upwards and downwards. Positioned around this column setup were three stationary X-ray sources. Opposite to each X-ray source was a detector array; each array had a top and bottom row of 32 detectors, creating 64 lines of measurement through the column per source. This arrangement also resulted in two measuring planes separated by approximately 10.9 mm. Using the hydraulic-jack platform the column setup could be moved to change the relative position of the measuring planes from the distributor.

All 192 X-ray detectors recorded at a rate of 2 500 Hz. The basic setup was the same as the one used by Mudde [56], with the exception of a smaller column and source circle diameter [47,55]. For more details on X-ray physics, please refer to these articles. [Figure 3.1](#) schematically illustrates the setup as viewed from the top and side, and [Figure 3.2](#) shows photos of the actual setup. At a specific superficial velocity and measuring height signals were logged for 300 s; Makkawi and Wright [5] recommend at least 120 s. The column was filled with sieved sand particles, having a Sauter mean diameter of 101 μm and a solids density of 2 530 kg/m^3 , to a static bed height of 0.50 m. The sand was sieved to exercise control over the particle size in the case of additional particle preparation for the study which is discussed in [Chapter 4](#). The achievable velocity range of the setup is 0.11 m/s up to 2.6 m/s. Four measuring heights above the distributor were investigated: 0.20 m, 0.30 m, 0.40 m and 0.50 m.

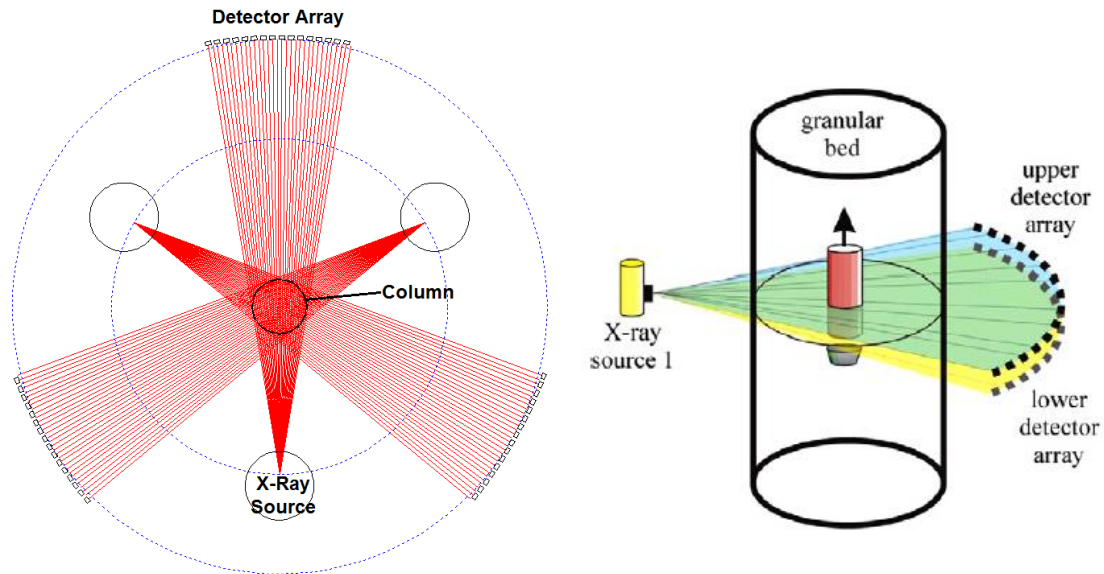


Figure 3.1: Top view of the fast XRT setup showing the three detector arrays and sources. Side view showing a single upper and lower detector array (taken from Brouwer et al. [76])

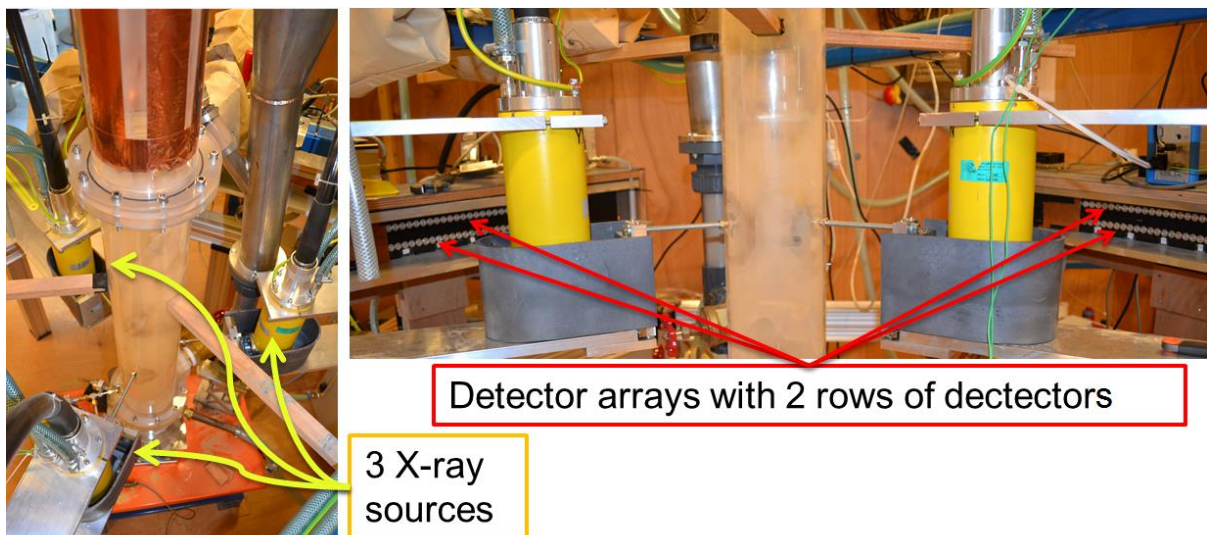


Figure 3.2: Photographs from the top and side of the setup

Figure 3.3 illustrates the first 16 measuring lines of a single source. The attenuation on each line is compared with that of packed bed and translated into line solid fraction (Φ_i). A calibration was performed for each individual detector. Calibration points were obtained by placing a thin acrylic partition in the column at different positions and filling one side with material. Partition positions are indicated by the horizontal lines in Figure 3.3. Using the following calibration function, A_{cal} , B_{cal} and C_{cal} can be determined for each individual detector:

$$I_{Xray} = A_{cal} + B_{cal} \exp\left(-x/C_{cal}\right) \quad 3-1$$

where I_{xray} is the beam intensity and x is the amount of material between the source and detector. [Appendix A](#) reports the calibration constants and shows the curves.

A weighted average between all 32 lines is calculated to obtain a cross-sectional solids fraction (Φ). The weighting factor is based on each detector's line length (l_i) penetrating the bed. An average is taken between the values obtained from each detector-source pair:

$$\Phi = \frac{1}{3} \left\{ \left(\sum_{i=1}^{32} \frac{l_i}{l_T} \Phi_i \right)_{\text{source1}} + \left(\sum_{i=1}^{32} \frac{l_i}{l_T} \Phi_i \right)_{\text{source2}} + \left(\sum_{i=1}^{32} \frac{l_i}{l_T} \Phi_i \right)_{\text{source3}} \right\} \quad 3-2$$

where: $l_T = \sum_{i=1}^{32} l_i$

For these calculations 5 min of data were processed for both the top and bottom measurement planes. [Figure 3.4a](#) illustrates the resulting cross-sectional solids concentration measurement. Movement of a void (or void agglomerates) through the planes is associated with a drastic drop in solids concentration. A time lag of voids crossing the detection planes is clearly observed in [Figure 3.4a](#).

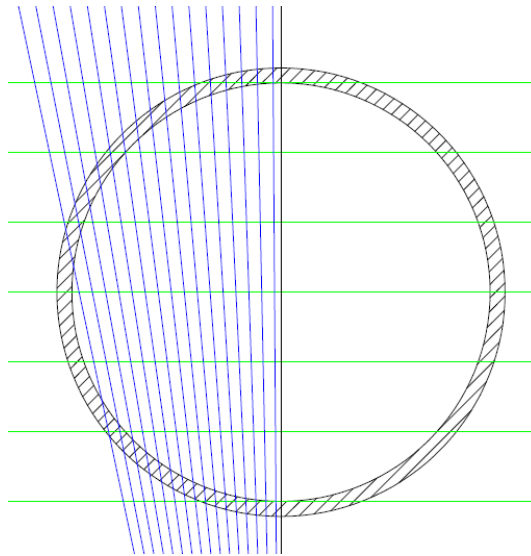


Figure 3.3: Position of 16 measuring lines (half of a single detector array). Horizontal lines indicate the positions of the partitions used for calibration

An average void rise velocity (\bar{u}_v) can be determined using the signals of both the bottom and top planes. A method similar to the bubble linking algorithm of Rüdüsüli et al. (9) is used. The Sum of Squared Differences (SSD) between the bottom and top planes can be calculated using both 5 min signals. The whole top plane signal is then shifted in time until a minimum in the SSD is obtained. [Figure 3.4](#) illustrates this technique: (a) is the original signals, (b) and

(c) are the same signals, with the exception of the top plane signal being shifted in time, and (d) shows the SSD as the top plane signal is shifted. **a**, **b** and **c** indicate the SSDs of [Figure 3.4a](#), [Figure 3.4b](#) and [Figure 3.4c](#). The best agreement between the bottom and top signals is achieved at point **b**. At this time shift the SSD is at a minimum. This time shift value can be interpreted as the averaged time that voids take to move from the bottom plane to the top plane. By knowing the distance between the two planes a velocity can be calculated (\bar{u}_v). Each bubble will have its own rise velocity depending on its size; \bar{u}_v is, however, the time-averaged void rise velocity.

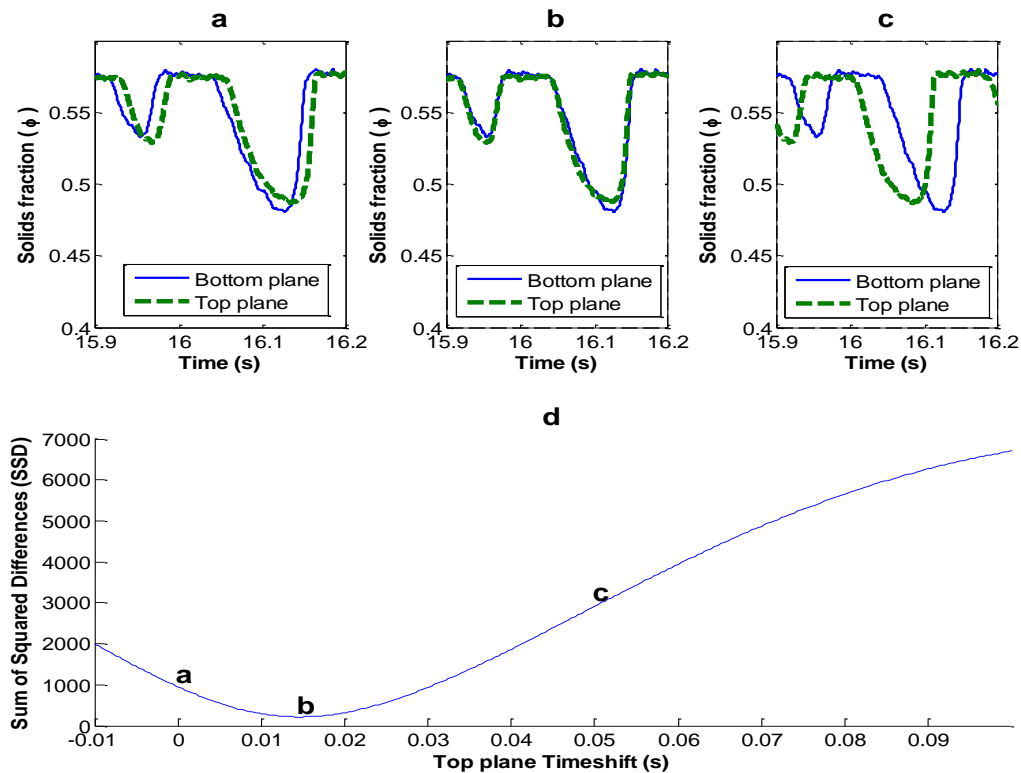


Figure 3.4: (a) is an example of the calculated cross-sectional solids concentration signal obtained for both the top and bottom measuring planes; the example is taken from the measurement done at 200 mm above the distributor and at a velocity of 0.11 m/s. (b) and (c) show the same signal, except that the top plane's signal is shifted in time. (d) is the calculated SSD between the top and bottom plane signals at different top plane time shifts

3.2 Results and discussion

3.2.1 Regime quantification

The standard deviation of pressure fluctuation at the different velocities is shown in [Figure 3.5](#). The measurements were repeated three times and the average was calculated for each velocity. The transition from bubbling to turbulent (U_c) is defined as the velocity at which the standard deviation reaches a maximum. This is the point at which the amplitude of the pressure fluctuation is at its largest. Using this method, U_c was determined to be 0.65 m/s. [Table 3-1](#) reports the top four Geldart B U_c -correlations according to Arnaldos and Casal [46]. Also reported are their individual predictions for this specific system. Proper agreement is obtained.

Using the technique discussed in Section [2.2.1](#), the coherence between the pressure measurement signal in the plenum chamber and in the bed is calculated [49]. The standard deviation of the incoherent part of the pressure signal is a measure of void sizes. It can be seen that the voids grow as the superficial velocity is increased in the bubbling regime and reach a maximum stable size in the turbulent regime. The sudden increase is due to the core-annulus structure which forms in the centre of the reactor; this is considered to be the start of the fast fluidization regime and is indicated on [Figure 3.5](#) as U_k . The U_k value is determined to be 1.19 m/s.

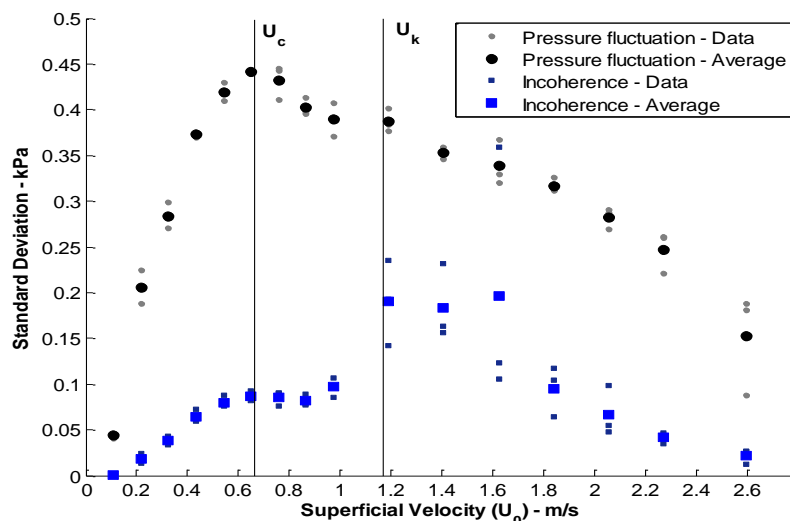


Figure 3.5: Standard deviation of pressure fluctuations, showing the bubbling to turbulent regime transition (U_c) at 0.65 m/s. Also shown is the standard deviation of incoherence, which is a measure of the void size. The end of turbulent fluidization (U_k) is determined to be 1.19 m/s

Table 3-1: U_c correlations and predictions of the system under investigation [46]

Authors	Equation	Predicted value (m/s)
Jin et al. [82]	$u_c = (gd_p)^{0.5} \left[\frac{(KD_f)(\rho_s - \rho_g)}{d_p \rho_g} \right]^{0.27}$ $KD_f = 0.00367 \text{ (for free bed)}$	0.66
Cai et al. [83]	$u_c = (gd_p)^{0.5} \left[\frac{0.211}{D_t^{0.27}} + \frac{2.42 \times 10^{-3}}{D_t^{1.27}} \right] \left[\frac{D_t(\rho_s - \rho_g)}{d_p \rho_g} \right]^{0.27}$	0.68
Nakajima et al. [84]	$Re_c = 0.633Ar^{0.467}$	0.79
Lee and Kim [85]	$Re_c = 0.7Ar^{0.485}$	0.95

3.2.2 Cross-sectional solids concentration

3.2.2.1 Mean solids concentration

Figure 3.6 shows the 5 min time-averaged mean of the cross-sectional solids fraction ($\bar{\phi}$) obtained from the X-ray data for the bottom plane. Makkawi and Wright found a 20 s measurement to be quite sufficient [75]. Three distinct types of behaviour are observed which coincide with the different regimes. A sharp decrease in $\bar{\phi}$ with velocity can be seen in the bubbling regime, with a more rapid decrease observed higher up in the reactor. Zhu et al. [53] observed similar height dependence using optical probes. The gradient of $\bar{\phi}$ changes for the turbulent regime; the same trend was seen by Makkawi and Wright [74] using ECT from a single height measurement. The solids concentration levels off and remains fairly constant with velocity at $H = 400$ mm and $H = 500$ mm. At the highest gas velocity in the turbulent fluidization regime, $\bar{\phi}$ -values at 200 mm, 300 mm and 400 mm are the same, while it is lower at 500 mm. The packed bed height was 500 mm; therefore the 500 mm measurement is close to the splash zone. The decreasing trend continues in the fast fluidization regime. In this regime there is no difference with height, except for measurements at 500 mm, which is at the

dense bed surface where one would expect a lower $\bar{\phi}$. Pneumatic transport is observed to set in at 2.60 m/s.

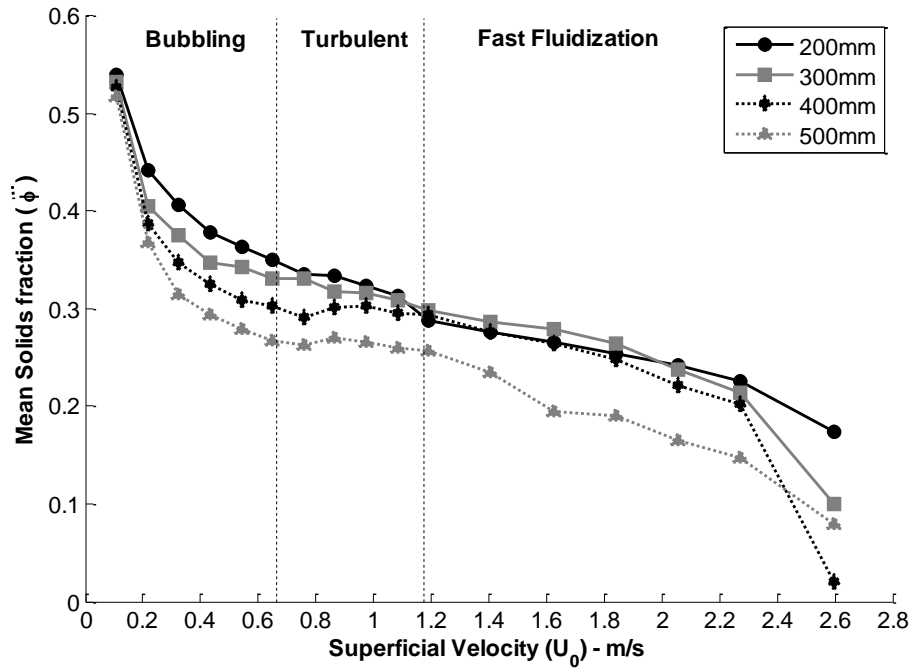


Figure 3.6: Average cross-sectional solids concentration with superficial velocity at $H=200$ mm, $H=300$ mm, $H=400$ mm and $H=500$ mm from the distributor

To get an impression of the radial solids distribution, the mean line solids fractions ($\bar{\phi}_i$) of each detector for a single source are indicated in [Figure 3.7](#). Only 2 min of data were used to calculate the mean of each line. The values of the outermost detectors are not shown. Due to the close proximity of the detection line to the wall, column vibrations influenced the outer detector value. Between 0.55 m/s and 0.83 m/s radial profiles are fairly constant, which suggests that, as with $\bar{\phi}$, the radial solids distribution remains constant as well. At the lowest superficial velocity asymmetry is observed; this is due to low distributor pressure drop causing mal-distribution. At high velocities the pressure drop across the distributor increases and better symmetry is observed. Slight deviation from symmetry is most likely caused by the solids return inlet coming from the cyclone system. Ellis et al. noted a similar effect due to the solids return [72].

At 200 mm smooth profile contours are obtained for all velocities. Axially higher up in the column a spike in the radial centre is seen, which disappears as the fast fluidization regime is reached. This cannot be attributed to mal-distribution since it is not observed at 200 mm. The

bubble wake geometry can provide a plausible explanation as the high solids density wake of the bubble appears frequently in the centre of the column, with a leaner ring structure surrounding the wake. This would explain the centre spike in solids density, which will disappear when the core-annulus structure of fast fluidization is formed. Bubbles were undeveloped lower down in the column which is why they are not seen at 200 mm. Higher up bubbles merged and grew, moving up in the centre of the column.

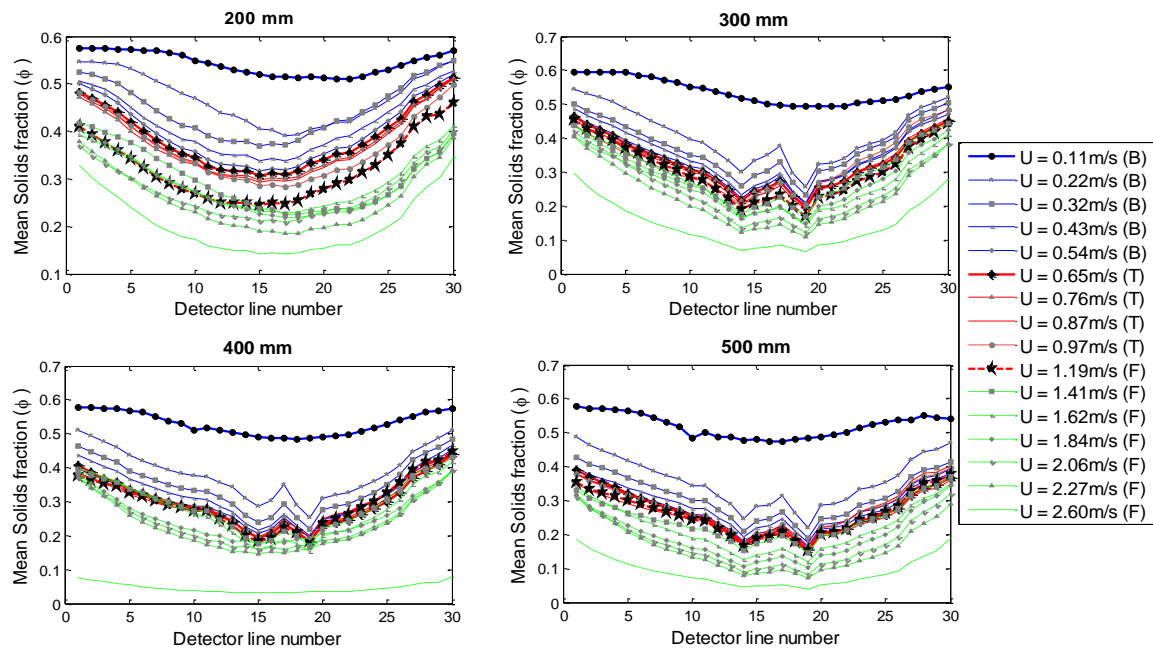


Figure 3.7: Mean line solids fraction indicating radial distribution of solids. Bold markers indicate U_c and U_k . Regime indication is given in the velocity legend

3.2.2.2 Solids concentration distributions

Figure 3.8 shows the density distributions of the ϕ signals at different velocities and heights. The distributions are based on 5 min of data. Unimodal and bimodal curves are observed. The bimodal curves indicate that two distinct phases exist. The peak at higher solids concentration would represent the emulsion phase, whereas the lower peak would represent the lean phase (bubbles and voids). The lean phase peak is less defined due to the presence of voids and emulsion over the cross-section. In the case of a unimodal trend, the signal does not fluctuate between the two phases. The conclusion can be drawn that the structure that exists in the bed remains fairly constant with time. The trend at 200 mm is considerably different from the trends higher up in the column, especially for the turbulent

regime. The distributions at 200 mm tend to be unimodal. It is unlikely that a core annulus exists at the low velocity. In this case the trend could be explained if multiple small bubbles pass frequently through the cross-sectional measurement plane.

The bubble regime has a clear bimodal trend, with large emulsion phase peaks. Since it is known that the fast fluidization regime is characterized by a constant core-annulus structure, a unimodal trend is expected and noted in the results. For the turbulent regime the mean cross-sectional solids concentration and radial solids concentration profiles ([Figure 3.6](#) and [Figure 3.7](#)) show constant values with velocity. However, the density distributions differ slightly with regard to velocity. The fact that emulsion phase peaks exist in the turbulent regime is also noteworthy. This observation indicates that there are times when the cross-section (higher up in the column) contains no voids. It should also be noted that the median of the emulsion phase peak does not change significantly with velocity.

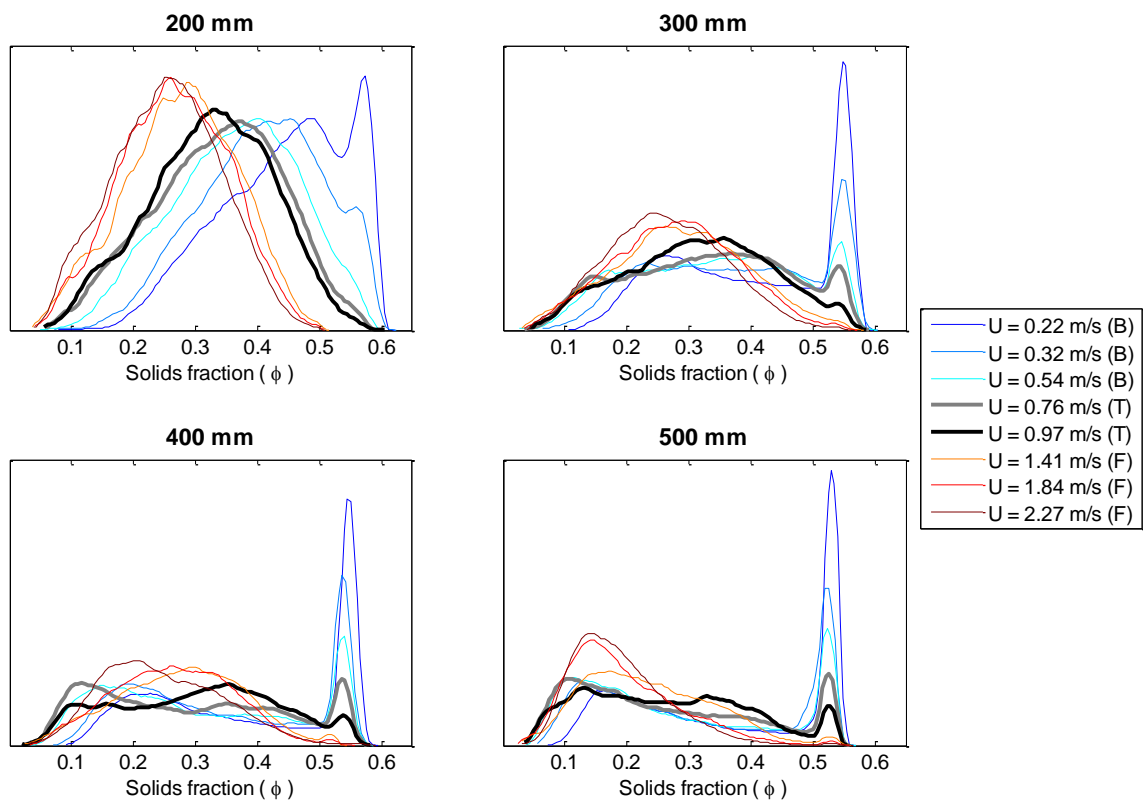


Figure 3.8: Density distributions of the cross-sectional solids concentration (ϕ) at different heights

3.2.2.3 Average void rise velocity (\bar{u}_v)

The average void rise velocity (\bar{u}_v), calculated using cross-sectional solids concentration data, is shown in [Figure 3.9](#). \bar{u}_v increases significantly in the bubbling regime with superficial velocity. As the superficial velocity increases into the turbulent regime, \bar{u}_v continues to increase. However, in the bottom part of the column (at 200 mm), the voids reach a constant velocity fairly quickly. This trend agrees with that observed in the standard deviation of incoherence in [Figure 3.3](#). The pressure probe was also in the bottom section of the column and both are a function of bubble size. Measurements higher up in the column all fall in a band where \bar{u}_v levels off but does not necessarily reach a constant value. Even though cross-sectional solids concentrations become independent of the superficial velocity in the turbulent regime, void dynamics does not. There was no clear trend for \bar{u}_v in the fast fluidization regime and it seemed to be random. These random values occur because no more distinct voids are rising; rather a core-annulus structure forms, which fluctuates causing random minimums in the SSDs.

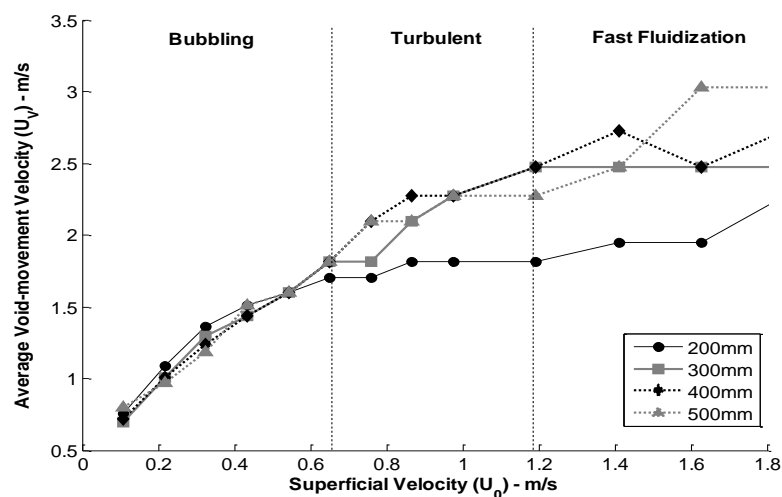


Figure 3.9: Average voids movement

3.2.3 Tomographic reconstruction

The data from the two measurement planes were processed using a Simultaneous Algebraic Reconstruction Technique (SART). This technique is an iterative reconstruction algorithm by which an instantaneous cross-sectional image of the bed is obtained. For more details on the reconstruction algorithm see previously published work on the technique [55,56,80]. [Figure 3.10](#) is an example of such a reconstructed image for both the bottom and

top planes at the same point in time. A cross-section of the bubble nose is seen in the top plane, whereas a cross-section of the same bubble lower down is seen in the bottom plane.

Signal noise, inherent to the X-ray sensors, was eliminated by averaging over 10 samples. 55 by 55 pixel images were reconstructed, resulting in a 2.54 mm pixel length. Pixels outside the column diameter were automatically assigned a zero value. Given the 2 500 Hz acquisition frequency, reconstruction resulted in 250 images per second. The images were stacked for both the top and bottom planes and a pseudo-3D representation of bubbles/voids could be obtained. The z-axis has time as scale and therefore the true length dimension of the bubble is not given. [Figure 3.11](#) shows the results of this entire process for 2 s of data, 300 mm above the distributor, and a superficial velocity of 0.11 m/s.

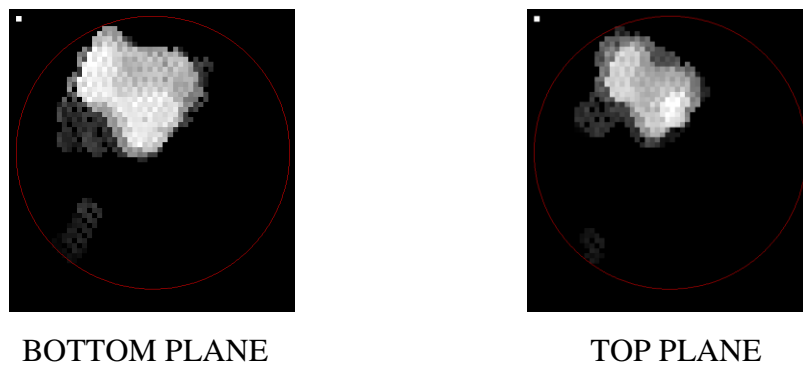


Figure 3.10: Reconstructed cross-sectional image for the bottom and top planes. Both images are taken at the same point in time. This example is taken from the measurement at a height of 300 mm and a superficial velocity of 0.11 m/s

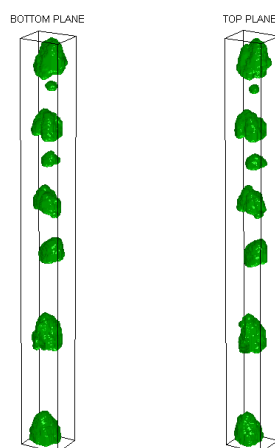


Figure 3.11: Pseudo-3D reconstruction of the void shapes over 2 s. $H = 300$ mm and $U_0 = 0.11$ m/s. The y-axis and x-axis give length dimensions, while the z-axis represents time. $t=0$ s at top and $t=2$ s at bottom

Figure 3.12 shows samples of the bottom and top plane reconstructions for the bubbling regime ($U_0 = 0.43$ m/s) and turbulent regime ($U_0 = 0.87$ m/s) at two different heights ($H = 200$ mm and $H = 400$ mm). Using the calculated average void rise velocity (\bar{u}_v), the z-axis was converted from a time to length scale. Very good agreement is seen between the two planes. Slugs were observed during experimental runs and the plug-like slugs are clearly visible at $U_0 = 0.43$ m/s, $H = 400$ mm. For the turbulent regime slug-like structures are seen, although visually these voids appear to have smaller cross-sections than slugs. The turbulent regime's flow structures are more closely represented by a train of highly elongated bubbles. This could be the start of a core annulus which collapses within moments.

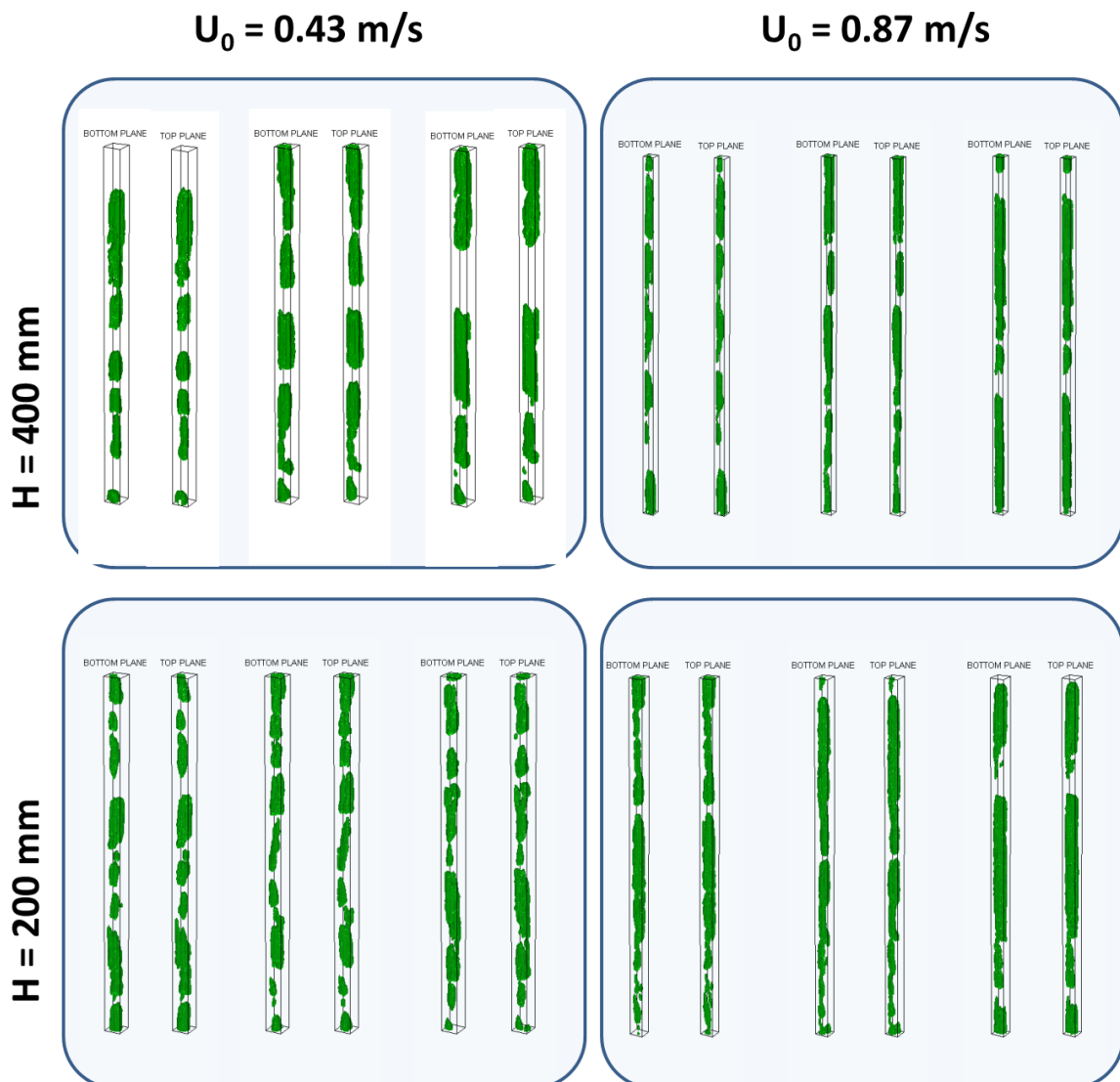


Figure 3.12: Samples of 2 s reconstructions at two superficial velocities (bubbling – $u_0 = 0.43$ m/s and turbulent – $u_0 = 0.87$ m/s) and heights ($H = 200$ mm and $H = 400$ mm)

The technique of Brouwer et al. [76] was used to determine volume-equivalent bubble diameters. The individual rise velocity of each bubble is required. Using the pseudo-3D images and an object-matching algorithm, bubbles are identified and matched between the bottom and top plane reconstructions. This matching is done on the basis of similar position in the x-y plane, similar volume of the pseudo-3D bubble and a maximum allowable bubble rise velocity. Once bubbles are matched, the time it takes for a bubble's centroid to rise from the bottom plane to the top plane is determined. Using this time and the fact that the planes are 10.9 mm apart, it is possible to determine the rise velocity and thereby the true volume of the bubble. Three parameters for every void passing the measurement plane can be determined:

- Void volume – V_b
- Void length (distance from bubble nose to wake) – L_b
- Void velocity – U_{b-Tomo}

Due to the computational intensiveness of the analysis procedure, the shortest significant signal lengths were employed. Initial signal periods of 2.5 s were taken and doubled until the mean bubble volume-equivalent diameter (d_b) changed by less than 5%. A minimum of 10 s of data was required before d_b remained unchanged for the low-velocity measurements. [Table 3-2](#) shows the signal length required for the analysis of each experiment and the number of void objects that could be matched. The bubbling and turbulent regimes are analyzed, and the fast fluidization regime is characterized by a core-annulus structure which cannot be quantified in this manner. [Figure 3.13](#) shows the percentage of objects that could be matched. More than 50% of voids could be matched in the bubbling regime; however, the chaotic nature of the turbulent regime is evident. It is unclear whether this is due to limitations of the XRT reconstruction or matching algorithm. Care should therefore be taken not to draw quantitative conclusions for the higher velocity turbulent runs.

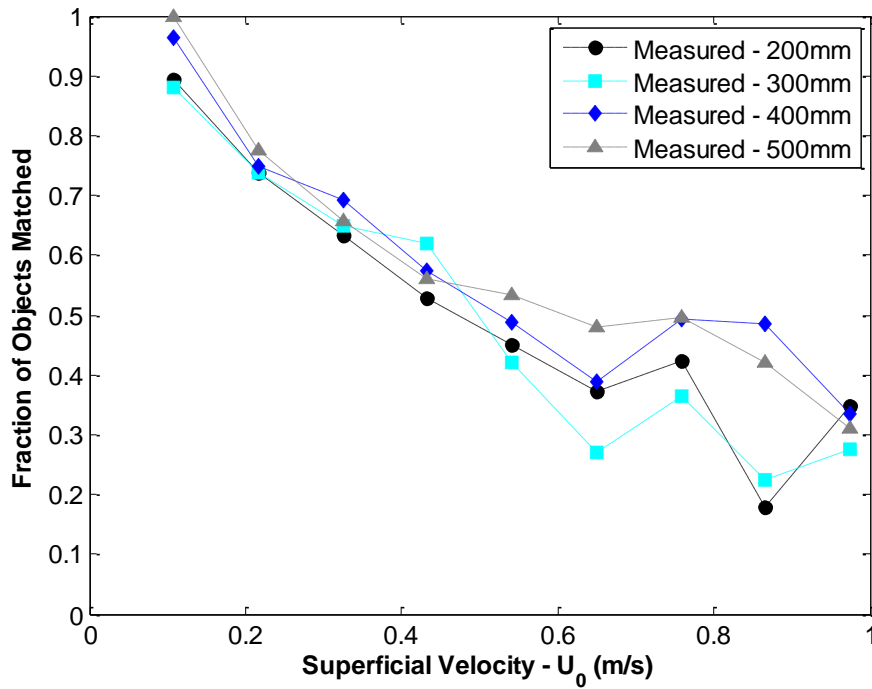


Figure 3.13: Fraction of void objects that could be matched in both bottom and top planes

Table 3-2: Signal lengths analysed to determine mean bubble diameter

Flow (m/s)	Signal length analysed in seconds			
	(Number of voids detected indicated in brackets)			
	200 mm	300 mm	400 mm	500 mm
0.11	10 (72)	10 (40)	10 (26)	10 (26)
0.22	10 (38)	10 (28)	20 (37)	20 (31)
0.32	20 (56)	20 (47)	20 (37)	20 (27)
0.43	20 (43)	20 (39)	20 (33)	20 (25)
0.54	20 (32)	20 (23)	20 (29)	20 (28)
0.65	20 (21)	40 (15)	40 (42)	40 (52)
0.76	40 (38)	40 (42)	40 (52)	40 (56)
0.87	40 (13)	40 (18)	40 (45)	40 (49)
0.97	40 (24)	40 (21)	40 (26)	40 (33)

3.2.3.1 Sphere equivalent bubble diameter

The first plot of [Figure 3.14](#) shows the resulting mean sphere-equivalent bubble diameter (d_b). This parameter is the diameter of a perfect spherical bubble with the same volume as the void. Karimipour and Pugsley evaluated 25 bubble correlations with 20 sets of bubble size data obtained from the literature [86]. For Geldart B particles they recommend the correlation of Choi et al. [87]:

$$(U_0 - U_{mf})(d_b - d_{b0}) + 0.474g^{0.5}(d_b^{1.5} - d_{b0}^{1.5}) = 1.132(U_0 - U_{mf})H \quad 3-3$$

with

$$d_{b0} = 0.00376(U_0 - U_{mf})^2 \quad 3-4$$

In [Figure 3.14](#) the correlated bubble size based on this recommendation is shown. The correlation performed very well at low superficial velocities and reasonably well for the 200 mm measurements.

Typical Geldart B behaviour is observed; bubble growth is seen to occur with column height as well as superficial velocity. Slugging was visually observed during the experiments and would explain the deviation from the correlation. Slugging is defined as when the bubble diameter is 66% that of the column [42]. For this column that would be approximately 0.1 m. d_b can go beyond 0.14 cm since the volumes of the voids, which could be cylindrical slugs, are converted to a spherical equivalent.

With the height and volume of each void known, the mean cross-sectional void area is determined as a fraction of the total cross-sectional area. The second plot in [Figure 3.14](#) shows this parameter; it increases up to a point and reaches a plateau. Further “bubble growth”, or rather volume increase, occurs in the height dimension of the voids. Slugging starts higher up in the column from a superficial velocity of 0.2 m/s. At $U_0 > 0.45$ m/s the entire bed is slugging. The plateau value is below 0.4, meaning that solids are still moving down the sides of the slugs.

Bubble behaviour becomes more erratic in the turbulent regime and a clear trend with height cannot be observed. The cross-sectional area fraction decreases in the turbulent regime, yet the spherical diameter shows that the bubble volume does not decrease, except at 500 mm. This could hint that the voids are thinner, elongated shapes.

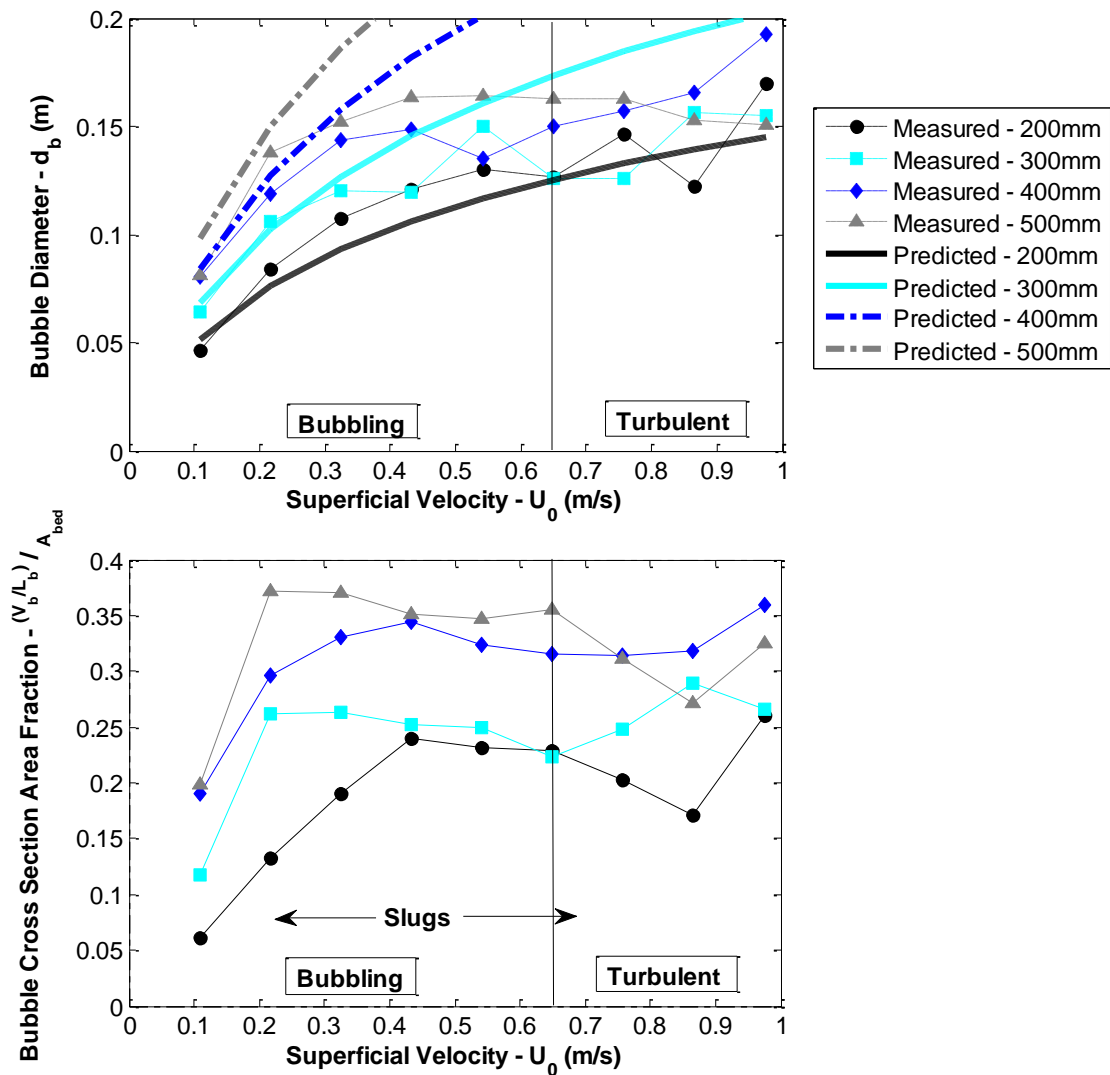


Figure 3.14: Comparison of bubble size correlations with the measured bubble diameters (d_b) for the regime from bubbling up to turbulent

3.2.3.2 Void structure and velocity analysis

This final discussion will be based on overall bed averages, i.e. the average values between the different measuring heights. From the discussion thus far it is evident that hydrodynamic behaviour is not fully developed at 200 mm. The data from this measurement height will therefore be excluded from the averages. [Figure 3.15](#) shows the measured void parameters: void volume (a), void length (b) and the cylindrical diameter (c) if the assumption is made that voids are cylindrical shapes. [Figure 3.15d](#) confirms that this assumption is a reasonable one as it shows that the void volume is directly proportional to the void length. Theory suggests that U_c is the point at which the largest stable bubbles exist;

beyond U_c bubbles break up into smaller transient voids [88]. A decrease in void volume, as well as length, is seen to occur at U_c , after which both continue to increase. However, the cylindrical diameter continues to decrease, confirming that the structures are thinner, elongated bubbles. In the Zhang and Bi optical probe study of void behaviour [52] it was found that void lengths decrease in the turbulent regime. Their investigation was, however, done on Geldart A particles (see Section [2.2.2](#)).

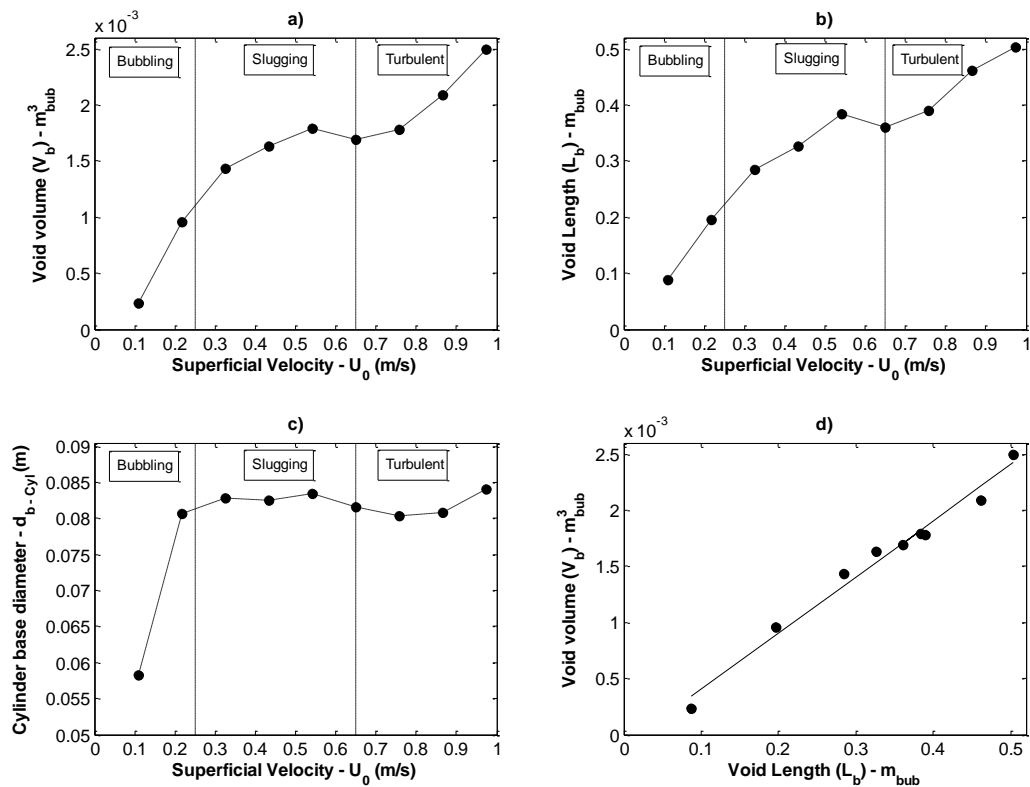


Figure 3.15: Quantification of void structures

Two seconds of reconstructed fast fluidization regime pseudo-3D images are shown in [Figure 3.16](#) ($U_0 = 1.84$ m/s). Since the core annulus is a continuous structure the z-axis cannot be scaled using a velocity as was done for [Figure 3.12](#). It was found from the reconstructions that the diameter of the core annulus increases with height and is in the range of 9 cm to 11 cm.

The expanded bed height in the turbulent regime is approximately 1 m and the void lengths are 0.4 m to 0.5 m, with cross-sectional diameters of approximately 8 cm. Even though the turbulent regime exhibits unique hydrodynamic behaviour, the structure of the voids seems to be a transient state between the flow structures of the bubbling and fast

fluidization regimes. The structure in the turbulent regime is best described as an unstable core annulus or as thin, elongated bubbles. This structure is most likely caused by the column diameter limitation and might not apply in columns of larger diameter.

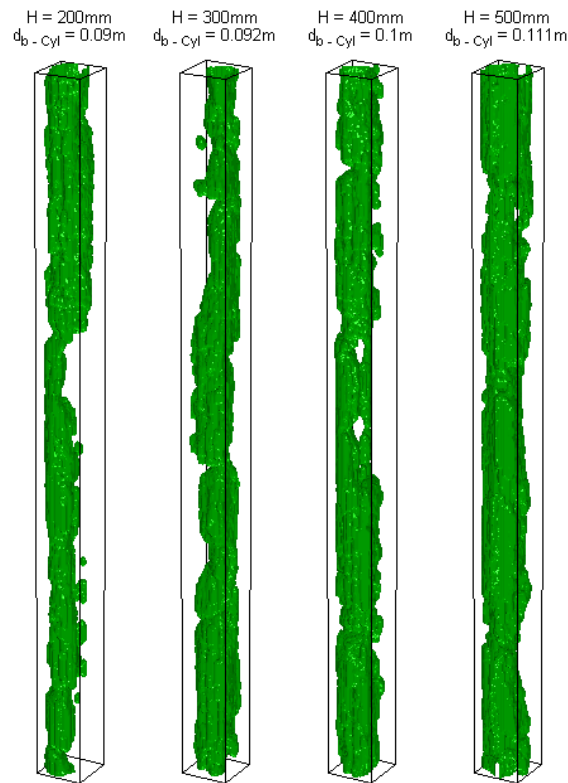


Figure 3.16: Illustration of the core annulus at different heights in the column. $U_0 = 1.84 \text{ m/s}$

There are three methods of determining the void rise velocity, two of which have been discussed, \bar{u}_v and $U_{b\text{-Tomo}}$. The third method is theoretically based on a mass balance and the mean solids concentration, $U_{b\text{-Theo}}$:

$$\psi_B = \frac{U_0 - U_{mf}}{U_b - U_{mf}} \quad \text{for } U_0 \gg U_{mf} \rightarrow \psi_B \approx \frac{U_0}{U_b} \quad 2-6$$

where ψ_B is calculated using the cross-sectional solids concentration:

$$\psi_B = \frac{\Phi_{mf} - \Phi_0}{\Phi_{mf}} \quad 2-5$$

Figure 3.17 shows how the average rise velocity changes with the superficial velocity. Also indicated is the standard deviation of $U_{b\text{-Tomo}}$. Trend-wise, \bar{u}_v and $U_{b\text{-Theo}}$ agree well, but the absolute values are different. This difference can be due to tolerance variation in the

measurement of the distance between the two planes. $U_{b\text{-Tomo}}$ has a large standard deviation at higher superficial velocities. It is based on individual bubble measurements and such deviations are to be expected. An important observation is that the average $U_{b\text{-Tomo}}$ is much lower than \bar{u}_v . As shown by [Figure 3.13](#), a large number of detected objects could not be matched in both planes. From [Figure 3.17](#) it would appear that the algorithm fails to match the relatively fast voids. The detection boundary for $U_{b\text{-Tomo}}$ is limited by the temporal resolution of the setup. With an approximate plane distance of 10.9 mm and a sampling rate of 250 Hz, the maximum detectable void rise velocity is 2.725 m/s. It is not clear from the graph, but it needs to be kept in mind that the standard deviation includes only 68% of the data. The total distribution of data is cut off at 2.7 m/s. Quantitative measurements relying on this algorithm should not be used for the turbulent regime. \bar{u}_v is recommended for further discussion.

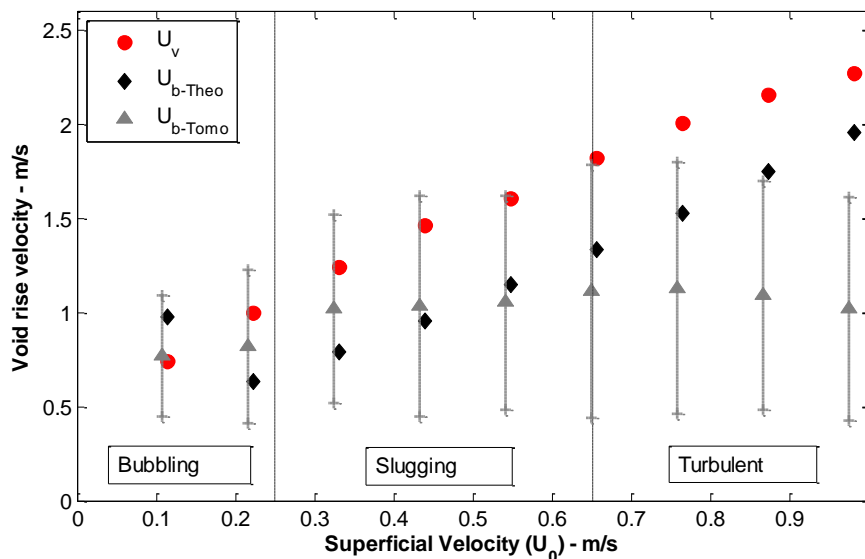


Figure 3.17: Comparison of different methods for determining the average rise velocity of voids

3.3 Conclusions

It was possible to measure the solids fraction effectively and to conduct tomographic reconstruction for higher superficial velocities using a fast XRT setup. Distinct behaviour was observed for all the fluidization regimes. Determination and characterization of the regimes can be done using pressure measurements, solids-fraction measurements and reconstructed tomography images.

The mean cross-sectional solids concentration visibly decreased with velocity and axial height, but remained fairly constant with velocity in the turbulent regime. The shape of the radial profiles also remained constant with velocity in the turbulent regime. Probability density distributions show that there were still two phases present in the turbulent regime and that the emulsion-phase solids concentration remains independent of velocity until fast fluidization sets in. It was observed that the bed structure was not yet fully developed at 200 mm above the distributor.

Bubble size measurements could be obtained for the bubbling, slugging and turbulent regimes. Good agreement between correlations and measured bubble sizes were found in the bubbling regime. The system exhibited slugging behaviour due to particle classification and column size. The point at which the slugging regime starts could be quantified using the reconstructed voids and it was proved that the voids could be characterized as cylindrical in shape. Erratic void behaviour was seen in the turbulent regime; nevertheless, the same cylindrical structures existed and were narrower than for the slugging regime. It was shown that the turbulent regime has unique hydrodynamic behaviour, although the structure of the voids appears to be a transient state between the void structures of the bubbling and fast fluidization regimes.

Three methods were used to determine void rise velocities. The first was a technique based on time-shift minimization of 5 min solids concentration signals, the second was based on theoretical equations, and the third on individual rising voids. Good agreement was obtained between the first two methods. The third method agreed well only for the lower velocities and it was concluded that the bubble-linking algorithm failed to link fast-rising voids. Overall, the abilities of the XRT setup were shown to be sufficient for the high-velocity regimes.

Chapter 4 : Linking Reactor Performance and Hydrodynamics

Advanced insight into the hydrodynamics of the Geldart B baseline sand particles has been gained in [Chapter 3](#). The investigation is now extended to the reaction column equipment using ozone, pressure probes and an optical probe. The same sand particles used in the tomography investigation (Chapter 3) are employed in this section. The reactor performance and hydrodynamics are measured simultaneously using the ozone decomposition reaction, pressure analysis techniques and intrusive solids concentration measurements. The bubbling regime up to the onset of the turbulent regime is investigated ($0.09 < U_0/U_c < 1.11$); this limited velocity span is due to the flow and pressure limitations of the reactor setup.

The hydrodynamic information obtained using the XRT setup ([Chapter 3](#)) was far more advanced and thorough than that of this reactor setup. Hence, the hydrodynamic measurements made in the reactor setup are compared with those of [Chapter 3](#) and using [Chapter 3](#)'s data an attempt is made to understand and correlate the hydrodynamic effects with the reactor performance. Lastly, known interphase mass transfer correlations are evaluated.

4.1 Experimental

4.1.1 Setup

All reaction investigations were conducted using a 14 cm (ID) acrylic column with a height of 5.5 m. The reaction implemented was the ozone decomposition reaction. Two cyclones in series were used to return entrained solids to the bed. The primary cyclone was a volute cyclone in order to handle high solids loading and the secondary cyclone was a tangential cyclone. An exhaust system with a solids filter bag container was installed after the cyclones to remove any remaining solids safely and to dispose of ozone-containing air via a stack. The filter bags were weighed before and after experiments and solids losses were found to be negligible. A triangular-pitch perforated plate distributor with thirty 2 mm holes was used. The open area of the distributor was 0.61%. A porous cloth was placed below the

distributor to prevent solids weepage. The cloth increased the pressure drop, which improved gas distribution.

Vortex flow meters with a superficial velocity range of 0.06 m/s to 1.2 m/s were installed. A rotameter was employed for velocities below this range. Differential pressure meters were installed across the bed and cyclones. These could be used to obtain u_{mf} and to ensure optimal operation of the cyclones. Absolute pressure transmitters were installed at the distributor, 0.2 m from the distributor and at 0.4 m for bubble measurements and u_c determination. The voidage probe was inserted at a height of 0.2 m from the distributor. [Figure 4.1](#) schematically shows the equipment setup.

The fluidizing medium was air supplied by a compressor, with a chiller maintaining the air at a constant temperature of 15 °C. The air was dosed with ozone generated by an EcoTec MZV1000 cold corona ozone generator. To ensure that no NO_x gases formed, oxygen was used as feed gas to the generator. Proper gas mixing was obtained using a freely rotating turbine rotor after the dosing point. The plenum chamber was also filled with 6 mm diameter glass beads. A gas sampling tube, for determining the inlet ozone concentrations, was inserted from the side to the centre of the plenum chamber, 50 mm below the distributor. Outlet samples were drawn from the centre of the reactor, 4.2 m above the distributor. The ozone-sampling probes were covered with filter paper to prevent solids from entering the sampling tubes and analyzer. The samples were continuously analyzed online using a 2B Technology Inc. UV-106 ozone analyzer, which employs the well-established method of light adsorption at a wavelength of 254 nm. All data were logged using 4–20 mA or 0–10 V signals in conjunction with National Instruments' USB-6008 DAQ devices connected to a PC. Flow measurements and ozone concentrations were logged at 10 Hz and the pressure-probe and voidage-probe measurements were collected at 1 000 Hz.

To determine catalyst activity, a small test reactor with plug flow behaviour, 16.4 mm in diameter, was installed. Both the Fluidized Bed Reactor (FBR) and the test reactor were supplied with the same ozone-dosed air. The test reactor could be loaded by tapping catalyst into it directly from the fluidized bed, thereby not exposing the sample to an atmosphere other than that inside the FBR. The test reactor was designed to detach safely from the FBR, to weigh and empty the loaded catalyst sample.



Fluidizing Air
feed line
(Ozone dosed)

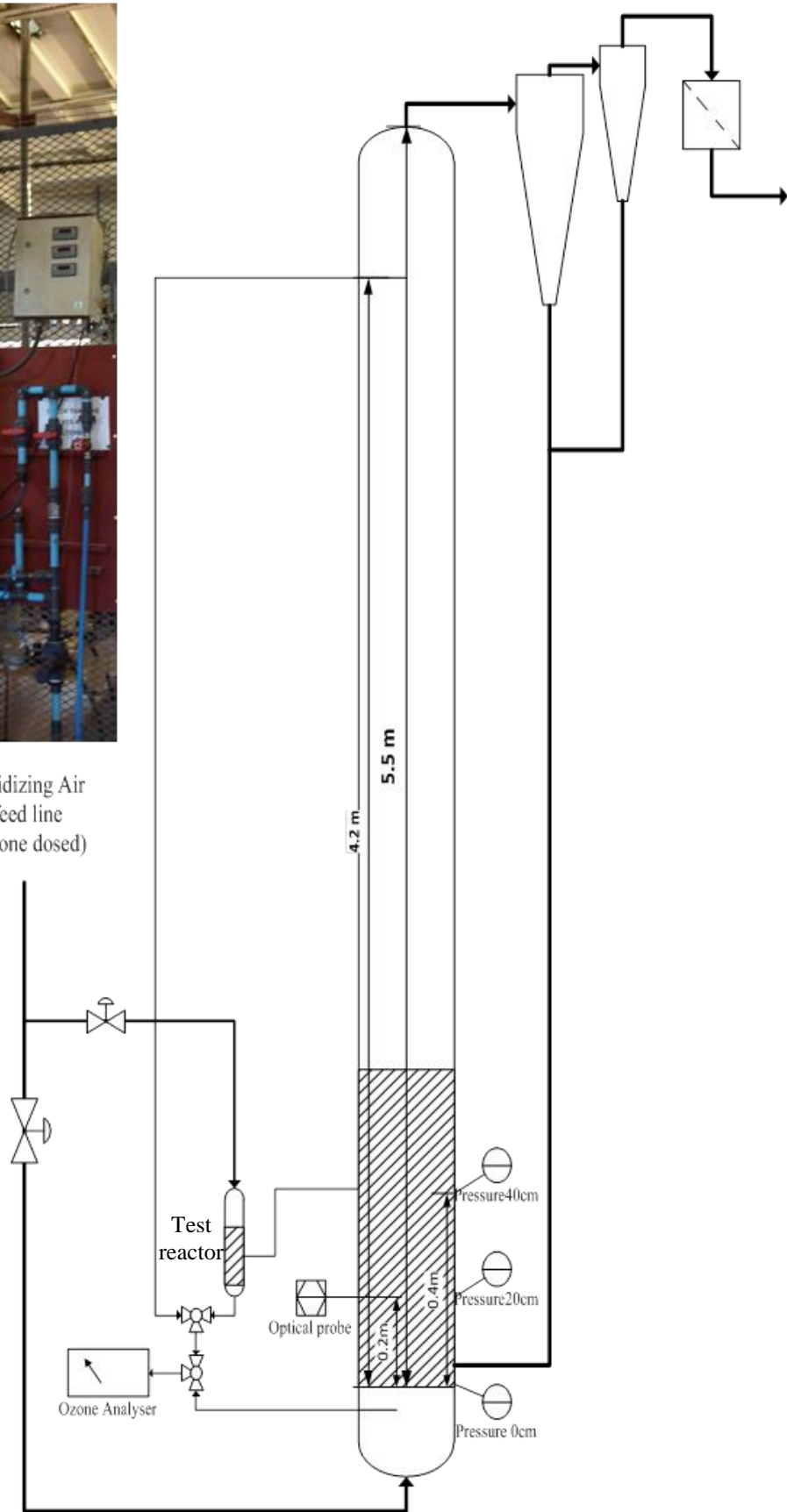
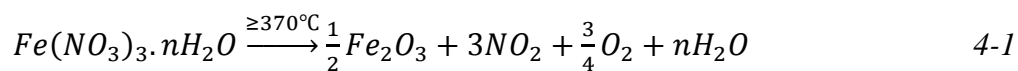


Figure 4.1: Reactor experimental setup and schematic drawing

4.1.2 Ozone decomposition catalyst

To activate sand for ozone decomposition, the particles require treatment. Iron oxide is consequently impregnated onto the particles. The method of Fan et al. was adopted [70,71]. The particles are mixed into a stirring solution of 10 wt.% ferric nitrate. After 1 h the stirrer is switched off and the solids are allowed to settle out for 15 min. Excess solution is decanted and the sludge placed in an oven for 12 h, resulting in dried solid chunks. These chunks are ground and sieved to the correct size fraction. Lastly, the batch is placed in a furnace at 475 °C to calcinate the impregnated ferric nitrate to ferric oxide. The calcination reaction is as follows:



As shown, NO₂ gas is released during the calcination process. When no NO₂ is detected, the reaction has reached completion; this takes approximately 2.5 h.

4.1.3 Method

Before experiments were started, first-order behaviour was confirmed using the small test reactor. Catalyst was loaded into the test reactor and the conversion determined at different flow rates and inlet ozone concentrations. These measurements were made in a relatively short period. A first-order reaction rate PFR model predicted these conversion results accurately, as shown in [Figure 4.2](#).

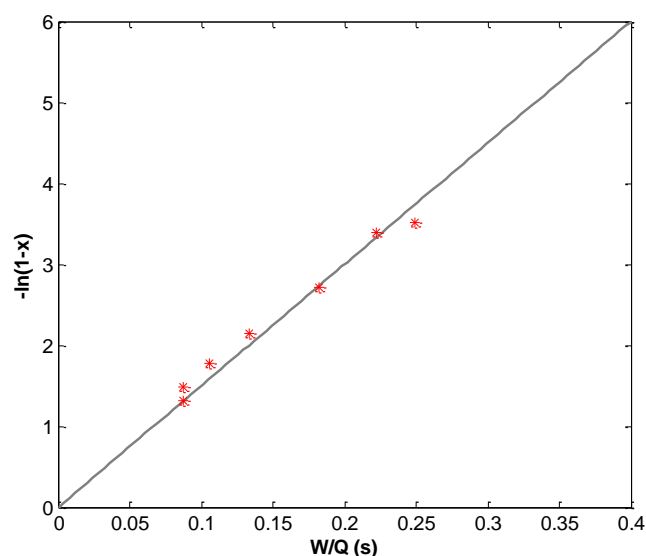


Figure 4.2: Confirmation of first-order behaviour. The linear line is a first-order PFR model with $k_r = 15 \text{ s}^{-1}$

A sample of the bed was taken and the catalytic activity was determined for each measurement of the FBR's conversion. In this way variations in the bed activity are accounted for. This solves the problems of catalyst instability discussed in Section [2.2.4](#). Instead of trying to stabilize the activity, it is continuously monitored. During experiments the test reactor was used to check the activity of the catalyst inside the FBR. This was achieved by running the FBR and test reactor in parallel. Care was taken to sample catalyst out of the FBR into the test reactor without exposing the sample to a different atmosphere. Both reactors were supplied with the same feed gas and advantage was taken of the liquid nature of fluidization to "tap" catalyst directly into the test reactor. During operations the test reactor was run at a single velocity since first-order behaviour was known. After each FBR conversion reading, a catalyst sample was taken and the activity determined within 5 min. In this manner a pseudo-instantaneous catalyst activity was obtained. The detachable design of the test reactor made catalyst unloading and weighing between measurements possible.

The following procedure was completed to determine the reactor's conversion. The FBR was set to a specific superficial velocity. The outlet gas-sampling probe was operated in reverse to backwash the filter. High-pressure air from the plenum chamber was used. After the filter had been cleaned, the FBR's outlet concentration was measured for 90 s. Sampling was then switched to the plenum chamber to determine the inlet concentration for 90 s. Lastly, a fresh catalyst sample was loaded into the test reactor and the reaction rate constant determined within 5 min. In a single experimental run this procedure was repeated at 11 different superficial velocities. Three experimental runs were conducted and different means of velocity sequences were used for each run: low to high; high to low and a random selection.

Sand of mass 13.5 kg was loaded into the FBR. It was determined that 13.5 wt.% of catalyst was in the return system. For the range of superficial gas velocities studied, the settled bed height fluctuated by 0.9%, which was deemed negligible. The amount of catalyst in the return system therefore remained fairly constant. System properties are reported in [Table 4-1](#). Due to the impregnation process the particle density decreased from 2 530 kg/m³ to 2 450 kg/m³. The Sauter mean particle diameter remained the same since the impregnated particles were sieved using the same set of sieves to prepare the support particles (see Section [3.1](#)).

Table 4-1: Catalyst and fluidizing medium properties

	Sand (baseline)
ρ_p (kg/m ³)	2 450
ρ_b (kg/m ³)	1 450
\bar{d}_p (μ m)	101
Geldart	B
u_{mf} (mm/s)	9.1
\mathcal{E}_{mf}	0.41
μ_g (Pa.s)	18×10^{-6}
ρ_g (kg/m ³)	1.2
D_m (m ² /s)	20×10^{-6}

An optical probe was used to measure the solids concentration. To calibrate the measured signal with the concentration of solids, a two-point calibration is used. The first point is determined by placing the tip in unfluidized powder; this is the signal reading for Φ_{packed} . The second point is determined by placing the tip in a sufficiently long, dark, solids-free tube; this is the signal reading for a solids concentration of zero. A linear calibration is assumed between these two points. It will be shown that this assumption is reasonable and compares relatively well with the tomography data.

The non-intrusive technique of Van der Schaaf et al. [49] was used (Section 2.2.1) for monitoring bubble behaviour. This is the same pressure analysis method used in the tomography investigation where two pressure probes are required. One probe is at the distributor and the second at a height in the bed where bubble measurement is desired. The Power Spectral Densities (PSDs) of both pressure probe signals are compared and the incoherence of the two signals relative to each other is calculated. The standard deviation of this incoherence (σ_i) is a measure of the average bubble/void size.

4.2 Results and discussion

Voidage probe data, absolute pressure readings, overall reactor conversion and pseudo-instantaneous catalyst activity (first-order rate constant) were logged. [Appendix C](#) contains the conversion and catalyst activity data. Using pressure fluctuations at 0.2 m above the distributor, the transition from bubbling to turbulent regime was measured and verified to remain at 0.65 m/s.

4.2.1 Reactor performance quantification

Initial work to quantify reactor performance was done using an FCC catalyst in a pseudo-2D column [58,62]. In previous work, the Thompson et al. (1999) model was used to do a best fit of the reactor performance over the velocity range and ascertain the mass transfer and axial dispersion using the fitted parameters. As shown by both Brink et al. [62] and Saayman [58], the shape of the fitted curve is dependent on the catalyst activity; therefore, if the activity changes significantly and the reactor is not fully mass transfer controlled, the method fails. Catalyst activity for sand is shown in [Figure 4.3](#). Large changes and fluctuations in the activity are seen. These are caused by catalyst deactivation and humidity fluctuations respectively. The humidity of the fluidizing air oscillated (1.5 h cycles), creating further activity fluctuations. This behaviour was caused by the compressor's chiller/dehumidifier.

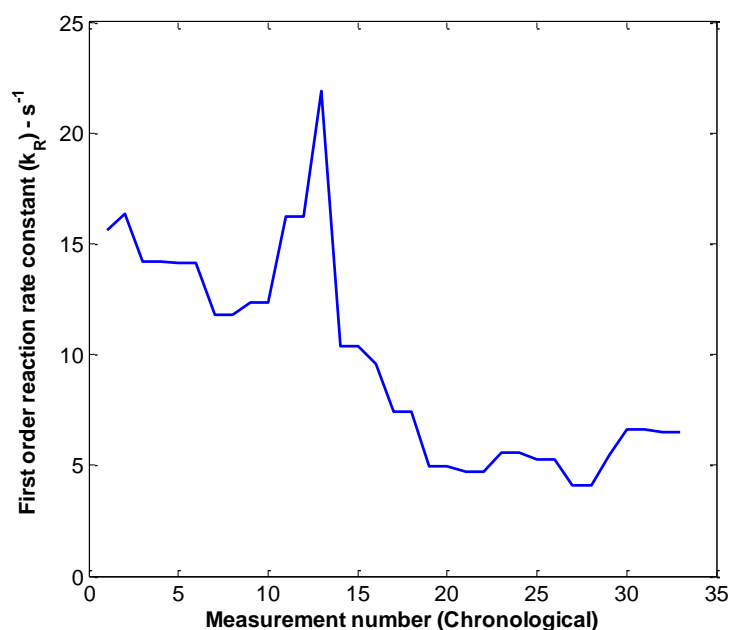


Figure 4.3: First-order rate constant as experiments were conducted

An alternative method of interpretation had to be used where data points could be evaluated individually. For this work the technique was refined and a different reactor modelling approach was implemented. The best solution entailed fitting the basic two-phase model (Section 2.4.1) to experimental data using the overall mass transfer coefficient (K_0) as fitting parameter:

$$C_i = u_B C_{i,B} + u_E C_{i,E} \quad 2-9$$

$$A_{bed} u_B \frac{dC_{i,B}}{dW_v} = -K_0 (C_{i,B} - C_{i,E}) \quad 2-10$$

$$A_{bed} u_E \frac{dC_{i,E}}{dW_v} = -R_i(C_E) + K_0 (C_{i,B} - C_{i,E}) \quad 2-11$$

The advantage of this approach is that only one parameter is fitted and all complexities of the Thompson et al. (1999) model are avoided. It is important to understand when fitting this model to experimental data that K_0 will be an apparent parameter, similar to an apparent reaction rate constant. The value of K_0 will be influenced by hydrodynamic behaviour, which is not considered in the model; hence it is referred to as an “apparent overall mass transfer coefficient”. Due to K_0 's incorporation of hydrodynamic effects, it serves as a good indicator of the reactor's performance, irrespective of the catalytic activity.

By taking into account the hydrodynamics of the reactor, the K_0 parameter can be converted to the generally used area-specific mass transfer coefficient (k_{be}). K_0 should be multiplied by the solids concentrations and divided by the specific bubble area:

$$k_{be} = \frac{K_0 \Phi_0}{\psi_B a_i} \quad 4-2$$

where

$$\Phi_0 = (1 - \varepsilon_0) \quad 4-3$$

$$\psi_B = \frac{\Phi_{mf} - \Phi_0}{\Phi_{mf}} \quad 2-5$$

or

$$\psi_B = \frac{U_0 - U_{mf}}{U_b - U_{mf}} \quad \text{for } U_0 \gg U_{mf} \rightarrow \psi_B \approx \frac{U_0}{U_b} \quad 2-6$$

It needs to be kept in mind that three hydrodynamic elements are assumed to have negligible influence on conversion when using the basic two-phase model:

- Solids content in the total disengagement height (TDH)
- Solids content in the bubbles
- Gas flow in the emulsion phase is at u_{mf} .

The effects of these elements will be incorporated into K_0 and could bias the k_{be} value if they are not negligible. Attempts at examining the validity of each assumption are made during the analysis of data in this chapter as well as in the following chapter.

The first assumption with regard to the TDH was addressed by measuring the reactor outlet solids concentration/entrainment (see [Appendix B, Figure B.5](#)). Even with an ideal PFR assumption and the freeboard model of Kunii and Levenspiel [89], the contribution to overall conversion is between 5% and 10% of the conversion value. This is at the highest flow rate (0.7 m/s) and is even less at lower flow rates. The TDH assumption was therefore deemed acceptable, especially when considering the bubbling regime to the onset of the turbulent regime.

The second assumption of bubble solids content is addressed in Section [4.2.2](#) and the third assumption of emulsion phase flow is discussed in Section [5.3.5](#).

4.2.2 Overall reactor performance (K_0)

Using the basic two-phase model, reactor conversion and catalyst activity at a superficial velocity, the apparent overall mass transfer coefficient (K_0) could be determined. Due to the implicit nature of the model, K_0 was fitted until the model conversion and the actual conversion matched within $\pm 1\%$. [Figure 4.4](#) shows the reactor performance (K_0); the average of the three measurements at a superficial velocity was calculated. Reactor performance increased up to a superficial velocity of 0.45 m/s, after which a decreasing trend was observed. This behaviour cannot be explained by the observed slugging, as slugging started around 0.2 m/s. All the hydrodynamic parameters need to be considered and incorporated.

The assumption of negligible bubble solids content can be explored using the observed result. Work by Sun and Grace [63] showed that bubble solids content increased with velocity. If the increased solids content was not negligible and significantly influenced K_0 , then the decreasing trend beyond 0.45 m/s would not be evident. From the measured parameters the bubble's solids content could not be determined directly. However, these results show indirectly that the assumption is acceptable and the possible contribution of solids in the bubble is of a secondary nature.

For later comparisons between the reaction measurements and the XRT measurements, a fit is required. Each investigation was performed at different superficial velocities and interpolation of reactor performance was required. A fourth-order polynomial was used, as

fourth order accurately preserves the shape. Excessive extrapolation outside the velocity range of 0.06 m/s to 0.705 m/s is not recommended.

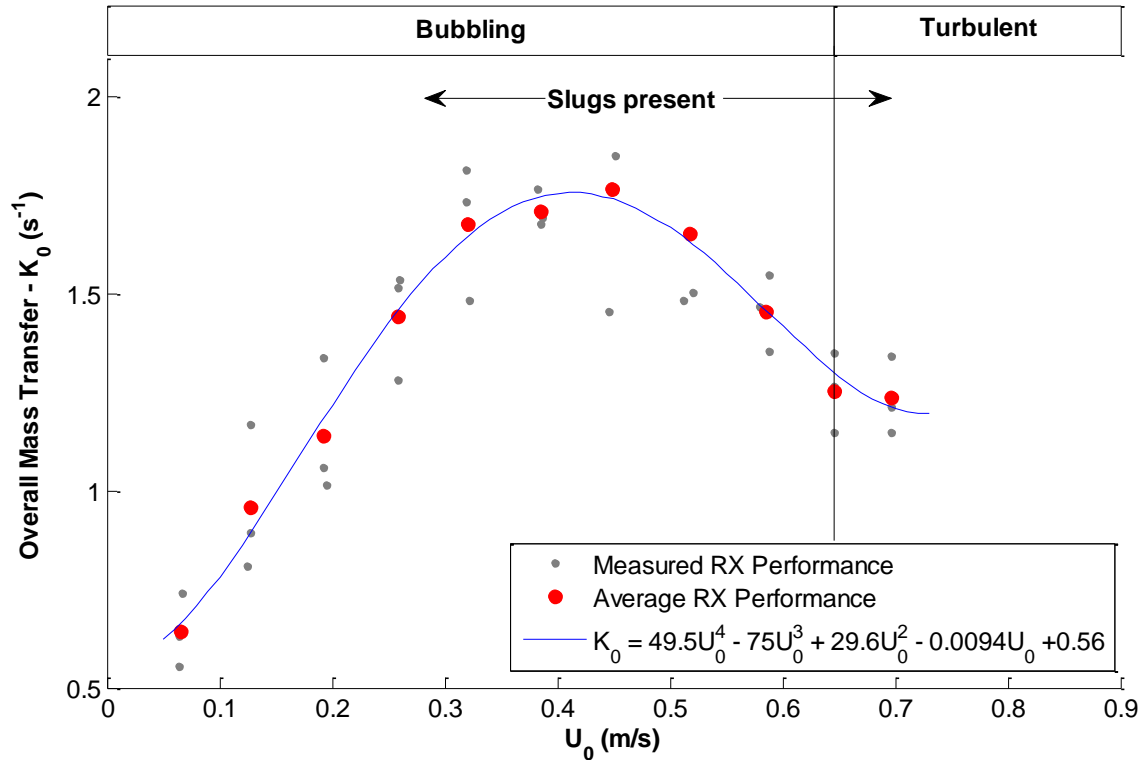


Figure 4.4: Reactor performance and fitted polynomial for interpolation

4.2.3 Hydrodynamic measurements

All the hydrodynamic parameters were well studied in [Chapter 3](#). However, it was desirable to investigate the reliability of the hydrodynamic measurement capabilities of the reaction setup. This knowledge would be useful for further reactor performance studies (discussed in [Chapter 5](#)) where particle systems were implemented in the reactor setup for which XRT data were not available. [Figure 4.5](#) shows the agreement that exists between the method of standard deviation of incoherence and measured void length at 200 mm above the distributor.

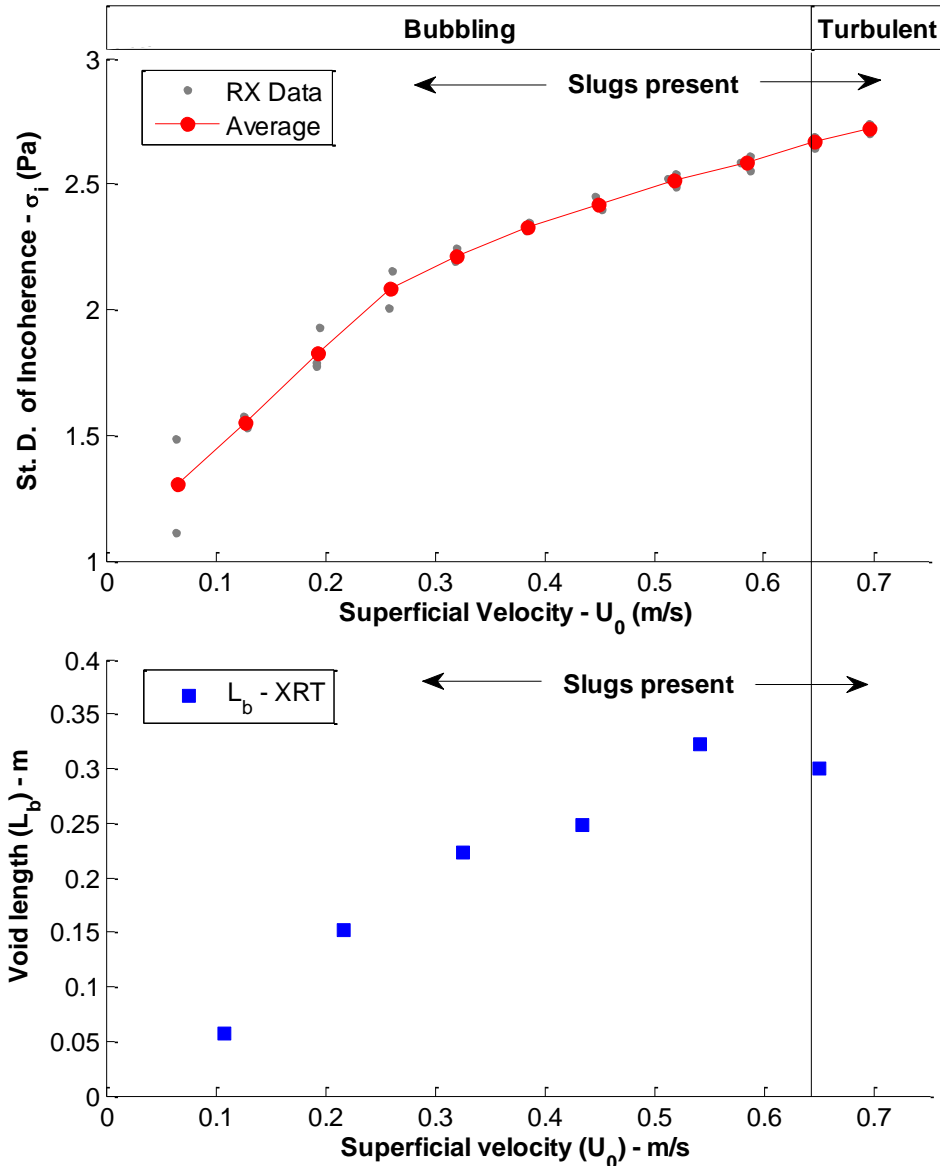


Figure 4.5: Agreement between measured standard deviation of incoherence and the bubble size, determined via XRT

Figure 4.6 shows the mean solids fraction measured by the probe, as well as the XRT measurement at 200 mm above the distributor. The key difference between the two methods is that the probe is intrusive and measures at a single point, whereas XRT provides a non-intrusive total cross-sectional measurement. At first glance, good agreement is observed, although a few points should be noted. The probe tip was at the centre of the reactor and from the radial profiles of Figure 3.7 it is known that the solids concentration is lower at the centre of the reactor. Even though this difference in the solids fraction would only be around 0.05, it is seen that the probe results lie slightly above the XRT results, except at the very low velocity of 0.06 m/s. The intrusive nature of the probe technique could be the cause of this

observation. It is reasonable to assume that some particles become stuck on the window of the probe tip, since the probe is in direct contact with the solids. A higher concentration of solids would then be detected. Considering all of this, the probe measurements are still acceptable and the linear calibration can be justified (Section 4.1.3).

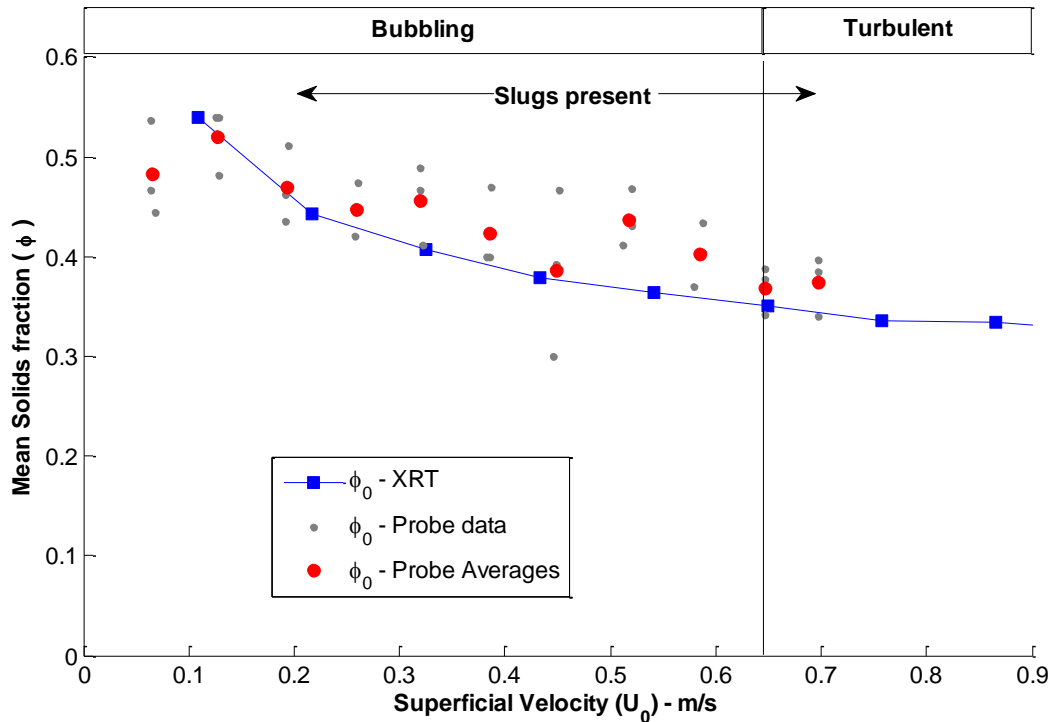


Figure 4.6: Comparison of measured solids concentration at $H = 200$ mm between the optical probe and XRT

4.2.4 Linking reactor performance and XRT measurements

Insight into the reactor performance can be gained using the hydrodynamic information from XRT. The following parameters were measured using the XRT method:

- Cross-sectional solids concentration – Φ_0
- Void volumes – V_b
- Void lengths – L_b
- Void rise velocities – U_v or U_b

Based on the assumptions discussed in Section 4.2.1, other hydrodynamic parameters are calculated. Assuming the bubble contains negligible solids, the voids fraction is:

$$\psi_B = \frac{\Phi_{mf} \Phi_0}{\Phi_{mf}} \quad 2-5$$

Assuming the bubbles have a cylindrical shape, the external bubble area per bubble volume can be calculated as follows:

$$d_{b(cyl)} = \sqrt{\frac{4V_b}{\pi L_b}} \quad 4-4$$

$$A_{b(cyl)} = 2 * \left\{ \frac{\pi}{4} (d_{b(cyl)})^2 \right\} + \pi L_b d_{b(cyl)} \quad 4-5$$

$$a_I = \frac{A_b}{V_b} \quad 4-6$$

As shown in [Chapter 3](#), a cylindrical shape approximates voids more accurately than a spherical shape. Lastly, the terminal bubble rise velocity (U_{br}) can be calculated; for U_b the values of U_v are used (see Section [3.2.3.2](#)):

$$U_b = U_o - U_{mf} + U_{br} \quad 2-4$$

The hydrodynamic considerations will only be based on averages calculated over the height of the reactor. This is because K_0 is an averaged parameter of the reactor. From the discussions in [Chapter 3](#) it is evident that the bed structure is not fully developed at the XRT measurement of 200 mm and consequently only the average between 300 mm, 400 mm and 500 mm will be used. No single parameters showed a turning behaviour and it is reasonable to assume that a combination of parameters is required to explain the trend. From the literature it is known that rise velocities are linked to specific mass transfer rates. Foka et al. [30] used the superficial velocity (U_0), of which the rise velocity is a function (see Section [2.5.1.1](#)). U_0 will therefore also be considered alongside the other measured hydrodynamic parameters. Let K_0 be some linear function of a combination of the parameters a_I , ψ_B , Φ_0 and U_0 :

$$K_0 \propto (a_I^k \psi_B^l \phi_0^m U_0^n) \quad 4-7$$

Using a line search optimization technique with k, l, m and n as the variables, the following combination had the best agreement with K_0 . These variables' values were very close to whole numbers and were therefore rounded.

$$K_0 \propto \frac{a_I^1 \psi_B^2}{\phi_0^2 U_0^1} \quad 4-8$$

[Figure 4.7](#) shows this parameter against velocity and the reactor performance against velocity. For both a turn is observed at 0.45 m/s.

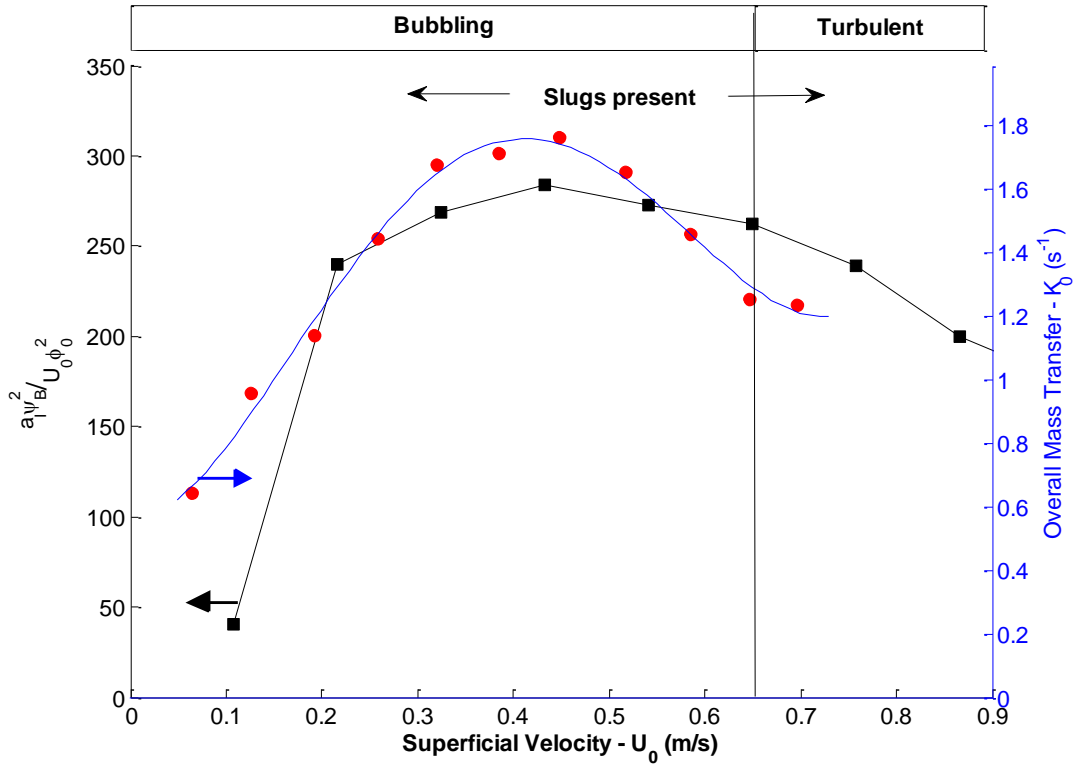


Figure 4.7: Combination of hydrodynamic parameters having the same trend as the reactor performance parameter K_0

4.3 Mass transfer correlations

The ideally structured and well-behaved voids of low-interaction bubbling beds differ considerably from the chaotic structures and behaviours at higher operating velocities. In this section the mass transfer nature of K_0 is investigated by means of the specific interphase mass transfer coefficient (k_{be}). Literature correlations are tested to evaluate the applicability over the entire bubbling regime. The absolute value of k_{be} is dependent on the model assumptions, two of which have already been deemed acceptable. The discussion is concerned mainly with the observed trends with superficial velocity. k_{be} is determined using the equation:

$$k_{be} = \frac{K_0 \Phi_0}{\phi_B a_i} \tag{4-2}$$

4.3.1 Penetration theory

In penetration theory (Section 2.5.1.2) k_{be} is generally a linear function of $(U_{br}/d_b)^{1/2}$. d_b represents the void height; it can therefore be replaced by L_b . Take Sit and Grace for instance:

$$\text{3D-column: } k_{be} = \frac{1}{3}u_{mf} + \left(\frac{4D_m \varepsilon_{mf} U_{br}}{\pi D_b}\right)^{\frac{1}{2}} \quad 2-50$$

The absolute correlation does not give a quantitatively good prediction, as seen in [Figure 4.8](#) (A-i). Hence, the constants in the correlation equation are combined:

$$k_{be} = c_p + m_p \left(\frac{U_{br}}{L_b}\right)^{\frac{1}{2}}$$

c_p and m_p represent all the constants. Using experimentally determined k_{be} and the XRT measurements for U_{br} and L_b over the entire velocity range of 0.11 m/s to 0.76 m/s, the best fit values for c_p and m_p were determined:

$$k_{be} = -0.0265 + 0.0245 \left(\frac{U_{br}}{L_b}\right)^{\frac{1}{2}} \quad 4-9$$

Higher velocity k_{be} values and possible experimental error caused the negative value of c_p . [Figure 4.8](#) (A-i) shows the prediction of this equation using XRT data compared with the measured k_{be} using the reactor performance data. The scatter in correlation is due to the scatter in the experimental values of U_{br} and L_b . The absolute percentage error is shown in [Figure 4.8](#) (A-ii); the line indicates the median error over the entire velocity range. For the entire velocity range the fit is not ideal; however, for the lower velocities ($U_0/U_c < 0.34$) the error is almost zero. This suggests that the mechanism of mass transfer proposed by penetration theory is only valid for low-interaction bubbling reactors.

4.3.2 Boundary layer theory

Two boundary layer correlations were mentioned in Section [2.5.1.1](#), namely Partridge and Rowe [13] and Foka et al. [30]. Foka et al. developed their correlation based on bubbling and turbulent regime data. The correlation by Partridge and Rowe is considered first:

$$\frac{k_{be} a_I \psi_B D_b}{\varepsilon_0 D_m} = 2 + 0.69 \left(\frac{\mu_g}{D_m \rho_g}\right)^{1/3} \left(\frac{\rho_g U_{br} D_b}{\mu_g}\right)^{1/2} \quad 2-38$$

This correlation performs exceptionally poorly as seen in [Figure 4.8](#) (B-i). From general observations in the literature it is found that authors prefer penetration theory correlations. Following the same argument as above, the constants are combined and a linear equation is obtained:

$$\frac{k_{be} a_I \psi_B L_b}{1 - \Phi_0} = c_B + m_B (U_{br} L_b)^{\frac{1}{2}}$$

c_B and m_B are the combinations of all the constants.

Using experimentally determined k_{be} and the XRT measurements for U_{br} and L_b over the entire velocity range of 0.11 m/s to 0.76 m/s, the best fit values for c_B and m_B were determined:

$$\frac{k_{be}a_I\psi_B L_b}{1-\Phi_0} = 0.3179 + 0.0366(U_{br}L_b)^{\frac{1}{2}} \quad 4-10$$

[Figure 4.8](#) (B-i) and (B-ii) shows the results. Relative to penetration theory, the predicted trend agreement is worse.

The correlation by Foka et al. has a direct proportionality and does not perform well:

$$k_{be}a_I = 1.631Sc^{0.37}U_0 \quad 2-40$$

The process of linearization was repeated, except that a linear equation was used which goes through the origin:

$$k_{be} = 1.8997\left(\frac{U_0}{a_I}\right) \quad 4-11$$

[Figure 4.8](#) (C-i) shows that the original correlation and the modified correlation do not differ significantly. This is due to fewer degrees of freedom in the number of fitting parameters. Although the correlation was designed to include the entire bubbling and turbulent regime, the errors are extremely large as shown in [Figure 4.8](#) (C-ii). Bi et al. mentioned that this correlation had not been extensively validated and should be used with caution [5].

4.3.3 Empirical correlation

Based on observations in [Figure 4.7](#), it is proposed to correlate k_{be} and $\psi_B/(\Phi_0 U_0)$. This parameter is referred to as β and is derived from Section [4.2.4](#):

$$\begin{aligned} K_0 &\propto \frac{a_I^1 \psi_B^2}{\phi_0^2 U_0^1} \\ \frac{K_0(\phi_0)}{(a_I \psi_B)} &\propto \frac{\psi_B}{\phi_0 U_0} \\ k_{be} &\propto \frac{\psi_B}{\phi_0 U_0} = \beta \end{aligned} \quad 4-12$$

Performing a linear fit through the origin gives:

$$k_{be} = 0.00568\beta \quad 4-13$$

[Figure 4.8](#) (D-i) shows this equation's prediction compared with the measured values and [Figure 4.8](#) (D-ii) shows the error. At 8% the lowest median of errors over the velocity range is obtained. This combination of hydrodynamic parameters fails to predict at the lowest velocity where ideal bubbling occurs. For the rest of the range ($U_0/U_c > 0.17$) good correlation

is obtained. The ideally structured and well-behaved voids of low-interaction bubbling beds differ considerably from the chaotic structures and behaviours at higher operating velocities. A single mass transfer correlation suitable for all velocity could therefore not be obtained. A change in mass transfer behaviour occurs around $U_0/U_c = 0.2$.

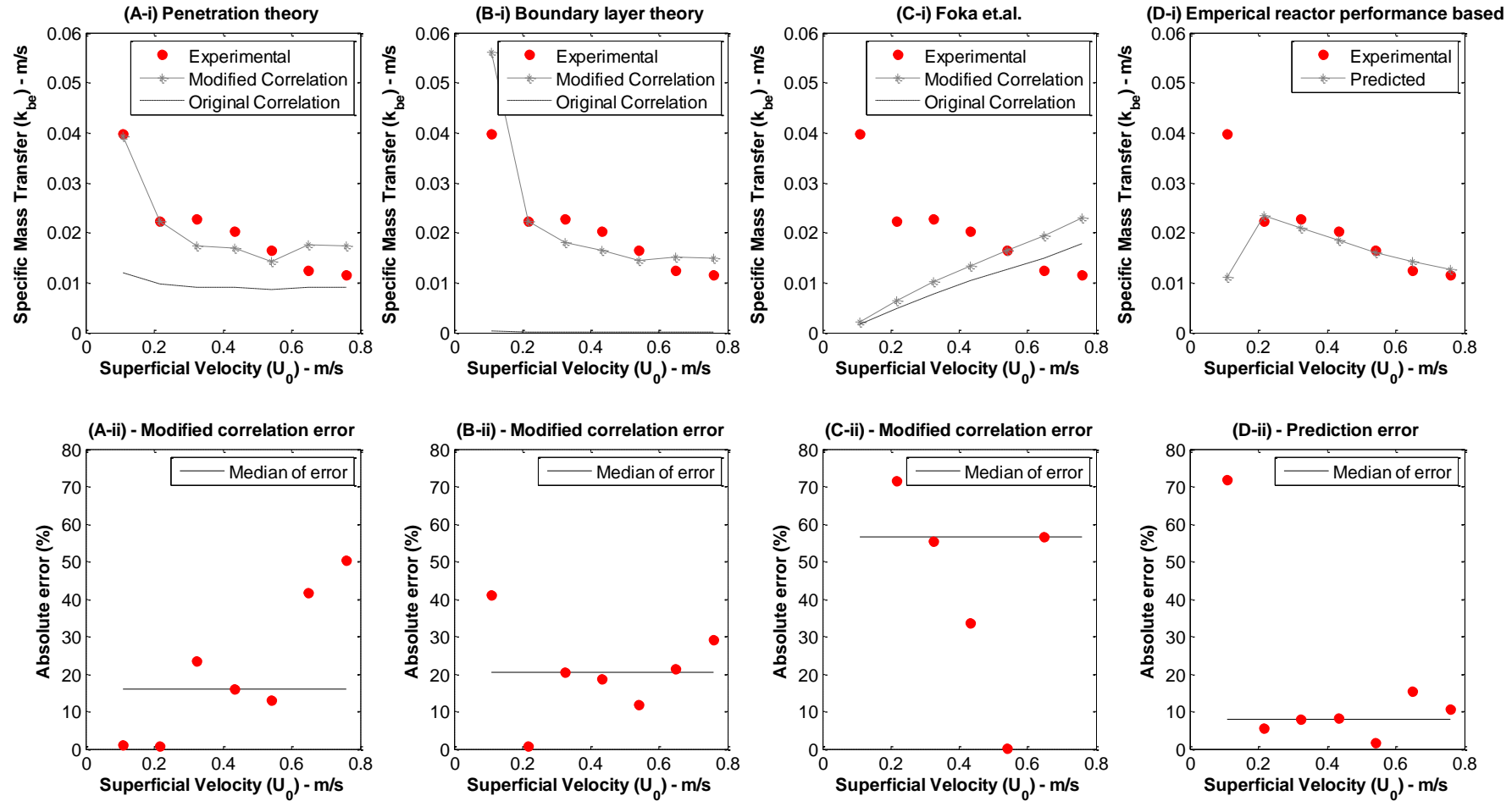


Figure 4.8: Predicted specific mass transfer compared with the measured specific mass transfer based on several theories and correlations. The error made in the modified correlation prediction is shown

4.4 Conclusions

Reactor performance was quantified using a basic two-phase model and an apparent mass transfer parameter. This revised method of analysis and quantification eliminated the need to stabilize the activity of the ozone decomposition catalyst.

As superficial velocity increased, reactor performance increased up to $U_0 = 0.45$ m/s, after which a decreasing trend was observed. The performance continued to decrease, reaching a plateau with superficial velocity at the bubbling-turbulent regime transition. The observed trend could be correlated using the following combination of hydrodynamic parameters:

$$K_0 \propto \frac{a_1^1 \psi_B^2}{\phi_0^2 U_0^1} \quad 4-8$$

Values from the XRT measurements were used in this chapter. However, it was shown that the pressure analysis technique of using the standard deviation of incoherence and a solids concentration probe gave similar hydrodynamic measurements.

Specific interphase mass transfer was investigated and it was found there is a distinct difference between low-interaction bubbling regime behaviour and high-interaction bubbling regime behaviour. Using the relationship between K_0 and k_{be} , the above equation was rewritten and an empirical correlation is suggested for k_{be} :

$$k_{be} \propto \frac{\psi_B}{\phi_0 U_0} = \beta \quad 4-12$$

β gave the best fit for the entire velocity range with an average error of 8%, although it is not recommended for $U_0/U_c < 0.17$. From a comparison of the classical approaches of penetration theory and boundary layer theory it was found that penetration theory performed better at low velocities ($U_0/U_c < 0.34$). The boundary between the low-interaction and high-interaction bubbling regimes occurs around a U_0/U_c of 0.2 for this system. A change in mass transfer behaviour is noted at this point.

Chapter 5 : Reactor Performance

Considerably more time was available on the reactor setup and additional investigations were performed without the associated XRT complement. Although the open literature contains numerous studies on fluidized bed hydrodynamics, very little is reported on highly dense particles [90,91]. Fluidized Bed Reactors (FBRs) utilizing high-density particles already exist in industry. An example, relevant to the South African economy, is the High Temperature Fisher-Tropsch (HTFT) reactor (Sasol Advanced Synthol or SAS reactor) operated with dense iron- or cobalt-based catalysts [3,4]. To the author's knowledge only two investigations focusing on extremely dense particle fluidization have been done. De Vos et al. investigated elutriation rates and entrainment of high-density iron-silicon (FeSi) particles [91]. Bischi et al. tested a novel Double Loop Circulating Fluidized Bed also utilizing FeSi particles [90]. FeSi is classified as Geldart A; it is, however, at the Geldart B boundary.

A major factor in any fluidized bed reactor, especially in the SAS reactors, is particle attrition [33,91]. Particle attrition causes particles to break up and consequently this process creates fines in an FBR. As discussed in Section [2.3.1](#), fines alter the hydrodynamics of a fluidized bed and in turn the reactor performance. The aim of this chapter is to quantify the reactor performance of a dense particle system and to observe the effect of fines on the reactor's performance. In addition, the effect of fines on the well-studied sand particle system is also investigated. The velocity range includes the bubbling regime up to the onset of the turbulent fluidization regime. Two particle types are investigated: sand and FeSi. Fines are added to each particle type, creating four particle systems.

5.1 Experimental

The same experimental procedure discussed in Section [4.1.3](#) was used for each particle system. FeSi is naturally active for ozone decomposition and requires no activation as was the case for sand. First-order behaviour could be verified for FeSi, as seen in [Figure 5.1](#). These measurements were made in a relatively short period before catalyst activity changes could occur.

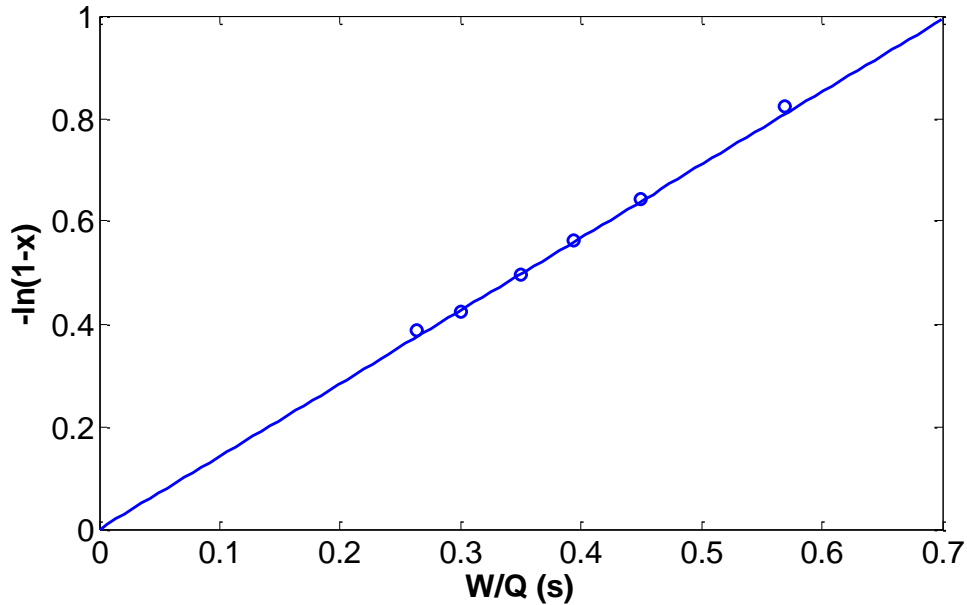


Figure 5.1: First-order behaviour confirmed for FeSi catalyst

The sand mixture and reaction results of [Chapter 4](#) will be referred to as the Sand baseline mixture. For sand, fines were added by removing 27 wt.% of the baseline mixture and replacing it with 27 wt.% of a fines mixture. Fines in this case were considered as particles smaller than 45 μm , as defined by Yates and Newton [41].

A mass of 37 kg of FeSi was loaded into the reactor. This batch of catalyst will be referred to as the FeSi baseline case. Similar to the sand system, it was shown 13.5 wt.% catalyst was in the solids return line and the catalyst inventory of the bed remained constant. Reaction experiments were done for the FeSi baseline mixture, after which 27 wt.% of the baseline mixture was replaced with 27 wt.% of a fines mixture. The definition of fines, according to Sun and Grace, is particles smaller than 20% of the Sauter mean [28]. However, equipment to obtain particles < 12 μm was not available and for the FeSi system particles < 21 μm are defined as fines. [Table 5-1](#) shows that U_{mf} decreased, which is expected as a result of fines addition [41]. Other system properties are also reported in the table.

Table 5-1: Catalyst and fluidizing medium properties

	Sand (Baseline)	Sand (Baseline with added fines)	FeSi (Baseline)	FeSi (Baseline with added fines)
ρ_p (kg/m ³)	2 450	2 450	6 690	6 690
ρ_b (kg/m ³)	1 450	1 620	3 650	3 920
\bar{d}_p (μ m)	101	81	59	41
Geldart	B	B	A/B	A/B
u_{mf} (mm/s)	9.1	4.0	6.5	5
ϵ_{mf}	0.41	0.34	0.46	0.42
μ_g (Pa.s)	18×10^{-6}	18×10^{-6}	18×10^{-6}	18×10^{-6}
ρ_g (kg/m ³)	1.2	1.2	1.2	1.2
D_m (m ² /s)	20×10^{-6}	20×10^{-6}	20×10^{-6}	20×10^{-6}

5.2 Estimation of bubble size

Calibration of the optical probe was repeated for each system of particles as discussed in Section 4.1.3. The voidage probe was used in addition to obtain an indication of bubble sizes. The method described in Section 2.2.2 was modified since only one probe was available. Using the probe-bubble contact time and a bubble rise velocity correlation, the bubble size was estimated. Karimipour and Pugsley [86] did a critical evaluation of all the available correlations, from which the most appropriate correlation was chosen for all the particle systems. The correlation of Werther (1978, included by the above authors) was used. It is valid for Geldart A and B particles:

$$u_b = \varphi \sqrt{9.81 D_b} \quad 5-1$$

$$\text{For Geldart A: } \varphi = 0.396 D^{0.4} \quad (10 \text{ cm} < D < 100 \text{ cm})$$

$$\text{For Geldart B: } \varphi = 0.254 D^{0.4} \quad (10 \text{ cm} < D < 100 \text{ cm})$$

The average between the φ for Geldart A and B is taken for FeSi since the particle systems of FeSi lie at the A/B boundary. Note that there is a difference between the average bubble size and the void length. To relate the void length distribution to an average bubble size, the equation of Liu and Clark [92] is required:

$$L_b = \left(\frac{2}{3} \alpha (1 + Q)^3 - \alpha Q (1 + Q)^2 \right) D_b \quad 5-2$$

where Q is the bubble wake shape factor.

With the probe-bubble contact time (t_1) and rise velocity correlation, a void length can now be determined:

$$L_b = t_1 u_{br} \quad 5-3$$

and it can be shown that:

$$D_b = \frac{8.56}{\left(\frac{2}{3}\alpha(1+Q)^3 - \alpha Q(1+Q)^2\right)^2} t_1^2 \quad 5-4$$

5.3 Results and discussion

[Appendix C](#) contains the conversion and catalyst activity data of these experiments. The voidage probe was not available for all the experiments with the FeSi baseline case. To eliminate the need for calculating averages, superficial velocity selection was done differently for FeSi: instead of a structured velocity-selection approach, as was followed for sand, velocities were selected randomly to create a band of data points. Using the basic two-phase model, reactor conversion and catalyst activity, the apparent overall mass transfer coefficient (K_0) could be determined. This was achieved by fitting the model's conversion to the actual conversion with an error smaller than $\pm 1\%$.

5.3.1 Regime quantification

The transition between the bubbling and turbulent fluidization flow regimes was determined using the standard deviation of pressure fluctuations technique [5]. When using absolute pressure measurements, a clear trend in the standard deviation could not be found. However, the differential pressure measurements between the 20 and 40 cm pressure probes did show a clear trend, as seen in [Figure 5.2](#). For the case of added fines it was found that the transition remained at 0.65 m/s. The standard deviation of pressure fluctuations of both the baseline case ([Chapter 4](#) results) and the XRT column ([Chapter 3](#) results) are shown. The XRT values are lower since these were determined using an absolute pressure signal and not a differential pressure signal. U_c did not change appreciably with the addition of fines.

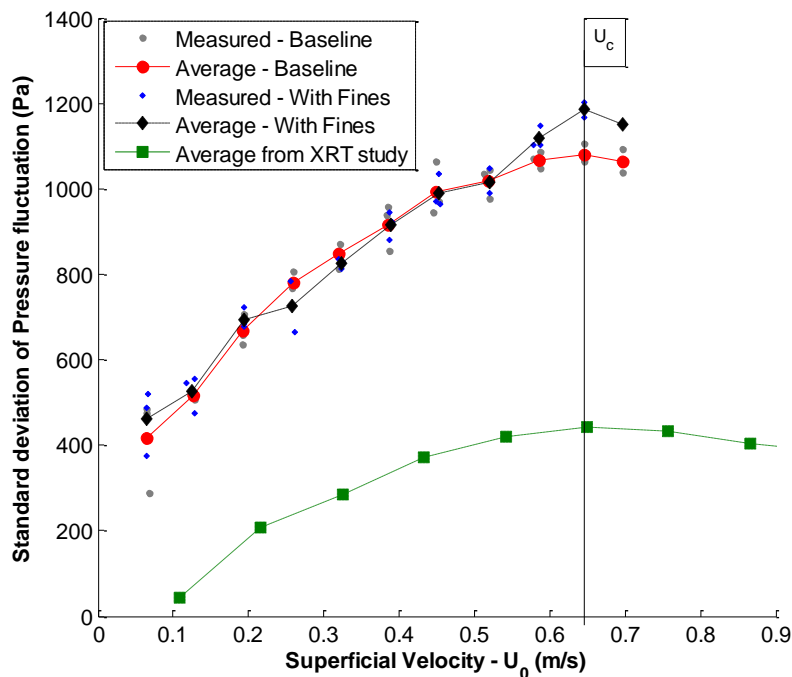


Figure 5.2: Regime transition confirmed to be at 0.65 m/s for sand

Figure 5.3 shows the results of the pressure analysis for FeSi. The different method of velocity selection resulted in a smooth band of data being created. The need for calculation of averages was eliminated. From visual inspection of the figure U_c is estimated at 0.36 m/s for the baseline system and at 0.33 m/s for the case with added fines. FeSi has a much lower u_c than suggested by correlations, which are in the order of 1.0 to 1.5 m/s as shown in Table 5-2. It should, however, be noted that the highest particle density used to obtain these correlations was $2\,970\text{ kg/m}^3$, whereas FeSi has a particle density double this figure. Turbulent regime was confirmed from visual observations. Features such as the diffused expanded bed surface and chaotic voids movement were observed.

Table 5-2: U_c correlations and predictions of the FeSi baseline system (as quoted by Arnaldos and Casal [46])

Authors	Equation	Predicted value (m/s)
Nakajima et al.	$Re_c = 0.633Ar^{0.467}$	1.00
Horio	$Re_c = 0.936Ar^{0.472}$	1.51
Lee and Kim	$Re_c = 0.7Ar^{0.485}$	1.18

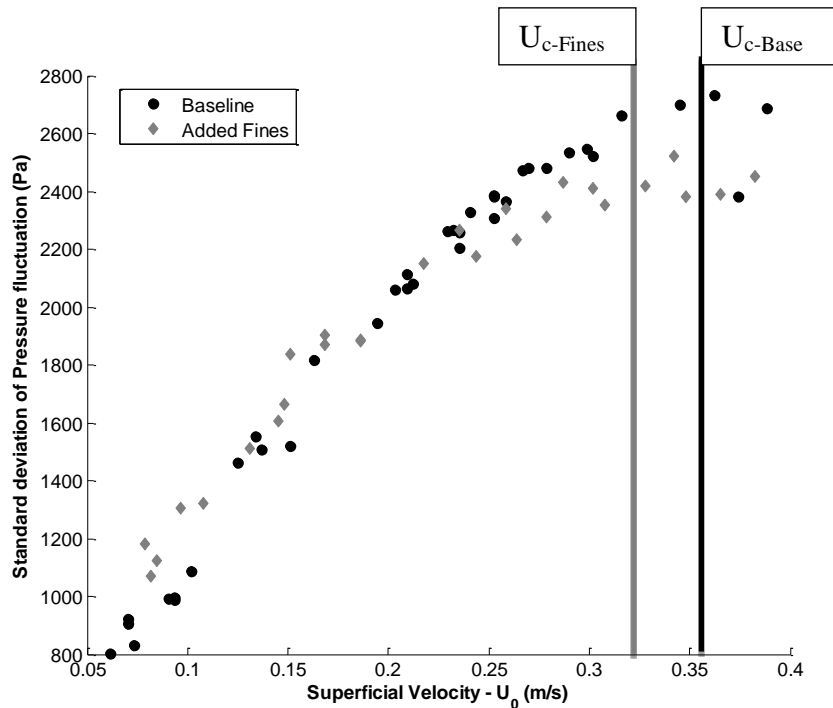


Figure 5.3: From visual inspection the standard deviations of differential pressure fluctuations show a U_c of 0.36 m/s for the baseline case and 0.33 m/s for the case of added fines. The different method of random velocity selection resulted in a smooth band of data being created

5.3.2 Reactor performance

Figure 5.4 shows the results for K_0 which were determined from the experimental data. The baseline case (Chapter 4) is also shown for comparative purposes. With the addition of fines, bubble sizes generally decrease and a better quality of fluidization is achieved [37,41,65], resulting in improved reactor performance. As expected from the literature, the addition of fines increased the reactor performance at the low bubbling velocities. Turning behaviour is observed in both cases. From tomography as well as from visual observations it is known that slugging is present for these particle systems. In the case where fines were added, the reactor performance between 0.5 and 0.6 m/s decreased to below the baseline case. Performance increased again once the turbulent regime started.

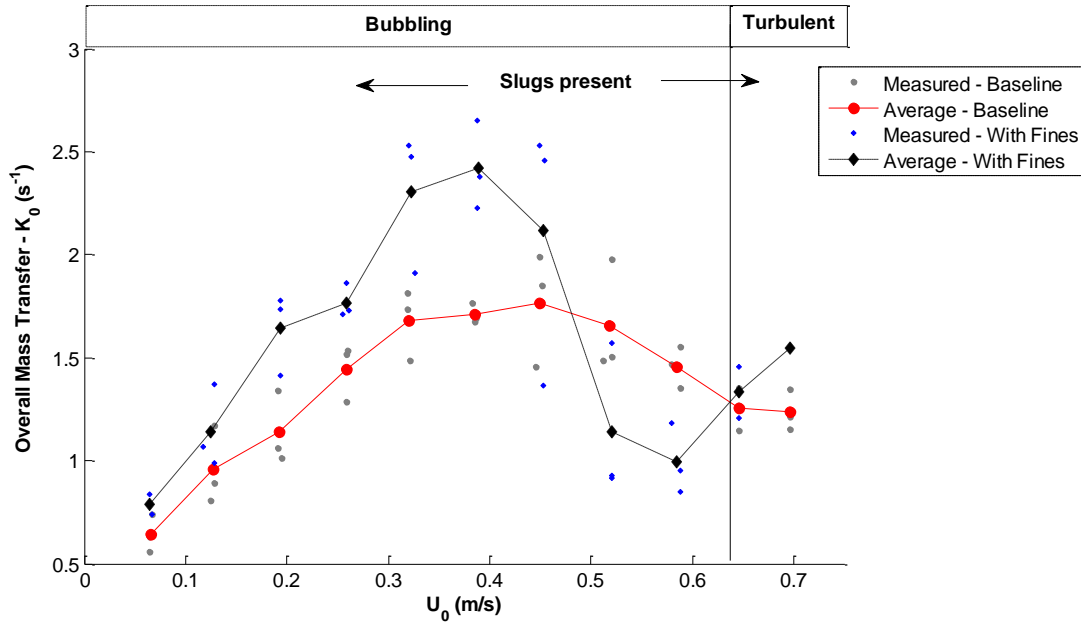


Figure 5.4: Reactor performance results for sand. Behaviour in the bubbling regime is as expected

The apparent overall mass transfer calculated from the experimental results for FeSi is plotted in [Figure 5.5](#). The ideal band of data, as seen in [Figure 5.3](#), resulting from the randomized velocity selection was not seen in the reactor performance. Using five consecutive data points for the baseline case and every four consecutive data points for the added fines case, an average and standard deviation were determined. Smaller markers indicate the experimental results, large markers are the averages and the bars indicate the standard deviation. An increasing trend with superficial velocity is seen. As with sand, it was expected that better reactor performance would be achieved with the addition of fines. [Figure 5.5](#) does not show any advantages from adding fines to the system: in fact, reactor performance decreased significantly with the addition of fines. Bubbles for the FeSi fines case were visually noted to be smoother and better defined. An in-depth investigation into the hydrodynamic differences between these two systems of FeSi is required to address why this unexpected behaviour is observed.

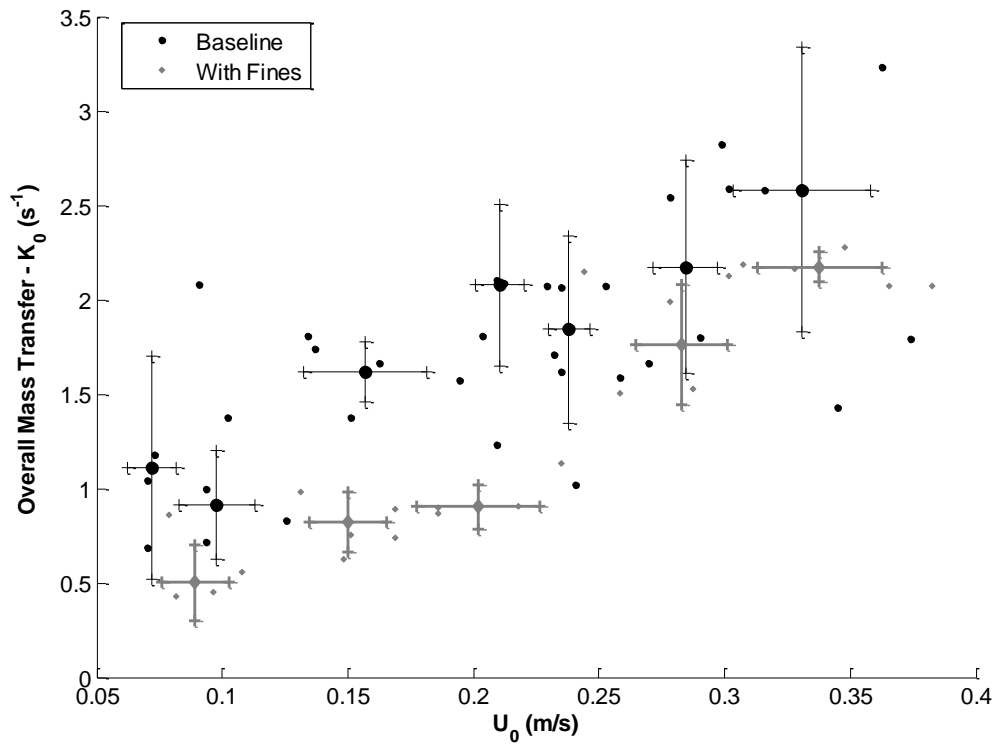


Figure 5.5: Reactor performance for FeSi showing an increasing trend. Statistical analysis was applied to every five consecutive data points for the “Baseline” case and to every four consecutive data points for the “With Fines” case. Bar plots indicate the relevant mean and standard deviations in the x- and y-directions of this analysis

5.3.3 Hydrodynamics

5.3.3.1 Bubble behaviour and sizes

[Figure 5.6](#) is the incoherent standard deviation. As found by Beetstra et al. [40], bubble sizes decrease with the addition of fines, as is evident in both graphs. As the superficial velocity is increased, the effect is enhanced even further.

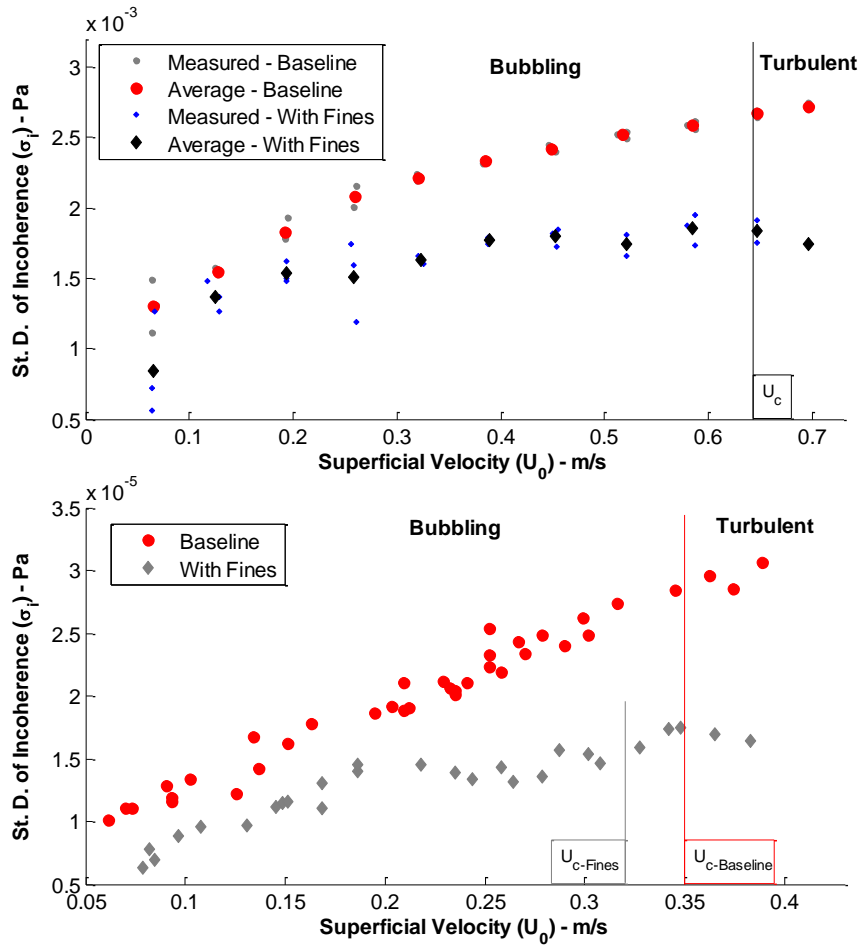


Figure 5.6: Incoherent standard deviation at 20 cm. Sand results are at the top and FeSi results at the bottom

Figure 5.7 shows the results of the bubble sizes derived from the voidage probe. Sand does not have acceptable agreement with the XRT measurements or the incoherence data of Figure 5.6. It needs to be kept in mind that this probe measurement is dependent on a bubble rise correlation. Both sand particle systems had slugging behaviour, which is the likely reason for the deviation. Bubble size measurements are required for specific mass transfer calculations and a different approach to ascertaining the slug sizes for the case of sand with added fines is needed. The incoherence ratio of the baseline case to the fines case (Figure 5.6) in conjunction with the baseline XRT measurements was used for specific mass transfer calculations, details of which are discussed in Section 5.3.4.

Good agreement between the incoherence and the probe measurement is obtained for FeSi. Slugging was not observed for the FeSi particle systems. Bubble size does not, however, explain the unexpected result of the reactor performance behaviour for FeSi. A decreased

bubble size would result in a larger bubble-emulsion transfer area and improved reactor performance.

In order to find a representative smoothed average for the FeSi data, the bubble size correlation of Cia et al. (1994) was taken from Karimipour and Pugsley (2011) and used in conjunction with a correction coefficient (k_{db}) to obtain an equation for the bubble size [86]:

$$D_{b-Correlation} = 0.138h^{0.8}(u_0 - u_{mf})^{0.42} e^{\{-2.5 \times 10^{-5}(u_0 - u_{mf})^2 - 10^{-3}(u_0 - u_{mf})\}} \quad 5-5$$

$$D_{b-FIT} = k_{db} * D_{b-Correlation} \quad 5-6$$

$$D_{b-FIT} = k_{db} * 0.138h^{0.8}(u_0 - u_{mf})^{0.42} e^{\{-2.5 \times 10^{-5}(u_0 - u_{mf})^2 - 10^{-3}(u_0 - u_{mf})\}} \quad 5-7$$

For the FeSi baseline case, k_{db} is 2.92 and for the FeSi case with added fines, it is 1.90.

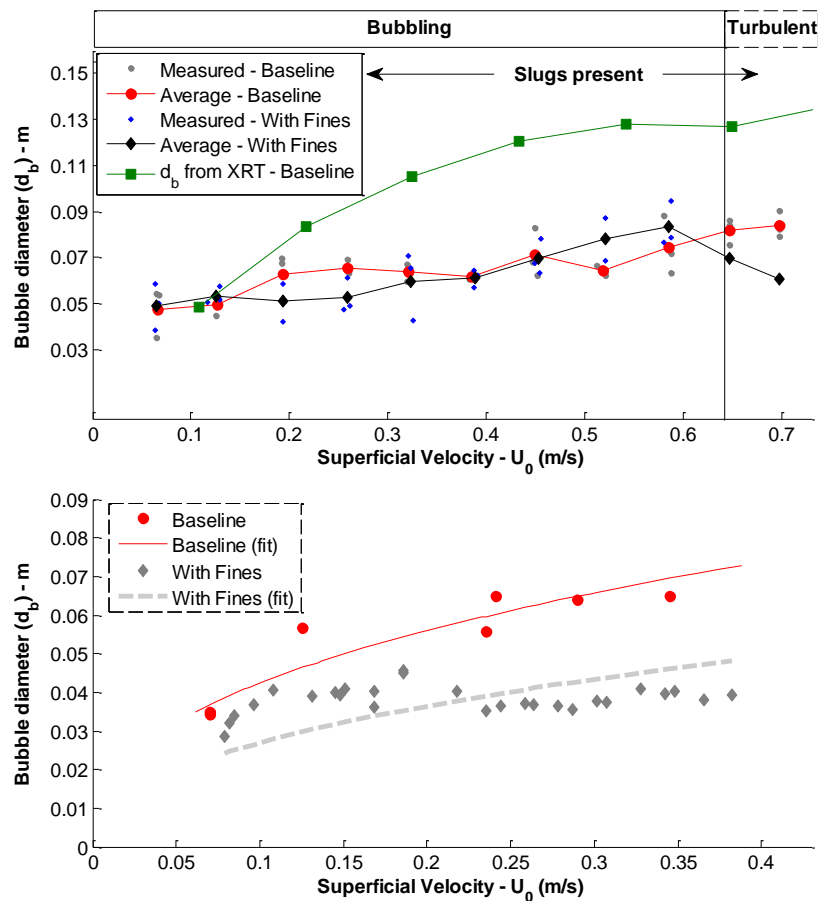


Figure 5.7: Bubble sizes from the voidage probe, showing equivalent void diameter at 0.20 m above the distributor. Sand results are in the top graph and FeSi results in the bottom graph. Good agreement between the incoherence and the probe measurement is obtained for FeSi; sand does not have acceptable agreement with the incoherence or XRT results

Some observations can also be made on the Geldart classification of FeSi. The baseline mixture of FeSi particles has bubble behaviour that is characteristic of Geldart B particles.

Bubbles grew significantly with superficial velocity. However, at U_{mf} , the bed of FeSi catalyst expanded approximately 8% without bubbles forming, which is characteristic of Geldart A particles. Accordingly, FeSi is more accurately classified as Geldart A/B.

5.3.3.2 Solids concentration

The mean solids concentration was calculated by averaging 5 min of voidage probe data at a specific velocity. Data are not available for all the runs of the baseline case. [Figure 5.8](#) shows the results. As stated in the introduction to this chapter, the addition of fines generally increases the bed voidage, implying that solids concentration decreases [31–34]. According to Yates and Newton [41], increased gas holdup in the emulsion phase is a key factor for increased reactor performance. For sand this trend is fully observed, but for FeSi the case with added fines clearly has a higher solids concentration, suggesting lower bubble holdup or a less expanded emulsion phase.

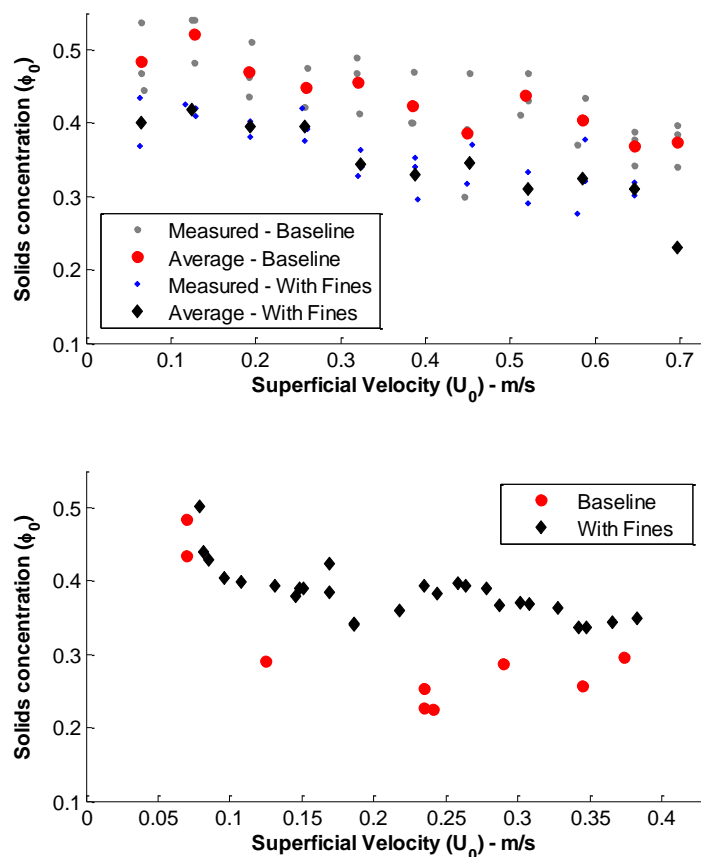


Figure 5.8: Average solids concentration showing that FeSi has an opposite trend from sand, with the addition of fines. These readings are from the voidage probe at $r/R=0$ and $h=0.20$ m. Sand results are at the top and FeSi results at the bottom

5.3.4 Specific mass transfer

The overall mass transfer (K_0) is converted to the specific mass transfer (k_{be}). Entrainment was measured for each system. Using the freeboard model of Kunii and Levenspiel [89] it was determined that the freeboard is responsible for only 5–8% of the conversion at the highest superficial velocity and even less at lower superficial velocities. The freeboard solids content was deemed negligible. Entrainment measurements are reported in [Appendix B](#). The limitations compared with the in-depth analysis of [Chapter 4](#) are:

- Averages calculated over the entire bed height are not possible for FeSi; parameters measured at 0.2 m above the distributor are used.
- Bubble sizes for FeSi are based on correlations ([Figure 5.7](#)).
- Some assumptions and XRT data will be required to ascertain the average bubble size and averaged solids concentration for the case of sand with added fines.

Bubble sizes are required for the determination of the specific area for inter-phase mass transfer (a_1). Due to the slugging nature of both systems of sand, values determined using XRT will have to be incorporated. The baseline sand values can be incorporated as is. For the added fines case, the assumption is made that the standard deviation of incoherence is an accurate representation of the bubble size behaviour and can correctly predict the degree of bubble size reduction. The ratio between the incoherence of the baseline case and the incoherence of the fines case is shown in [Figure 5.9](#). A linear fit is made to these ratio data and to the void length of baseline sand. Using these fits, the void length of the added fines case is calculated. The second assumption is that the cylinder diameter of the slugs is the same as that of the baseline sand – approx. 8 cm.

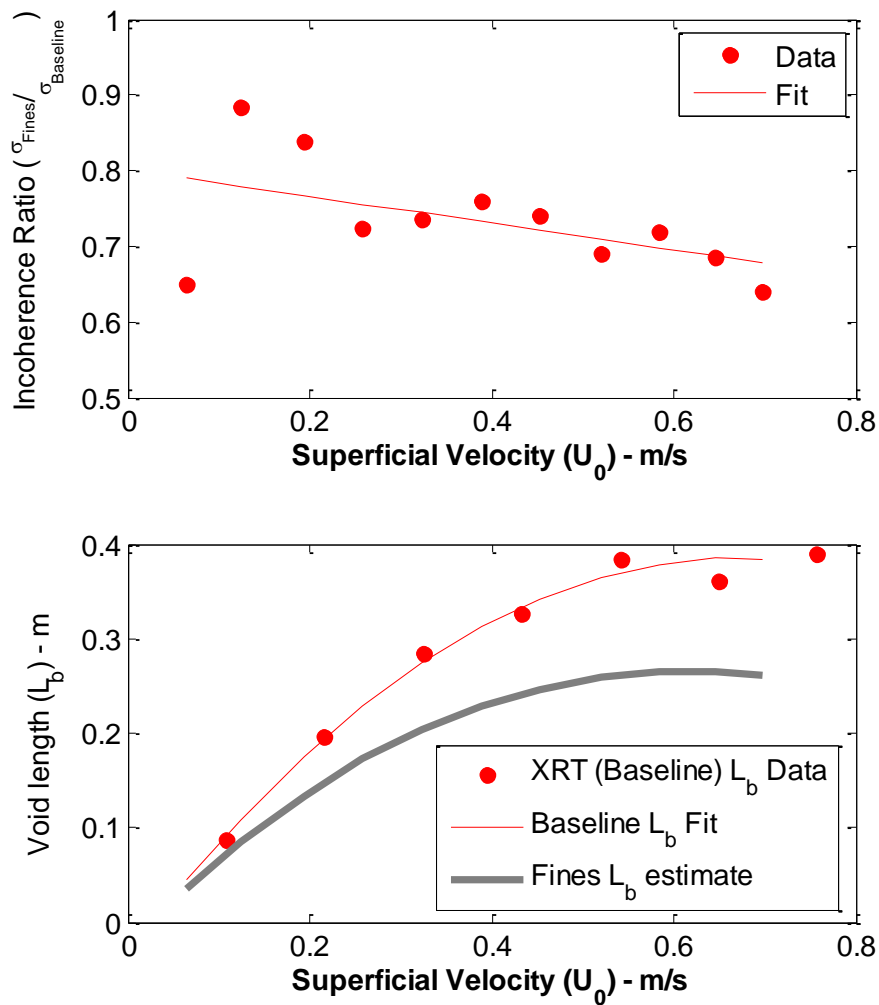


Figure 5.9: Calculating void lengths for the case of sand with added fines using incoherence data

Figure 5.10(a) shows the calculated k_{be} , the empirical β -correlation and the correlation of Sit and Grace [16] for the two sand systems. The Sit and Grace correlation and the measured interphase mass transfer are in a similar range, but the data do not agree perfectly with the predicted values over the entire superficial velocity range. Most researchers apply some correction factor to the correlation [25,27,62]. The relative differences between the two systems' correlations and data are similar in that both the correlation and the data show the case of added fines having a lower specific mass transfer. According to Sit and Grace, this is because of the convection term, which is a function of U_{mf} . The reactor performs better since the fines reduce bubble sizes and increase a_I .

The suggested β parameter of Section 4.3.3 agrees well with the trends of both the baseline and fines cases, although the constant coefficient of β will require modification for the fines case. This coefficient seems to depend on the system properties. The β parameter does not perform well at low velocities as seen here and in Section 4.3.3. The functionality of the proposed β correlation appears to be a viable subject for future investigations into high-velocity bubbling fluidized bed reactors.

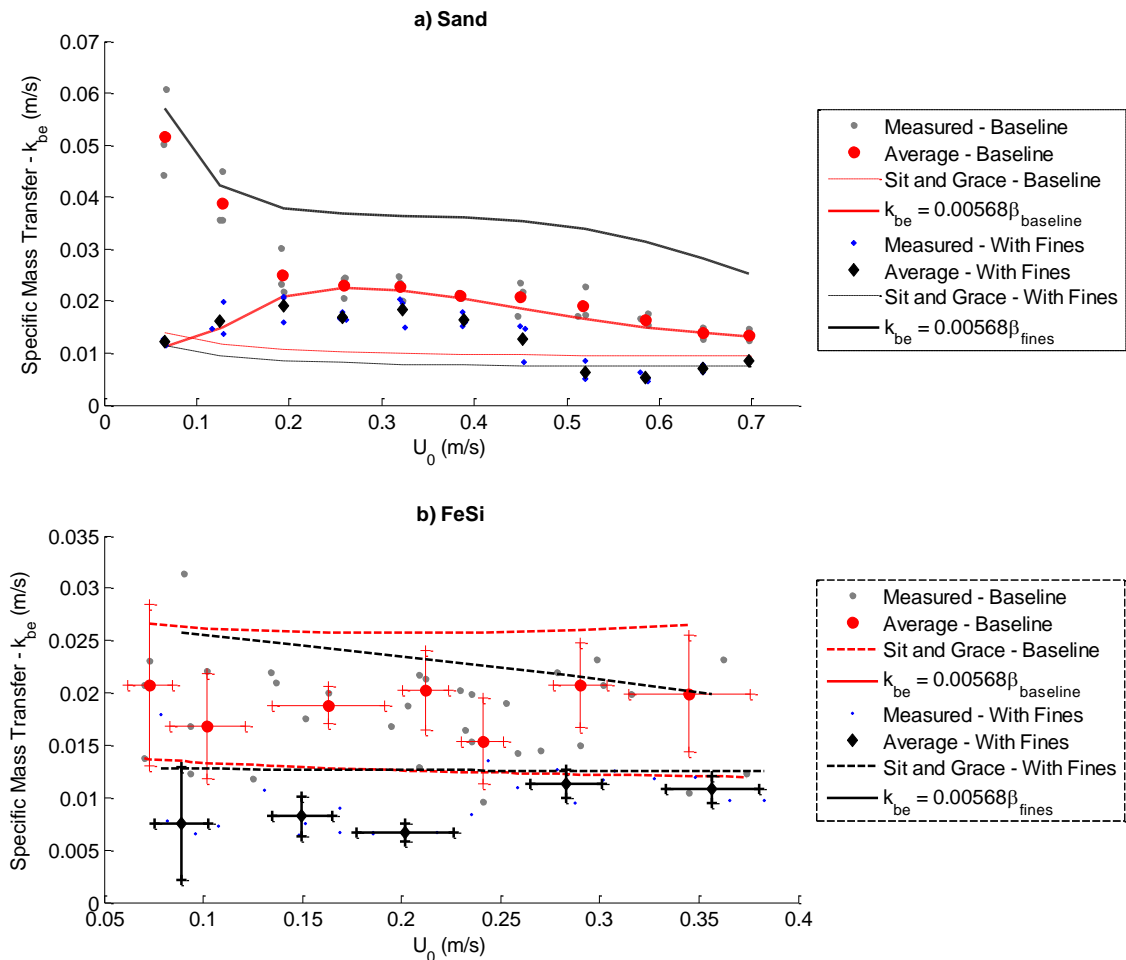


Figure 5.10: Specific mass transfer with superficial velocity. A statistical analysis was applied to every five consecutive data points for the FeSi “Baseline” case and every four consecutive data points for the FeSi “With Fines” case. Bar plots indicate the relevant mean and standard deviations in the x- and y-directions of this analysis

In Figure 5.10(b) the Sit and Grace correlation shows that the baseline k_{be} and the fines k_{be} should be similar. Yet the measured data show a considerable difference. The measured baseline k_{be} is twice the value of the fines k_{be} . Also seen is the trend of the fines data not

agreeing with the trend of the β parameter. In Section [4.2.1](#) the three assumptions which could bias k_{be} are mentioned:

- Solids content in the total disengagement height (TDH).
- Solids content in the bubbles.
- Gas flow in the emulsion phase is at U_{mf} .

The first two were deemed acceptable with a fair amount of certainty. The final assumption of negligible emulsion phase flow is now addressed.

5.3.5 Emulsion phase flow

[Figure 5.11](#) shows the solids concentration distributions of the baseline case and the case with added fines, at a low and a high superficial velocity. As was seen in the tomography investigation ([Figure 3.8](#)), two-phase behaviour is not yet observable for sand at 0.2 m above the distributor. What is evident from the figure is that the entire solids concentration distribution shifts to lower values with the addition of fines.

The FeSi data in [Figure 5.11](#) show that two-phase behaviour is already observable at 0.2 m above the distributor, as is evident from the bimodal distributions. The irregular shape of the peak is likely caused by the intrusive nature of the probe. More insight can be gained with regards to the emulsion phase density and flow. The distribution shifts upwards, opposite to what occurs with sand, with the addition of fines. The emulsion phase (sharp peak at high solids concentration) has a higher value for the fines case at both sets of velocities, suggesting that the emulsion phase would be less expanded for the fines case.

For the FeSi-type particles, K_0 showed that reactor performance decreases ([Figure 5.5](#)) with the addition of fines, and a collapse of the emulsion phase is observed in [Figure 5.11](#). It is reasonable to assume that less emulsion-phase gas flow would cause a less expanded emulsion phase since the local particle velocity needs to remain at the terminal particle velocity. These observations provide the most likely reason for the extreme difference in the calculated k_{be} 's of [Figure 5.10\(b\)](#), where similar specific mass transfer for the same particle type is expected. In contrast to the FeSi runs, the addition of fines to sand resulted in a bed expansion and likely an emulsion expansion as well. This expansion effect is much less severe than the collapse effect in FeSi reflected by similar k_{be} 's in [Figure 5.10\(a\)](#), suggesting that the sand system is more closely resembled by the classical two-phase models in which emulsion gas flow is assumed to be negligible. Yates and Newton postulated that gas flow in

the emulsion phase is a key factor for increased reactor performance when fines are added [41] but for FeSi it was found that the emulsion phase assumption should be used with some caution.

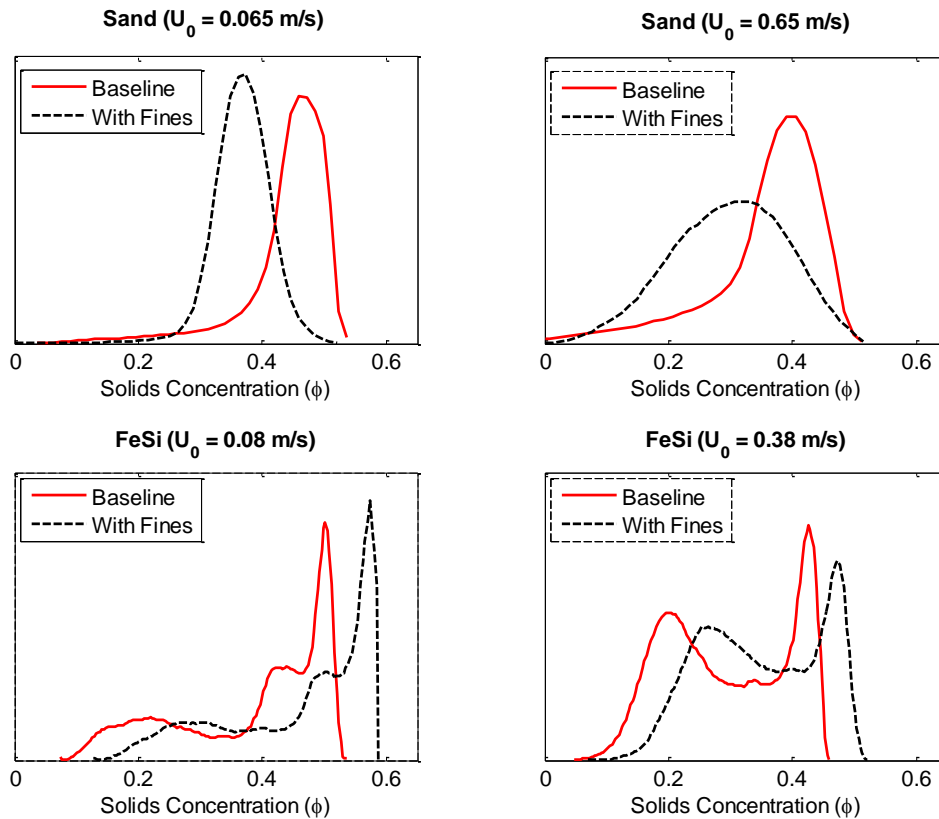


Figure 5.11: Solids concentration distribution at $r/R = 0$ and 0.2 m from the distributor. The distributions at low and high superficial velocities for the baseline case and the case with added fines are shown

5.4 Conclusions

The same method of reactor performance quantification employed in [Chapter 4](#) was used with an extremely high-density FeSi particle type. Two systems of this particle type were tested, each having a different proportion of fines. The addition of fines decreased the overall reactor performance of FeSi. Simultaneously, hydrodynamic measurements were made to observe the underlying causes. Solids concentrations unexpectedly increased with the addition of fines, whereas bubble sizes followed expected behaviour and decreased. Calculated k_{be} values could not explain the observed reactor performance behaviour, but emulsion phase flow could do so. It was shown that the emulsion phase collapsed indicating

decreased through flow in the phase. Yates and Newton [41] postulated that emulsion phase flow is not necessarily a negligible model parameter.

The technique was verified using the well-studied system of sand particles described in the previous chapters, in conjunction with the addition of fines. As in other conversion studies using fines [28,41], the method showed increased reactor performance with the addition of fines for the sand particle type. Both measured hydrodynamic parameters changed advantageously: bubble sizes decreased, which in theory creates more area for interphase mass transfer, and solids concentrations decreased, meaning higher gas holdup in the bed. The theory of Newton and Yates [41] of more gas flow through the emulsion phase could not be confirmed experimentally with solids concentration distributions. However, it was concluded that the sand system more closely resembles the classical two-phase models in which emulsion gas flow is assumed to be negligible.

Chapter 6 : Concluding Remarks

The hydrodynamics and reactor performance of a 14 cm (ID) catalytic Fluidized Bed Reactor (FBR) were investigated using an integrated approach. Two particle types were used, namely Geldart B sand particles and high-density ferro-silicon (FeSi) particles. Fines were added to each particle type to create four particle systems:

- Sand baseline
- Sand with fines
- FeSi baseline
- FeSi with fines

The entire bubbling regime, including the onset of the turbulent regime, was the main interest of this work. An optical probe and pressure measurements were used to obtain information on the hydrodynamics of the different particle systems. In addition, an advanced method of fast X-Ray Tomography (XRT) was employed to obtain highly detailed hydrodynamic information on the sand baseline system. The XRT investigation included the fast fluidization flow regime. Reactor performance was quantified using the ozone decomposition reaction, a basic two-phase model and an apparent overall interphase mass transfer parameter, K_0 . The technique of reactor performance quantification could be verified using the sand with fines system. As for previous conversion studies using fines [28,41], the method showed improved hydrodynamics and increased reactor performance for the well-studied sand particle type.

The main findings and contributions of this work were:

- For the sand baseline system, reactor performance increased up to $U_0/U_c = 0.7$, after which a decreasing trend was observed. Based on the XRT-determined hydrodynamics and reactor performance, an empirical trend correlation was proposed for the specific interphase mass transfer (k_{be}) for the higher velocity bubbling regime:

$$k_{be} \propto \frac{\psi_B}{\phi_0 U_0} = \beta \tag{4-12}$$

This hydrodynamic parameter, β , gave the best fit for the entire velocity range with an average error of 8%, although it is not recommended for $U_0/U_c < 0.17$. The classical approach of penetration theory for interphase mass transfer, performed extremely well at low velocities ($U_0/U_c < 0.34$). A change in mass transfer behaviour occurs around a U_0/U_c

of 0.25 for the combination of sand and a 14 cm (ID) column. A distinction should be made between the low-interaction bubbling regime and the high-interaction bubbling regime.

- For the FeSi particle type, the addition of fines decreased the overall reactor performance. Solids concentrations unexpectedly increased, whereas bubble sizes followed expected decreasing behaviour. The bubble behaviour would cause an increase in reactor performance. Calculated k_{be} values could also not explain the observed reactor performance behaviour; however, emulsion-phase flow could. A collapse of the emulsion phase was shown, which would decrease the through flow in this phase. It was postulated that through flow in the emulsion phase is much higher for the FeSi baseline system and decreases with the addition of fines. Yates and Newton [41] similarly postulated that emulsion-phase flow is not always a negligible model parameter.
- For the sand particle type, both measured hydrodynamic parameters changed advantageously with the addition of fines: Solids concentrations decreased and bubble sizes decreased. The theory of emulsion-phase through flow could not be confirmed with the available solids concentration distributions as with FeSi. Based on the available data, it was postulated that the sand system more closely resembles the classical two-phase models in which emulsion-phase gas flow is assumed to be negligible.
- When XRT was used, very distinct hydrodynamic behaviour was observed for all the fluidization regimes. Probability density distributions show that there were still two phases present in the turbulent regime and that the emulsion-phase solids concentration remains independent of velocity until fast fluidization sets in. It was further shown that the turbulent regime has unique hydrodynamic behaviour, although voids appear to be a transient structure between the structures of the bubbling and fast fluidization regimes.
- FeSi is Geldart A/B and has properties of both Geldart groups. Bubbles grew significantly with superficial velocity. However, at U_{mf} , the bed of FeSi catalyst expanded approximately 8% without bubbles forming, which is characteristic of Geldart A particles.

A correlation between the hydrodynamic measurements and the specific mass transfer was obtained. There is scope for an extended investigation into a new mass transfer correlation which would be more suited for the higher velocity spectrum of the bubbling regime ($U_0/U_c > 0.2$). Lastly, the influence of emulsion flow on reactor performance was examined and it is evident that the mathematical approach to this phenomenon is lacking in FBR modelling.

References

- [1] J. Saayman, W. Nicol, Demonstrating the effect of interphase mass transfer in a transparent fluidized bed reactor, *Chemical Engineering Education*, 45 (2011) 178–183.
- [2] J.R. van Ommen, J.M. Valverde, R. Pfeffer, Fluidization of nanopowders: a review., *Journal of Nanoparticle Research*, 14 (2012) 737.
- [3] D.J. Duvenhage, T. Shingles, Synthol reactor technology development, *Catalysis Today*, 71 (2002) 301–305.
- [4] A. P. Steynberg, R.L. Espinoza, B. Jager, A.C. Vosloo, High temperature Fischer–Tropsch synthesis in commercial practice, *Applied Catalysis A: General*, 186 (1999) 41–54.
- [5] H.T. Bi, N. Ellis, I.A. Abba, J.R. Grace, A state-of-the-art review of gas-solid turbulent fluidization, *Chemical Engineering Science*, 55 (2000) 4789–4825.
- [6] P.N. Rowe, B.A. Partridge, E. Lyall, G.M. Ardran, Bubbles in Fluidized Beds, *Nature*, 195 (1962) 278–279.
- [7] P.N. Rowe, B.A. Partridge, Gas flow through bubbles in a fluidized bed - I. Flow through an ideal bubble, *Chemical Engineering Science*, 18 (1963) 511–524.
- [8] J.F. Davidson, D. Harrison, The behaviour of a continuously bubbling fluidised bed, *Chemical Engineering Science*, 21 (1966) 731–738.
- [9] J.F. Davidson, D. Harrison, *Fluidized Particles*, 1st ed., New York, Cambridge University Press, 1963.
- [10] M.J. Lockett, J.F. Davidson, D. Harrison, On the two-phase theory of fluidization, *Chemical Engineering Science*, 22 (1967) 1059–1066.
- [11] G.K. Stephens, R.J. Sinclair, O.E. Potter, Gas Exchange between Bubbles and Dense Phase in a Fluidised Bed, *Powder Technology*, 1 (1967) 157–166.
- [12] K. Godard, J.F. Richardson, Distribution of gas flow in a fluidised bed, *Chemical Engineering Science*, 23 (1968) 660.
- [13] A.A.H. Drinkenburg, K. Rietema, Gas transfer from bubbles in a fluidized bed to the dense phase—I. Theory, *Chemical Engineering Science*, 27 (1972) 1765–1774.
- [14] C. Chavarie, J.R. Grace, Interphase Mass Transfer in a Gas-Fluidized Bed, *Chemical Engineering Science*, 31 (1975) 741–749.

- [15] S.P. Sit, J.R. Grace, Interphase Mass Transfer in an Aggregative Fluidized Bed, *Chemical Engineering Science*, 33 (1978) 1115–1122.
- [16] S.P. Sit, J.R. Grace, Effect of Bubble Interaction on Interphase Mass Transfer in Gas Fluidized Beds, *Chemical Engineering Science*, 36 (1981) 327–335.
- [17] C. Chavarie, J.R. Grace, Performance Analysis of a Fluidized Bed Reactor. II. Observed Reactor Behavior Compared with Simple Two-Phase Models, *Industrial & Engineering Chemistry Fundamentals*, 14 (1975) 79–86.
- [18] C. Chavarie, J.R. Grace, Performance Analysis of a Fluidized Bed Reactor. I. Visible Flow Behavior, *Industrial & Engineering Chemistry Fundamentals*, 14 (1975) 75–79.
- [19] C. Chavarie, J.R. Grace, Performance analysis of a fluidized bed reactor. III. Modification and extension of conventional two-phase models, *Industrial & Engineering Chemistry Fundamentals*, 14 (1975) 86–91.
- [20] J.R. Grace, Generalized Models for Isothermal Fluidized Bed Reactors, in: L.K. Doraiswamy (Ed.), *Recent Advances in the Engineering Analysis of Chemically Reacting Systems*, New Delhi, Wiley Eastern (1984) pp. 237–255.
- [21] D. Kunii, O. Levenspiel, Fluidized reactor models. 1. For bubbling beds of fine, intermediate, and large particles. 2. For the lean phase: freeboard and fast fluidization, *Industrial & Engineering Chemistry Research*, 29 (1990) 1226–1234.
- [22] D. Kunii, O. Levenspiel, Entrainment of solids from fluidized beds I. Hold-up of solids in the freeboard II. Operation of fast fluidized beds, *Powder Technology*, 61 (1990) 193–206.
- [23] I.A. Abba, J.R. Grace, H.T. Bi, Spanning the Flow Regimes : Generic Fluidized-Bed Reactor Model, *AIChE Journal*, 49 (2003) 1838–1848.
- [24] J. Chaouki, A. Gonzalez, C. Guy, D. Klvana, Two-phase model for a catalytic turbulent fluidized-bed reactor: Application to ethylene synthesis, *Chemical Engineering Science*, 54 (1999) 2039–2045.
- [25] M. Thompson, H. Bi, J.R. Grace, A generalized bubbling/turbulent fluidized-bed reactor model, *Chemical Engineering Science*, 54 (1999) 3–10.
- [26] R. Jafari, R. Sotudeh-Gharebagh, N. Mostoufi, Performance of the wide-ranging models for fluidized bed reactors, *Advanced Powder Technology*, 15 (2004) 533–548.
- [27] W. Wu, P.K. Agarwal, The Effect of Bed Temperature on Mass Transfer Fluidized Bed, *The Canadian Journal of Chemical Engineering*, 81 (2003) 940–948.
- [28] G. Sun, J.R. Grace, The Effect of Particle Size Distribution on the Performance of a Catalytic Fluidized Bed Reactor, *Chemical Engineering Science*, 45 (1990) 2187–2194.

- [29] J.B.L.M. Campos, O.D.S. Mota, A.M.F.R. Pinto, Measurement of Mass Transfer between the Bubble and Dense Phases in a Fluidized Bed Combustor, *Combustion and Flame*, 116 (1998) 105–119.
- [30] M. Foka, J. Chaouki, C. Guy, D. Klvana, Gas phase hydrodynamics of a gas-solid turbulent fluidized bed reactor, *Chemical Engineering Science*, 51 (1996) 713–723.
- [31] H.O. Kono, C.C. Huang, E. Morimoto, T. Nakayama, T. Hikosaka, Segregation and agglomeration of Type C powders from homogeneously aerated Type A–C powder mixtures during fluidization, *Powder Technology*, 53 (1987) 163–168.
- [32] P.U. Foscolo, R. Di Felice, L.G. Gibilaro, An Experimental Study of the Expansion Characteristics of Gas Fluidized Beds of Fine Catalyst, *Chemical Engineering and Processing*, 22 (1987) 69–78.
- [33] M.J. Lorences, G.S. Patience, F. V Díez, J. Coca, Fines effects on collapsing fluidized beds, *Powder Technology*, 131 (2003) 234–240.
- [34] R.J. Dry, I.N. Christensen, G.C. Thomas, The Effect of Naturally-Occurring Interparticle Forces on the Fluidisation Characteristics of Fine Iron Oxide Powders, *Chemical Engineering Science*, 43 (1988) 1033–1038.
- [35] J. Baeyens, S. Geldart, S.Y. Wu, Elutriation of fines from gas fluidized beds of Geldart A-type powders—effect of adding superfines, *Powder Technology*, 71 (1992) 71–80.
- [36] X. Ma, K. Kato, Effect of interparticle adhesion forces on elutriation of fine powders from a fluidized bed of a binary particle mixture, *Powder Technology*, 95 (1998) 93–101.
- [37] J.R. Grace, G. Sun, Influence of particle size distribution on the performance of fluidized bed reactors, *The Canadian Journal of Chemical Engineering*, 69 (1991) 1126–1134.
- [38] D. Bai, Y. Masuda, N. Nakagawa, K. Kato, Transition to turbulent fluidization in a binary solids fluidized bed, *Canadian Journal of Chemical Engineering*, 74 (1996) 58–62.
- [39] J.-H. Choi, H.-J. Ryu, C.-K. Yi, Type transition in onset condition of turbulent fluidization, *Korean Journal of Chemical Engineering*, 28 (2011) 2009–2011.
- [40] R. Beetstra, J. Nijenhuis, N. Ellis, J.R. van Ommen, The Influence of the Particle Size Distribution on Fluidized Bed Hydrodynamics Using High-Throughput Experimentation, *AIChE Journal*, 55 (2009) 2013–2023.
- [41] J.G. Yates, D. Newton, Fine Particle Effects in a Fluidized-bed Reactor, *Chemical Engineering Science*, 41 (1986) 801–806.
- [42] W.-C. Yang, Bubbling Fluidized Beds, In: W.-C. Yang (Ed.), *Handbook of Fluidization and Fluid-Particle Systems*, 1st ed., New York, Marcel Dekker, 2003: pp. 53–112.

- [43] D. Kunii, O. Levenspiel, *Fluidization Engineering*, 2nd ed., Sydney, Australia, Butterworth-Heinemann, 1991.
- [44] O. Levenspiel, *Chemical Reaction Engineering*, 3rd ed., New York, Wiley, 1999.
- [45] D. Kunii, O. Levenspiel, Circulating fluidized-bed reactors, *Chemical Engineering Science*, 52 (1997) 2471–2482.
- [46] J. Arnaldos, J. Casal, Prediction of transition velocities and hydrodynamical regimes in fluidized beds, *Powder Technology*, 86 (1996) 285–298.
- [47] R.F. Mudde, Advanced measurement techniques for GLS reactors, *The Canadian Journal of Chemical Engineering*, 88, 4 (2010) 638–647.
- [48] J.R. van Ommen, S. Sasic, J. van der Schaaf, S. Gheorghiu, F. Johnsson, M.-O. Coppens, Time-series analysis of pressure fluctuations in gas–solid fluidized beds – A review, *International Journal of Multiphase Flow*, 37 (2011) 403–428.
- [49] J. van der Schaaf, J.C. Schouten, F. Johnsson, C.M. Van den Bleek, Non-intrusive determination of bubble and slug length scales in fluidized beds by decomposition of the power spectral density of pressure time series, *International Journal of Multiphase Flow*, 28 (2002) 865–880.
- [50] M. Rudisuli, T.J. Schildhauer, S.M. Biollaz, J.R. van Ommen, Bubble characterization in a fluidized bed by means of optical probes, *International Journal of Multiphase Flow*, 41 (2012) 56–67.
- [51] N. Ellis, H.T. Bi, C.J. Lim, J.R. Grace, Influence of probe scale and analysis method on measured hydrodynamic properties of gas-fluidized beds, *Chemical Engineering Science*, 59 (2004) 1841–1851.
- [52] X. Zhang, H.T. Bi, Study on Void Behavior in a Turbulent Fluidized Bed with Catalyst Powders, *Industrial & Engineering Chemistry Research*, 49 (2010) 6862–6869.
- [53] H. Zhu, J. Zhu, G. Li, F. Li, Detailed measurements of flow structure inside a dense gas–solids fluidized bed, *Powder Technology*. 180 (2008) 339–349.
- [54] M. Bieberle, F. Barthel, U. Hampel, Ultrafast X-ray computed tomography for the analysis of gas–solid fluidized beds, *Chemical Engineering Journal*, 189-190 (2012) 356–363.
- [55] R.F. Mudde, Double X-ray Tomography of a Bubbling Fluidized Bed, *Industrial & Engineering Chemistry Research*, 49 (2010) 5061–5065.
- [56] R.F. Mudde, Bubbles in a Fluidized Bed : A Fast X-Ray Scanner, *AIChE Journal*, 57 (2011).
- [57] C. Rautenbach, R.F. Mudde, X. Yang, M.C. Melaen, B.M. Halvorsen, A comparative study between electrical capacitance tomography and time-resolved X-raytomography, *Flow Measurement and Instrumentation*, 30 (2013) 34–44.

- [58] J. Saayman, Bubbling to Turbulent Regime Transition in a 2D Catalytic Fluidized Bed Reactor, MSc dissertation, University of Pretoria, 2009.
- [59] B. Dhandapani, S.T. Oyama, Gas phase ozone decomposition catalysts, *Applied Catalysis B: Environmental*, 11 (1997) 129–166.
- [60] W.T. Tsai, C.Y. Chang, F.H. Jung, C.Y. Chiu, W.H. Huang, Y.H. Yu, et al., Catalytic decomposition of ozone in the presence of water vapor, *Journal of Environmental Science and Health, Part A*, 33 (1998) 1705–1717.
- [61] C.Y. Chang, W.T. Tsai, L. Cheng, Catalytic Decomposition of Ozone in Air, *Journal of Environmental Science and Health . Part A: Environmental Science and Engineering and Toxicology*, 32 (1997) 1837–1847.
- [62] H.G. Brink, J. Saayman, W. Nicol, Two Dimensional Fluidised Bed Reactor: Performance of a Novel Multi-Vortex Distributor, *Chemical Engineering Journal*, 175 (2011) 484–493.
- [63] G. Sun, J.R. Grace, Experimental determination of particle dispersion in voids in a fluidized bed, *Powder Technology*, 80 (1994) 29–34.
- [64] G. Sun, Influence of Particle Size Distribution on the Performance of Fluidized Bed Reactors, Vancouver, Canada, Department of Chemical Engineering, University of British Columbia, 1991.
- [65] J.R. Grace, G. Sun, Fines Concentration in Voids in Fluidized Beds, *Powder Technology*, 62 (1990) 203–205.
- [66] S. Pagliolico, M. Tiprigan, G. Rovero, A. Gianetto, Pseudo-homogeneous Approach to CFB Reactor Design, *Chemical Engineering Science*, 47 (1992) 2269–2274.
- [67] H. Schoenfelder, M. Kruse, J. Werther, Two-dimensional model for circulating fluidized-bed reactors, *AIChE Journal*, 42 (1996) 1875–1888.
- [68] A. Therdthianwong, P. Pantarak, S. Therdthianwong, Modeling and simulation of circulating fluidized bed reactor with catalytic ozone decomposition reaction, *Powder Technology*, 133 (2003) 1–14.
- [69] S. Zimmermann, F. Taghipour, CFD modeling of the hydrodynamics and reaction kinetics of FCC fluidized-bed reactors, *Industrial & Engineering Chemistry Research*, 44 (2005) 9818–9827.
- [70] C. Fan, Y. Zhang, X. Bi, W. Song, W. Lin, L. Luo, Evaluation of downer reactor performance by catalytic ozone decomposition, *Chemical Engineering Journal*, 140 (2008) 539–554.
- [71] C. Fan, X. Bi, W. Lin, W. Song, Mass transfer and reaction performance of the downer and its hydrodynamic explanation, *The Canadian Journal of Chemical Engineering*, 86 (2008) 436–447.

- [72] N. Ellis, H.T. Bi, C.J. Lim, J.R. Grace, Hydrodynamics of turbulent fluidized beds of different diameters, *Powder Technology*, 141 (2004) 124–136.
- [73] B. Du, W. Warsito, L. Fan, Bed Nonhomogeneity in Turbulent Gas-Solid Fluidization, *AIChE Journal*, 49 (2003) 1110–1126.
- [74] Y.T. Makkawi, P.C. Wright, Fluidization regimes in a conventional fluidized bed characterized by means of electrical capacitance tomography, *Chemical Engineering Science*, 57 (2002) 2411–2437.
- [75] Y.T. Makkawi, P.C. Wright, Electrical capacitance tomography for conventional fluidized bed measurements—remarks on the measuring technique, *Powder Technology*, 148 (2004) 142–157.
- [76] G.C. Brouwer, E.C. Wagner, J.R. van Ommen, R.F. Mudde, Effects of pressure and fines content on bubble diameter in a fluidized bed studied using fast X-ray tomography, *Chemical Engineering Journal*, 207–208 (2012) 711–717.
- [77] A. Mahecha-Botero, J.R. Grace, S.S.E.H. Elnashaie, C.J. Lim, Advances in Modeling of Fluidized-Bed Catalytic Reactors: a Comprehensive Review, *Chemical Engineering Communications*, 196 (2009) 1375–1405.
- [78] R. Higbie, The Rate of Absorption of a Pure Gas into a Still Liquid During Short Periods of Exposure, *Transactions of the American Institute of Chemical Engineers*, 31 (1935) 365–387.
- [79] B. Du, L. Fan, F. Wei, W. Warsito, Gas and Solids Mixing in a Turbulent Fluidized Bed, *AIChE Journal*, 48 (2002) 1896–1909.
- [80] R.F. Mudde, Time-resolved X-ray tomography of a fluidized bed, *Powder Technology*, 199 (2010) 55–59.
- [81] M. Wormsbecker, T. Pugsley, J.R. van Ommen, J. Nijenhuis, R. Mudde, Effect of Distributor Design on the Bottom Zone Hydrodynamics in a Fluidized Bed Dryer Using 1-D X-ray Densitometry Imaging, *Industrial & Engineering Chemistry Research*, 48 (2009) 7004–7015.
- [82] Y. Jin, Z.Q. Yu, Z. Wang, P. Cai, In: K. Østergaard, A. Sorensen (Eds.), *Fluidization V*, New York, Engineering Foundation, (1986) pp. 289–296.
- [83] P. Cai, S.P. Chen, Y. Jin, Z.Q. Yu, Z.W. Wang, Effect of operating temperature and pressure on the transition from bubbling to turbulent fluidization, *AIChE Symposium Series*, 85 (1989) 37–43.
- [84] M. Nakajima, M. Harada, M. Asai, R. Yamazaki, G. Jimbo, Bubble fraction and voidage in an emulsion phase in the transition to a turbulent fluidized bed, In: P. Basu, M. Horio, M. Hasatani (Eds.), *Circulating Fluidized Bed Technology III*, Oxford, Pergamon, (1991) pp. 79–84.

- [85] G.S. Lee, S.D. Kim, Bed Expansion Characteristics and Transition Velocity in Turbulent Fluidized Beds, *Powder Technology*, 62 (1990) 207–215.
- [86] S. Karimipour, T. Pugsley, A critical evaluation of literature correlations for predicting bubble size and velocity in gas–solid fluidized beds, *Powder Technology*, 205 (2011) 1–14.
- [87] J.-H. Choi, J.E. Son, S.D. Kim, Bubble size and frequency in gas fluidized beds, *Journal of Chemical Engineering of Japan*, 21 (1988) 171–178.
- [88] K. Dubrawski, S. Tebianian, H.T. Bi, J. Chaouki, N. Ellis, R. Gerspacher, et al., Traveling column for comparison of invasive and non-invasive fluidization voidage measurement techniques, *Powder Technology*, 235 (2013) 203–220.
- [89] D. Kunii, O. Levenspiel, The KL reactor model for circulating fluidized beds, *Chemical Engineering Science*, 55 (2000) 4563–4570.
- [90] A. Bischi, Ø. Langørgen, J.-X. Morin, J. Bakken, M. Ghorbaniyan, M. Bysveen, O. Bolland, Performance analysis of the cold flow model of a second generation chemical looping combustion reactor system, *Energy Procedia*, 4 (2011) 449–456.
- [91] W. de Vos, W. Nicol, E. du Toit, Entrainment behaviour of high-density Geldart A powders with different shapes, *Powder Technology*, 190 (2009) 297–303.
- [92] W. Liu, N.N. Clark, Relationships Between Distributions Lengths and Distributions of Chord of Bubble Sizes Including Their Statistical Parameters, *International Journal of Multiphase Flow*, 21 (1995) 1073–1089.

Appendix A : XRT Calibration

Calibration was done for two X-ray source intensities, at X-ray source settings of 25 mA and 50 mA. This dual calibration was required due to the large variation in solids concentrations as the superficial velocity is increased.

At the low-velocity bubbling regime, X-rays of higher intensity (50 mA) were required to penetrate the bed. If a lower intensity is used, all the X-rays are attenuated by the bed to undetectable levels. As the superficial velocity is increased, the solids concentration goes down and the detectors become overexposed. From a superficial velocity of 0.2 m/s, X-rays of a lower intensity (25 mA) had to be used.

Calibration points are obtained by placing a thin acrylic partition in the column at different positions and filling one side with material. The following figures show the calibration points and curves, and the tables report the values of A_{cal} , B_{cal} and C_{cal} .

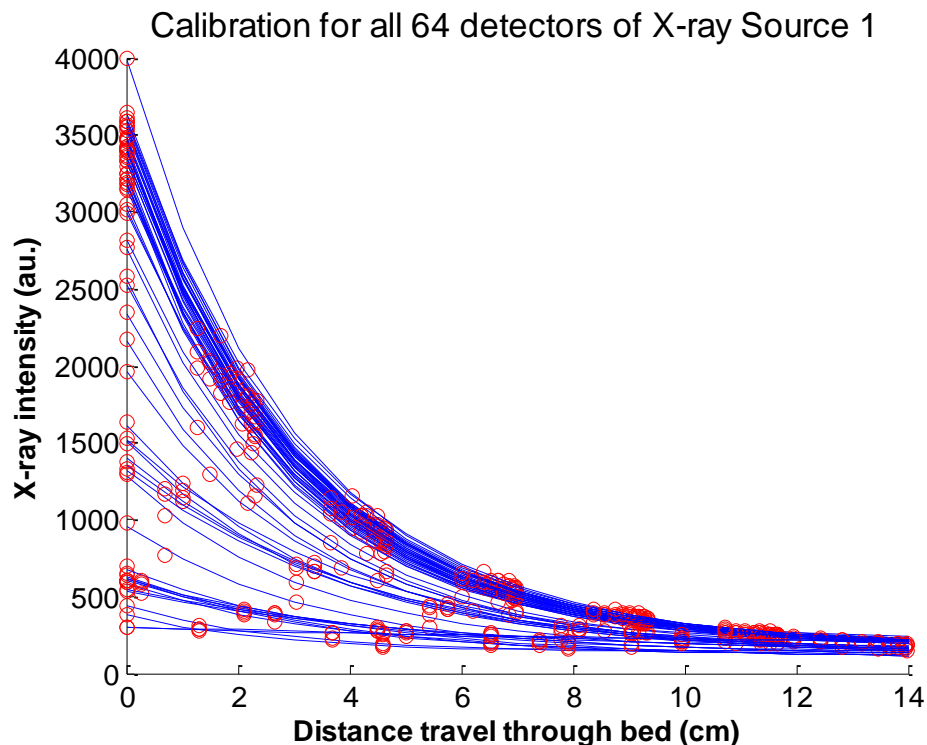


Figure A.1: Calibration curves at 25 mA, source 1

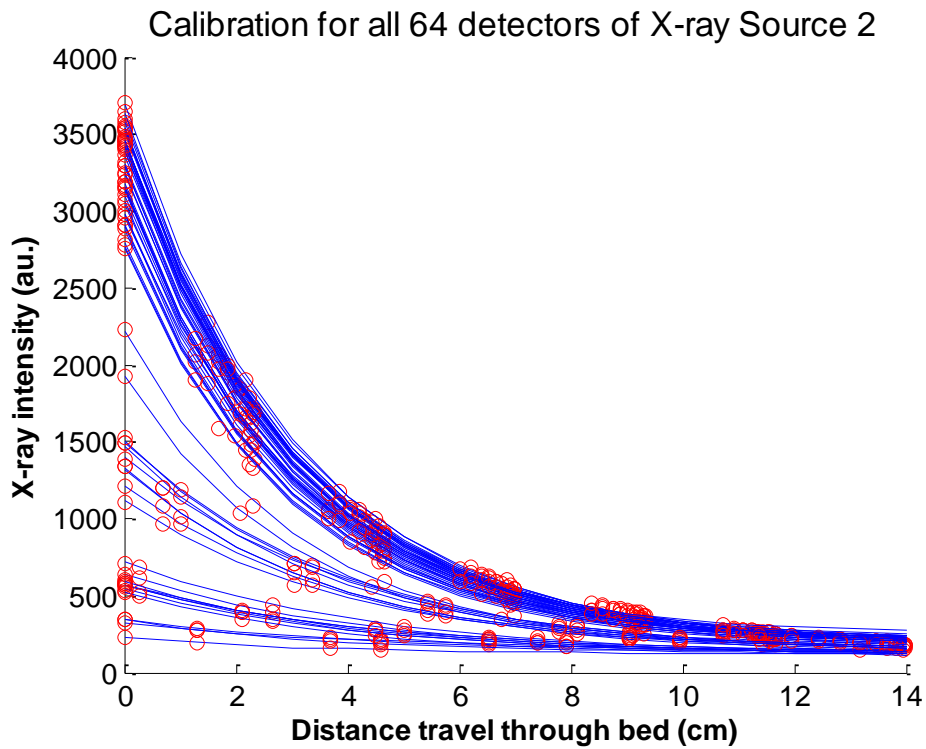


Figure A.2: Calibration curves at 25 mA, source 2

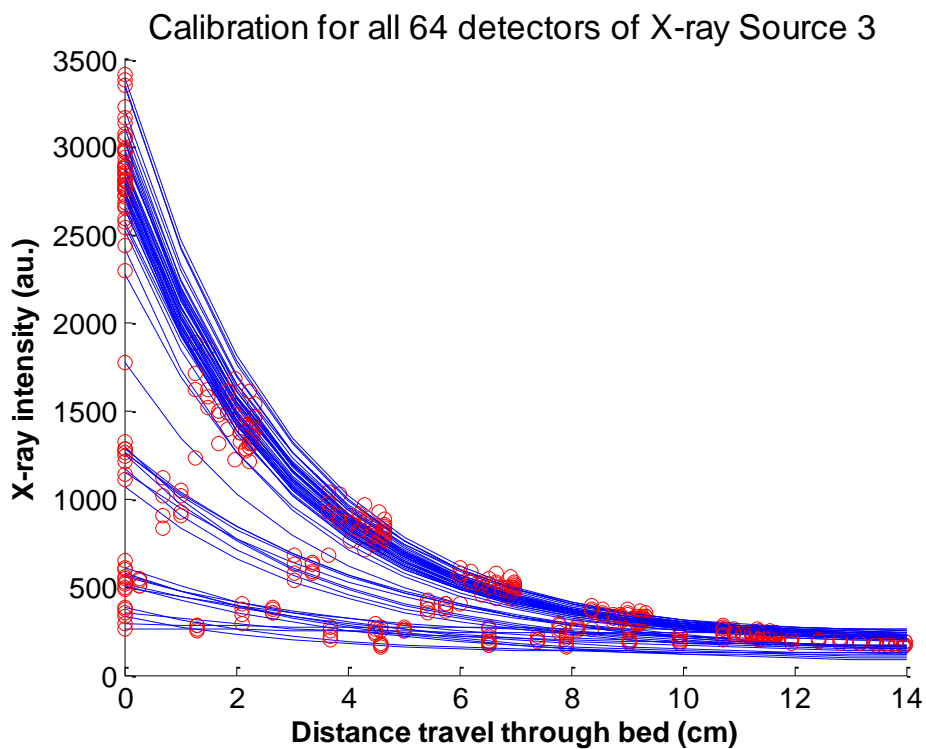


Figure A.3: Calibration curves at 25 mA, source 3

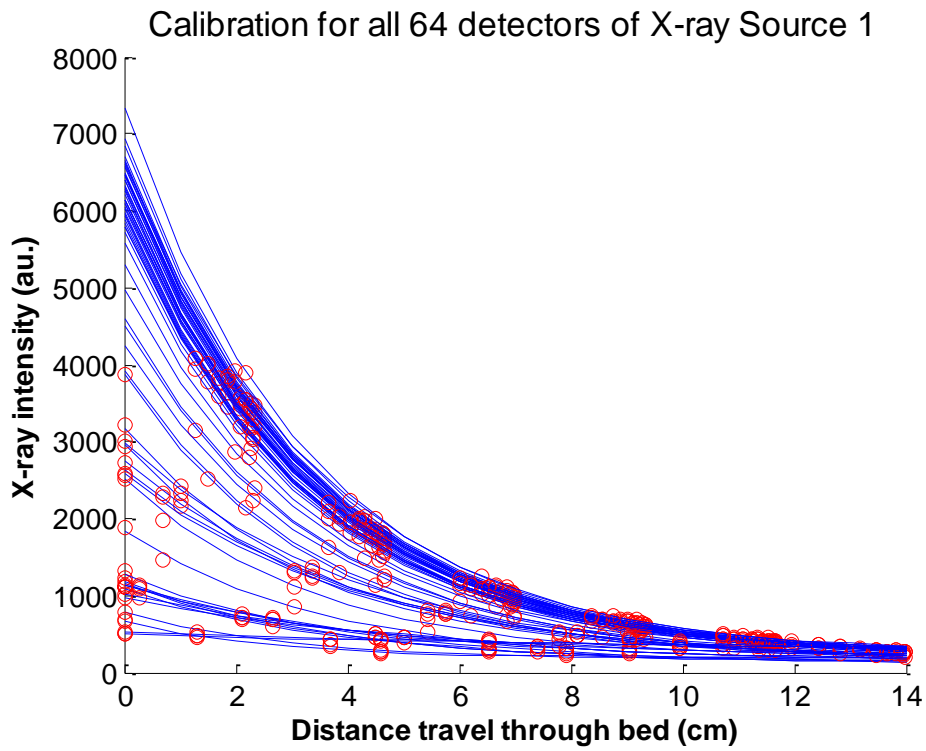


Figure A.4: Calibration curves at 50 mA, source 1

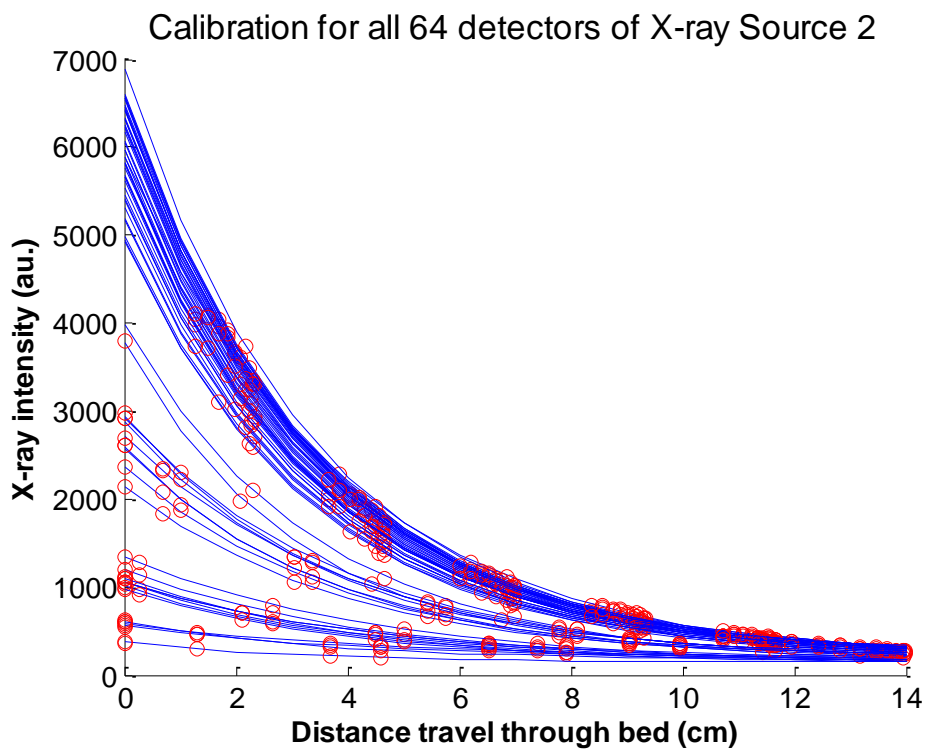


Figure A.5: Calibration curves at 50 mA, source 2

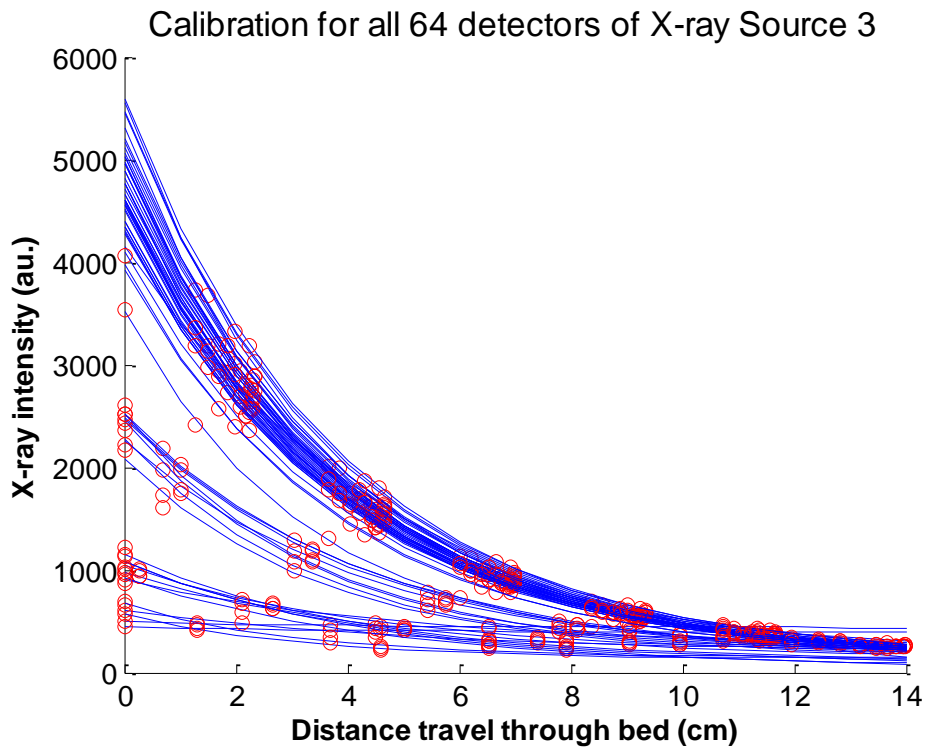


Figure A.6: Calibration curves at 50 mA, source 3

Table A-1: Calibration coefficients for source 1 and 25 mA

Detector	X-ray source 1 (with a setting of 25 mA)					
	Top row sensors			Bottom row sensors		
	A _{cal}	B _{cal}	C _{cal}	A _{cal}	B _{cal}	C _{cal}
1	139.6	241.8	2.5	137.3	296.6	2.7
2	105.6	506.8	3.7	101.8	525.5	3.8
3	109.4	468.4	3.8	105.7	563.3	3.9
4	134.4	1143.9	3.3	122.1	830.7	3.4
5	149.3	1359.3	3.4	127.2	1477.3	3.4
6	201.0	2354.3	2.7	215.6	2966.6	2.7
7	213.8	3055.9	2.8	221.7	3212.2	2.8
8	201.3	3024.1	2.8	203.4	3190.9	2.9
9	200.6	3033.6	2.9	195.1	3214.2	2.9
10	198.0	3339.1	2.9	167.5	2590.2	2.9
11	197.8	3267.5	2.9	180.9	3203.7	3.0
12	200.3	3787.4	2.9	158.4	2000.8	3.0
13	171.3	3146.8	3.0	180.7	3373.5	3.0
14	177.3	2864.8	3.0	173.8	3145.4	3.0
15	169.9	3036.9	3.0	174.5	3003.1	3.0
16	180.6	3366.6	3.0	146.1	2369.5	3.0
17	180.3	3457.1	3.0	172.4	3176.3	3.1
18	177.1	3223.1	3.1	150.7	2184.4	3.1
19	183.9	3390.8	3.1	184.0	3332.7	3.1
20	168.7	2642.4	3.1	164.2	3224.7	3.1
21	176.9	3284.4	3.1	175.0	3300.3	3.1
22	168.8	2844.3	3.1	177.6	3213.7	3.1
23	180.2	3399.6	3.2	177.7	3276.4	3.2
24	178.2	3202.4	3.2	171.5	3167.7	3.2
25	168.2	3009.9	3.2	167.6	3433.4	3.2
26	161.8	2981.3	3.2	136.1	1823.6	3.3
27	163.0	2828.2	3.3	172.8	2993.0	3.3
28	109.4	1404.0	4.1	98.4	1297.9	4.1
29	118.4	1231.7	4.2	108.9	1205.4	4.2
30	117.9	492.7	4.6	112.5	486.3	4.5
31	141.3	407.2	5.0	132.2	397.5	5.2
32	180.7	112.3	10.6	110.7	189.7	18.8

Table A-2: Calibration coefficients for source 2 and 25 mA

X-ray source 2 (with a setting of 25 mA)						
Detector	Top row sensors			Bottom row sensors		
	A _{cal}	B _{cal}	C _{cal}	A _{cal}	B _{cal}	C _{cal}
1	141.0	199.1	4.3	134.6	186.4	4.5
2	122.4	449.6	4.4	107.6	459.9	4.5
3	105.1	533.5	4.4	110.3	603.5	4.4
4	128.6	1266.7	4.0	125.4	986.6	3.9
5	116.4	1375.3	4.0	111.0	1103.9	3.9
6	185.1	2849.5	3.1	183.9	2769.5	3.2
7	195.3	3154.7	3.1	190.5	3401.5	3.1
8	197.5	3187.3	3.1	191.5	3248.3	3.1
9	203.0	3312.2	3.1	171.0	3245.7	3.1
10	196.3	3245.6	3.1	191.0	3212.6	3.1
11	190.8	3310.8	3.1	140.1	1778.7	3.1
12	174.5	3056.6	3.1	192.2	3502.8	3.1
13	195.7	3371.9	3.0	184.1	3121.3	3.0
14	184.4	3101.8	3.0	160.9	2810.9	3.0
15	188.4	3344.0	3.0	150.3	2068.8	3.0
16	181.3	2974.1	3.0	188.3	2906.4	3.0
17	195.9	3346.8	3.0	168.2	2732.7	3.0
18	190.8	3335.7	3.0	175.2	2591.7	3.0
19	185.5	2877.7	2.9	180.5	3061.3	3.0
20	192.8	2940.5	2.9	162.7	2588.2	3.0
21	209.3	3234.5	2.9	182.1	2687.8	3.0
22	199.2	3087.6	2.9	191.6	2949.0	2.9
23	185.9	2709.8	2.9	200.1	3215.8	2.9
24	205.3	2967.5	2.9	213.6	3418.4	2.9
25	216.7	3237.4	2.9	198.2	2596.2	2.9
26	223.8	3235.3	2.9	208.5	2949.0	2.8
27	249.3	3141.3	2.9	215.3	2761.3	2.8
28	142.1	1364.8	3.6	139.8	1188.0	3.5
29	137.1	1177.3	3.6	142.7	1327.9	3.5
30	113.6	432.0	4.0	111.3	459.3	4.0
31	103.8	421.5	3.9	124.3	469.7	3.9
32	133.3	215.4	3.2	121.9	108.6	3.1

Table A-3: Calibration coefficients for source 3 and 25 mA

X-ray source 3 (with a setting of 25 mA)						
Detector	Top row sensors			Bottom row sensors		
	A _{cal}	B _{cal}	C _{cal}	A _{cal}	B _{cal}	C _{cal}
1	235.5	29.6	5.5	255.9	33.3	6.1
2	173.1	324.1	5.2	158.7	196.7	4.9
3	113.3	407.0	4.8	131.4	430.9	4.8
4	105.5	1048.5	4.4	106.9	1155.6	4.4
5	115.8	1146.0	4.2	111.6	1175.7	4.2
6	190.8	2573.8	3.2	141.3	1634.5	3.3
7	181.5	2395.3	3.2	177.1	2751.3	3.2
8	171.8	2384.1	3.1	167.4	2571.9	3.1
9	175.4	2490.0	3.1	178.7	2609.9	3.1
10	189.5	2686.9	3.0	168.9	2110.3	3.0
11	185.0	2521.4	3.0	168.3	2723.5	3.1
12	202.3	2667.1	2.9	183.0	2659.9	3.0
13	180.5	2343.0	2.9	175.0	2465.7	3.0
14	193.8	2674.5	2.9	174.6	2779.1	3.0
15	187.9	2644.8	2.9	169.3	2888.3	3.0
16	202.5	3134.4	2.9	179.5	2800.4	3.0
17	192.6	3015.6	2.9	197.5	2950.8	3.0
18	190.9	2771.2	2.9	182.4	2776.4	2.9
19	203.4	2834.2	2.9	184.0	2609.8	2.9
20	195.5	2611.6	2.8	206.1	3190.8	2.9
21	200.4	2496.1	2.8	179.4	2466.7	2.9
22	203.5	2540.7	2.8	190.9	2598.2	2.9
23	222.8	2799.6	2.7	224.5	3125.5	2.8
24	222.8	2513.9	2.7	208.5	2899.9	2.8
25	228.0	2551.7	2.7	195.6	2222.5	2.7
26	229.3	2490.6	2.6	213.9	2582.0	2.7
27	248.1	2483.8	2.6	240.8	2585.3	2.7
28	149.9	1141.7	3.3	132.3	1116.9	3.5
29	142.2	1024.8	3.4	126.9	943.0	3.5
30	101.8	511.8	4.2	84.3	488.2	4.4
31	63.6	511.3	4.5	74.2	430.6	4.6
32	120.4	260.0	3.1	116.5	213.5	3.2

Table A-4: Calibration coefficients for source 1 and 50 mA

X-ray source 1 (with a setting of 50 mA)						
Detector	Top row sensors			Bottom row sensors		
	A _{cal}	B _{cal}	C _{cal}	A _{cal}	B _{cal}	C _{cal}
1	181.1	491.7	2.5	183.8	601.3	2.7
2	117.1	1030.7	3.7	108.0	1068.6	3.8
3	123.8	953.4	3.8	117.8	1145.4	3.9
4	182.2	2320.8	3.3	152.3	1686.7	3.4
5	198.9	2755.5	3.4	175.3	2996.9	3.5
6	176.2	4336.5	3.4	198.3	5511.6	3.3
7	200.5	5634.4	3.3	207.1	5941.2	3.3
8	215.8	5677.6	3.2	191.4	5893.0	3.4
9	220.3	5713.5	3.2	191.6	5960.1	3.4
10	214.6	6246.2	3.3	167.5	4810.6	3.4
11	215.3	6116.0	3.3	190.4	6009.5	3.4
12	224.9	7097.8	3.3	168.3	3758.3	3.3
13	192.5	5908.5	3.3	192.8	6293.5	3.4
14	197.1	5390.0	3.3	179.6	5833.9	3.4
15	195.3	5752.3	3.3	184.7	5608.7	3.4
16	211.9	6431.0	3.3	155.2	4436.3	3.4
17	213.2	6625.3	3.3	184.5	5966.9	3.4
18	210.4	6197.7	3.3	156.9	4087.4	3.4
19	212.2	6479.6	3.3	195.6	6272.7	3.4
20	193.7	5093.3	3.3	180.8	6121.5	3.4
21	219.8	6433.8	3.3	193.0	6281.2	3.4
22	207.4	5585.1	3.3	202.6	6189.8	3.4
23	230.0	6700.6	3.3	207.0	6364.3	3.4
24	230.9	6348.7	3.3	210.8	6229.0	3.4
25	229.1	6037.4	3.3	187.1	6417.6	3.6
26	235.9	6047.0	3.2	179.2	3698.4	3.3
27	258.2	5724.3	3.2	255.3	5794.8	3.4
28	126.4	2847.6	4.1	114.7	2633.2	4.2
29	134.6	2500.1	4.2	131.5	2446.1	4.2
30	140.0	1001.2	4.6	139.4	989.7	4.5
31	184.7	830.5	5.0	170.2	808.7	5.2
32	293.5	206.2	9.2	183.1	332.4	15.5

Table A-5: Calibration coefficients for source 2 and 50 mA

X-ray source 2 (with a setting of 50 mA)						
Detector	Top row sensors			Bottom row sensors		
	A _{cal}	B _{cal}	C _{cal}	A _{cal}	B _{cal}	C _{cal}
1	189.5	402.6	4.3	177.7	375.7	4.4
2	149.7	909.7	4.4	128.5	929.8	4.5
3	119.0	1080.0	4.4	128.1	1221.3	4.4
4	151.1	2557.7	4.0	149.7	1993.1	3.9
5	140.9	2776.7	4.0	135.4	2228.3	3.9
6	244.0	5639.8	3.3	261.0	5550.1	3.2
7	224.8	6020.6	3.4	123.9	5754.0	3.9
8	238.8	6204.0	3.3	241.1	6348.3	3.3
9	234.0	6367.0	3.4	215.9	6324.5	3.3
10	222.9	6184.4	3.4	230.2	6218.0	3.3
11	213.7	6264.2	3.4	188.9	3589.2	3.1
12	197.9	5772.1	3.4	226.4	6670.9	3.3
13	222.5	6347.5	3.4	208.1	5869.6	3.4
14	211.2	5830.0	3.4	177.0	5215.3	3.4
15	211.0	6214.0	3.4	161.5	3812.3	3.4
16	197.2	5458.5	3.4	201.1	5329.0	3.4
17	213.4	6129.2	3.4	180.9	5007.0	3.4
18	208.3	6111.7	3.4	186.5	4736.3	3.4
19	201.3	5263.0	3.4	195.5	5635.8	3.4
20	210.2	5403.5	3.4	176.1	4759.3	3.4
21	231.8	5972.4	3.3	198.0	4967.1	3.4
22	224.3	5745.1	3.3	209.1	5447.9	3.3
23	211.8	5098.9	3.3	223.0	5957.0	3.3
24	233.6	5586.6	3.3	232.2	6322.1	3.3
25	240.4	6068.5	3.3	203.5	4784.7	3.4
26	230.4	6002.6	3.4	212.3	5468.9	3.4
27	201.9	5563.1	3.6	226.6	5185.4	3.3
28	189.2	2754.9	3.6	186.3	2398.2	3.6
29	182.0	2377.2	3.6	201.5	2680.0	3.5
30	129.5	875.4	4.0	129.6	929.2	4.0
31	125.5	853.5	3.9	149.7	950.6	3.9
32	178.1	434.8	3.2	142.4	226.5	3.2

Table A-6: Calibration coefficients for source 3 and 50 mA

X-ray source 3 (with a setting of 50 mA)						
Top row sensors			Bottom row sensors			
Detector	A_{cal}	B_{cal}	C_{cal}	A_{cal}	B_{cal}	C_{cal}
1	393.2	55.3	4.1	435.4	59.0	4.2
2	243.8	659.7	5.1	207.9	402.7	4.9
3	136.4	829.4	4.8	161.1	876.4	4.7
4	117.7	2130.8	4.4	125.5	2348.3	4.4
5	135.2	2330.4	4.2	134.0	2389.1	4.2
6	222.9	5078.4	3.5	197.8	3321.2	3.3
7	175.7	4593.7	3.6	192.6	5357.1	3.5
8	149.2	4461.9	3.6	154.9	4867.6	3.6
9	149.6	4610.9	3.7	150.9	4811.9	3.7
10	154.8	4875.8	3.7	142.1	3830.4	3.7
11	135.7	4440.1	3.8	151.4	4296.2	5.2
12	116.9	4485.3	4.0	151.1	4738.6	3.7
13	119.7	3976.3	3.9	141.0	4356.3	3.7
14	130.2	4532.4	3.9	125.5	4849.4	3.8
15	128.9	4470.9	3.9	115.7	5005.3	3.8
16	139.7	5311.7	3.8	130.4	4833.2	3.8
17	129.2	5078.7	3.8	135.8	5027.0	3.9
18	130.8	4640.3	3.8	118.9	4688.8	3.9
19	141.0	4744.4	3.8	129.1	4428.4	3.8
20	137.7	4371.4	3.8	137.6	5442.8	3.8
21	137.8	4158.3	3.8	121.0	4187.0	3.8
22	125.3	4209.8	3.9	126.8	4430.7	3.8
23	120.1	4596.1	3.9	137.0	5323.2	3.9
24	119.8	4155.8	4.0	117.1	4952.3	3.9
25	115.6	4271.7	3.9	114.7	3800.6	3.9
26	113.8	4224.7	3.9	111.0	4470.5	3.8
27	115.5	4276.4	3.9	120.4	4539.4	3.8
28	203.2	2322.0	3.3	179.1	2267.8	3.5
29	184.3	2083.6	3.4	160.7	1914.7	3.5
30	101.0	1042.3	4.2	80.3	992.8	4.4
31	37.6	1039.5	4.5	50.2	875.1	4.6
32	143.4	527.7	3.1	132.2	436.0	3.2

Appendix B : Determination of Hydrodynamic Parameters

Minimum fluidization was determined by measuring the pressure drop across the bed. The bed was fluidized and the superficial velocity decreased until the pressure drop decreased. At this point the bed starts defluidizing; this is where U_{mf} is.

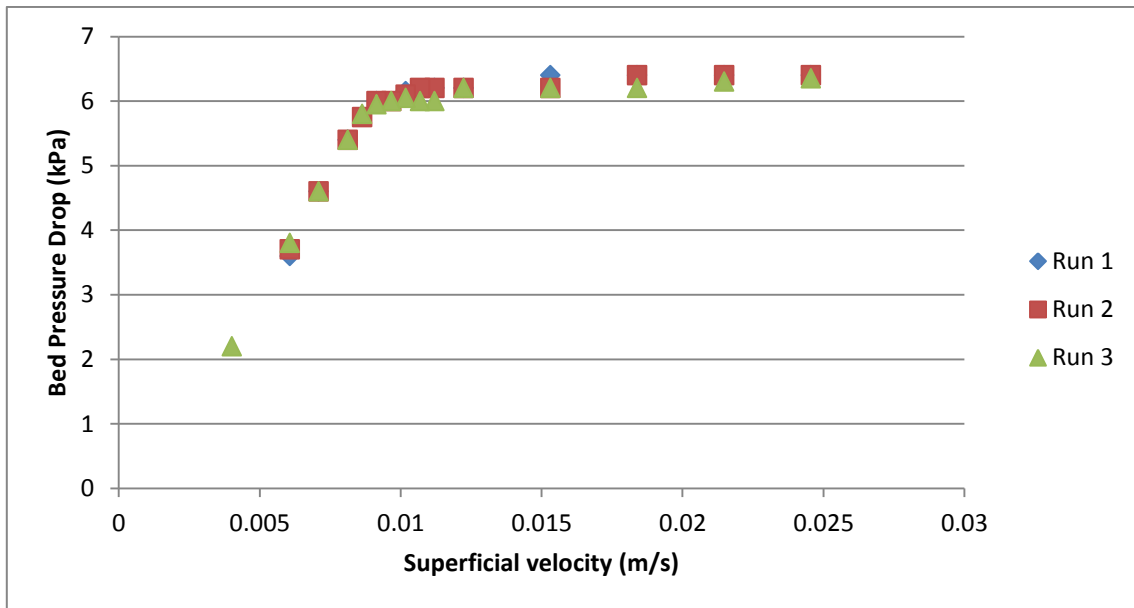


Figure B.1: U_{mf} for Sand baseline determined to be 9.1 mm/s

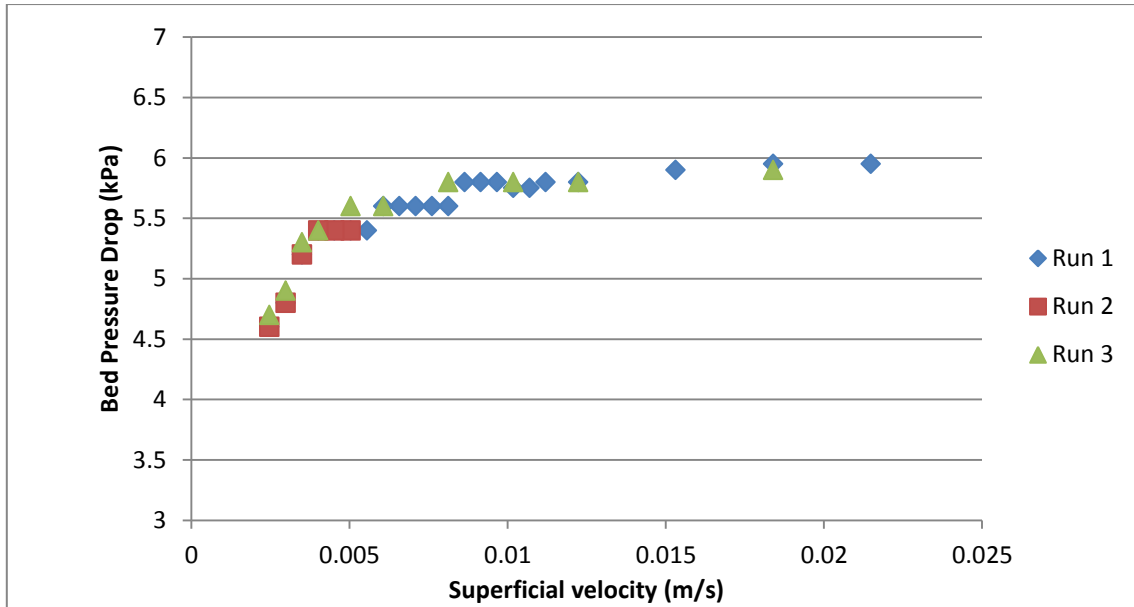


Figure B.2: U_{mf} for Sand with fines determined to be 4.0 mm/s

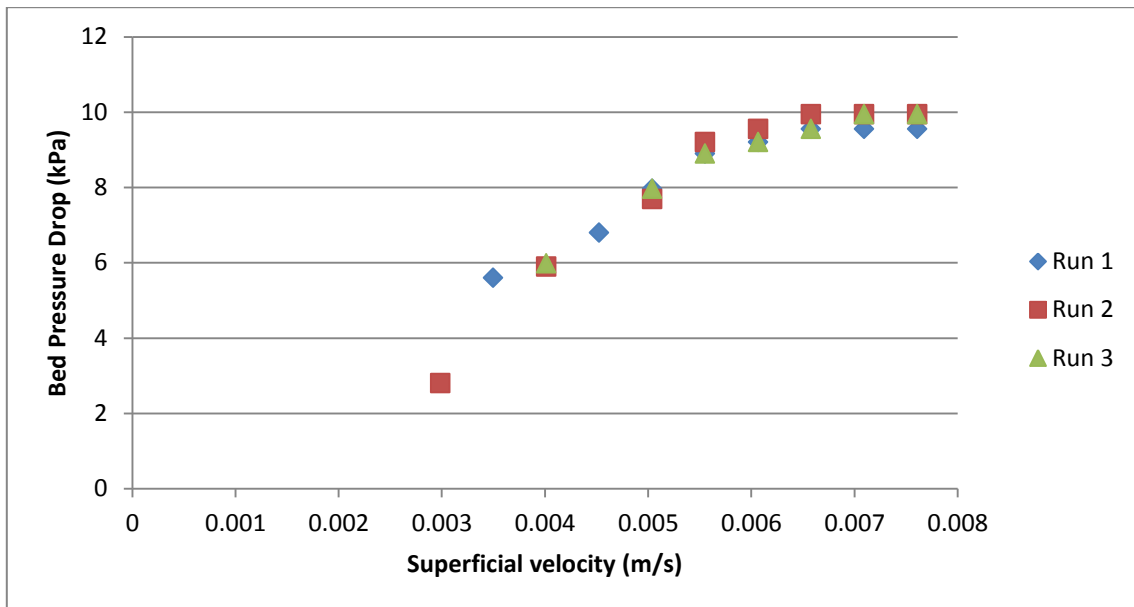


Figure B.3: U_{mf} for FeSi baseline determined to be 6.5 mm/s

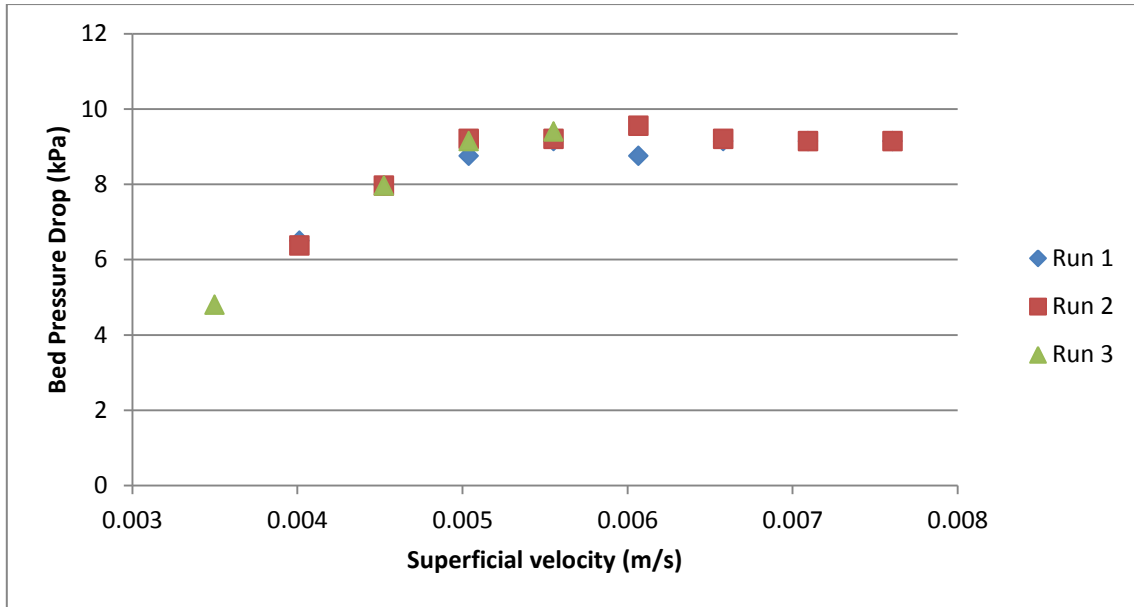


Figure B.4: U_{mf} for FeSi with fines determined to be 5.0 mm/s

Entrainment (G_s) was determined by closing a valve in the solids return pipe below the cyclones for 1 min. The height of the collected solids was measured and converted to a mass using the pipe diameter and bulk density. Entrainment rate measurements are reported in [Figure B.5](#) and [Figure B.6](#). Each data point is based on three repeat runs. For the case where fines were added to the baseline sand mixture, the entrainment could not be measured. The fines mixture had a significant static charge after the cyclone separation process and the height of the collected solids could not be seen and measured.

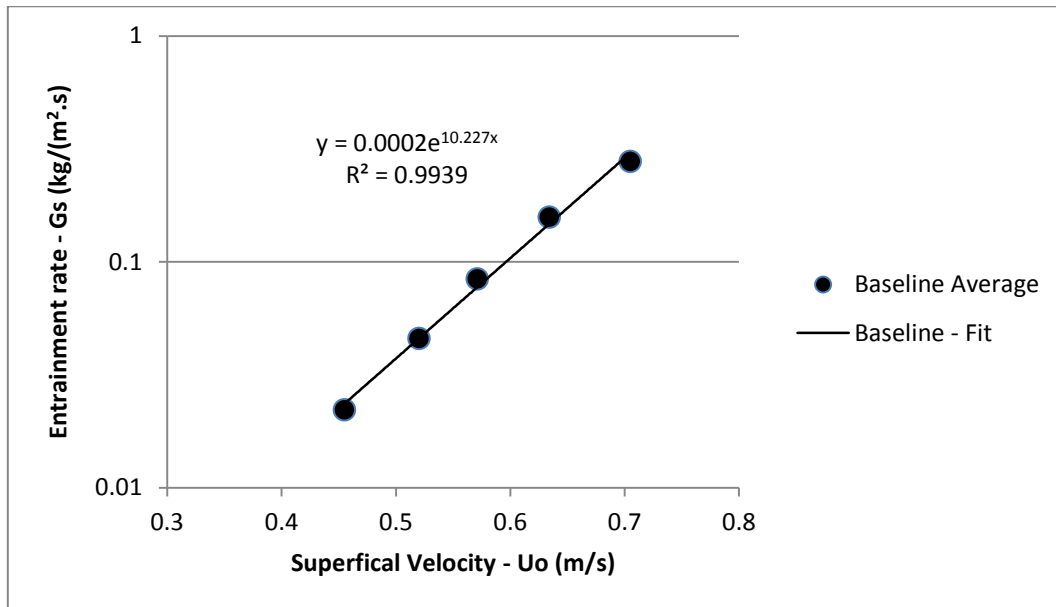


Figure B.5: Entrainment measurements for Sand baseline

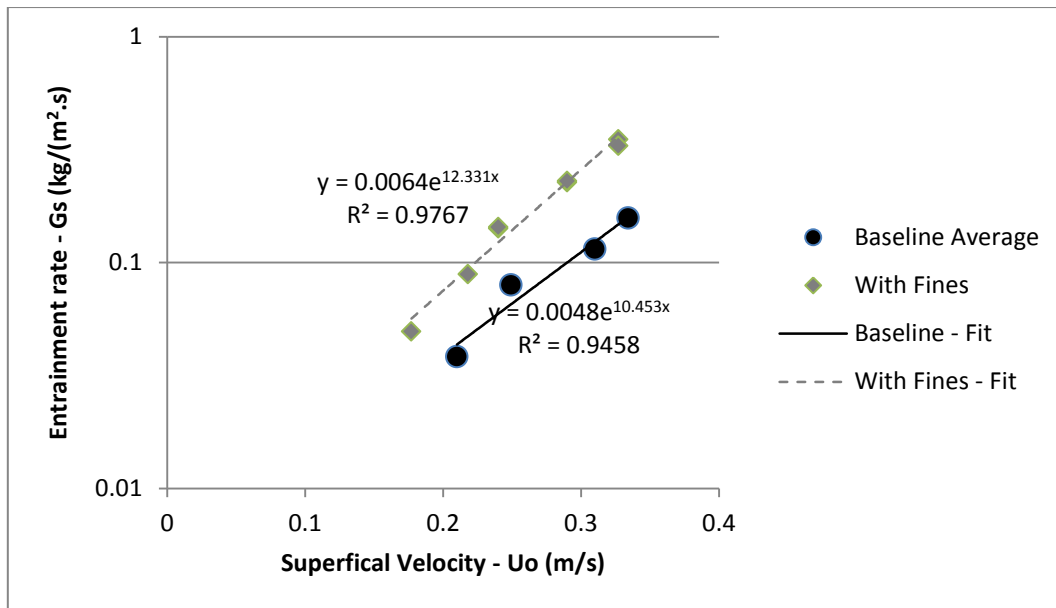


Figure B.6: Entrainment measurements for FeSi baseline and with fines

Appendix C : Reactor Performance Data

Table C-1: Data of baseline sand experiments

Superficial velocity (U_0) - m/s	First-order rate constant (k_R) - s^{-1}	Conversion (x)
0.065	15.628	0.961
0.065	10.360	0.945
0.067	7.442	0.966
0.125	10.360	0.864
0.128	16.367	0.888
0.128	21.900	0.938
0.192	14.164	0.811
0.192	16.232	0.883
0.195	9.549	0.782
0.258	14.164	0.772
0.258	16.232	0.825
0.260	6.636	0.787
0.319	12.366	0.797
0.319	6.636	0.748
0.322	14.135	0.738
0.383	11.797	0.720
0.386	14.135	0.710
0.386	6.469	0.668
0.446	7.442	0.579
0.449	11.797	0.698
0.452	12.366	0.675
0.512	4.969	0.505
0.521	5.265	0.580
0.521	6.469	0.521
0.579	5.591	0.467
0.588	4.969	0.434
0.588	5.265	0.472
0.646	4.722	0.385
0.646	5.591	0.410
0.646	4.107	0.354
0.697	4.722	0.376
0.697	4.107	0.344
0.697	5.431	0.349

Table C-2: Data of sand with added fines experiments

Superficial velocity (U_0) - m/s	First-order rate constant (k_R) - s^{-1}	Conversion (x)
0.064	2.349	0.954
0.064	3.014	0.957
0.067	6.315	0.959
0.117	4.810	0.905
0.129	2.977	0.911
0.129	6.315	0.879
0.193	4.102	0.817
0.193	3.014	0.840
0.193	4.340	0.879
0.255	4.102	0.779
0.258	4.810	0.810
0.261	2.977	0.736
0.320	4.521	0.799
0.323	4.340	0.787
0.326	2.800	0.666
0.388	2.800	0.667
0.388	2.945	0.642
0.391	3.755	0.689
0.450	3.755	0.650
0.453	2.004	0.393
0.455	4.521	0.665
0.521	1.612	0.271
0.521	0.968	0.273
0.521	1.230	0.243
0.579	1.230	0.251
0.588	1.612	0.248
0.588	1.373	0.221
0.646	1.230	0.230
0.646	2.004	0.304
0.697	1.440	0.256

Table C-3: Data of baseline FeSi experiments

Superficial velocity (U_0) - m/s	First-order rate constant (k_R) - s^{-1}	Conversion (x)
0.070	2.054	0.945
0.070	2.249	0.914
0.073	1.490	0.932
0.091	1.628	0.940
0.093	1.055	0.780
0.093	2.609	0.911
0.102	2.768	0.931
0.125	2.164	0.792
0.134	2.736	0.945
0.137	1.055	0.783
0.151	2.593	0.845
0.163	2.538	0.889
0.195	2.852	0.835
0.203	1.484	0.743
0.209	2.386	0.844
0.209	3.129	0.741
0.212	1.490	0.751
0.229	1.484	0.719
0.232	2.557	0.777
0.235	3.314	0.794
0.235	3.422	0.850
0.241	2.191	0.603
0.253	2.851	0.802
0.258	3.129	0.751
0.270	2.557	0.715
0.279	1.905	0.731
0.290	2.191	0.679
0.299	1.905	0.720
0.302	3.122	0.795
0.316	3.581	0.797
0.345	3.243	0.615
0.362	3.579	0.795
0.374	3.243	0.640

Table C-4: Data of FeSi with added fines experiments

Superficial velocity (U_0) - m/s	First-order rate constant (k_R) - s^{-1}	Conversion (x)
0.079	1.216	0.873
0.082	1.602	0.771
0.096	0.683	0.617
0.108	1.351	0.710
0.131	2.899	0.834
0.148	1.633	0.639
0.151	2.585	0.720
0.169	0.948	0.583
0.169	1.781	0.635
0.186	1.819	0.640
0.186	2.146	0.667
0.218	2.021	0.607
0.235	2.162	0.633
0.244	2.138	0.740
0.258	2.256	0.668
0.279	2.422	0.706
0.287	4.253	0.708
0.302	3.123	0.729
0.307	2.905	0.732
0.328	2.119	0.651
0.348	2.458	0.675
0.365	3.592	0.673
0.383	3.789	0.664